

AN ABSTRACT OF THE DISSERTATION OF

Zhifei Li for the degree of Doctor of Philosophy in Chemistry presented on June 13, 2018.

Title: Fundamental Studies of the Structure-Property Correlations of Na-ion and K-ion Storage in Non-Graphitic Carbon

Abstract approved:

Xiulei (David) Ji

Grid-scale energy storage systems are urgently needed to increase the flexibility and rigidity of the grid for modern society and take full advantage of the renewable green energy resources such as solar energy and wind energy. Na-ion batteries (NIBs) and K-ion batteries (KIBs) have been emerged as one of the most promising solutions for grid-scale energy storage systems. Unfortunately, graphite, which is the commercialized anode in LIBs, does not show meaningful capacity in NIBs, and it shows poor cycling performance in KIBs. Non-graphitic carbon materials have been shown promising electrochemical performance in NIBs and KIBs. However, due to the structural complexity of non-graphitic carbon, the structure-property correlations of non-graphitic carbon anodes for Na-ion and K-ion storage are still not well established. Therefore, in this thesis, I focus on understanding the structure-property correlations of Na-ion and K-ion storage in non-graphitic carbon and improving the Na-ion and K-ion storage performance of non-graphitic carbon anodes.

There had been reports regarding the structure-property correlations of hard carbon anodes in NIBs, where discrepancies still exist. In addition, the capacity of hard carbon anodes in NIBs rarely reaches values beyond 300 mAh/g. Herein, in this thesis, we first applied PO_x doping on hard carbon to tune its structure, which increases its reversible capacity from 283 to 359 mAh/g. We observe the interlayer d-spacing of the turbostratic nanodomains is expanded and the defect concentration of the doped hard carbon is increased. The structural changes of hard carbon lead to enhanced plateau and slope capacity. Our study demonstrates that Na-ion storage in hard carbon heavily depends on carbon local structures, where such structures, despite being disordered, can be tuned toward unusually high capacities.

Even though our above-mentioned results agree well with our early proposed model, the structure-property correlations of Na-ion storage in hard carbon is still not solidified. Furthermore, how defects affect the slope capacity and what types of defects are beneficial for the slope capacity is still not clear. Therefore, in our following work, we synthesized a series of well-controlled heteroatom doped hard carbons, namely, P-, S- and B-doped hard carbon, and non-doped hard carbon where they show consistently low surface area. We then comprehensively characterized these hard carbons' structural features and electrochemical performance which allows us to reveal the mechanism of Na-ion storage in hard carbon. Our combined experimental studies and first principles calculations reveal that it is the Na-ion-defect binding that corresponds to the slope capacity, while the Na intercalation between graphenic layers is responsible for the low-

potential plateau capacity. In addition, our computational results also revealed that too strong binding between Na-ion and defects will lead to irreversibility. The new understanding provides a new set of design principles to optimize hard carbon anode for Na-ion storage.

In a recent work, guided by our proposed design principles, we synthesized a highly defective hard carbon by microwave heating a low-temperature (650°C) pre-annealed hard carbon. After a brief microwave treatment, *i.e.*, for 6 seconds, the reversible capacity of the hard carbon was increased from 204 to 308 mAh/g. The microwaved carbon retains a high extent of structural defects after microwaving the low-temperature annealed hard carbon. Such a defective structure exhibits a much higher slope capacity than conventional hard carbon with less low-potential plateau capacity which can reduce the safety concerns. The microwave heating of carbon represents a new direction for tuning structures of hard carbon.

The rate capability of hard carbon has long been underestimated in prior studies that used carbon/Na two-electrode half-cells. Through a three-electrode cell setup, we discover that it is the overpotential of the sodium counter electrode that drives the half-cells to the lower cutoff potential prematurely during hard carbon sodiation, particularly at high current rates, which prevents the hard carbon anode from being fully sodiated. Hard carbon demonstrates a much better rate-capability in this three-electrode setup.

In the last part of this thesis, we studied soft carbon as anode for K-ion storage. In this work, we synthesized a series of soft carbons (SCs) by the pyrolysis of 3,4,9,10-perylenetetracarboxylic dianhydride (PTCDA) at different temperatures. By using polyacrylic acid as the binder, SC obtained at 700°C (SC700) shows the highest capacity of 354 mAh/g which is the highest capacity of non-graphitic carbons reported so far by accounting the potential between 0-2 V. More importantly, SC700 shows a better cycling stability than SCs obtained at higher temperature, where it is still worse than the cycling performance of hard carbons. Via combined experimental and computational studies, we generate mechanistic insights about the structure-property correlations of K-ion storage in soft carbons.

©Copyright by Zhifei Li
June 13, 2018
All Rights Reserved

Fundamental Studies of the Structure-Property Correlations of Na-ion and K-ion
Storage in Non-Graphitic Carbon

by
Zhifei Li

A DISSERTATION

submitted to

Oregon State University

in partial fulfillment of
the requirements for the
degree of

Doctor of Philosophy

Presented June 13, 2018
Commencement June 2019

Doctor of Philosophy dissertation of Zhifei Li presented on June 13, 2018

APPROVED:

Major Professor, representing Chemistry

Chair of the Department of Chemistry

Dean of the Graduate School

I understand that my dissertation will become part of the permanent collection of Oregon State University libraries. My signature below authorizes release of my dissertation to any reader upon request.

Zhifei Li, Author

ACKNOWLEDGEMENTS

I would like to thank my advisor, Dr. Xiulei Ji, for being supportive and patient with me throughout my time at Oregon State University. He is always passionate about research and science which has infected me and helped me develop the mindset of being a scientist. He is a wise mentor, and his philosophy towards work and life has inspired me to pursue excellence.

I would like to thank Dr. Michael Lerner, who is an excellent scientist and has provided me thoughtful advice. I would like to thank Dr. Wei Kong, Dr. May Nyman and Dr. Zhenxing Feng for being on my committee and providing me guidance throughout my PhD studies.

I am thankful to our collaborators for all their help on my research: Dr. Jun Lu, Dr. Tianpin Wu, Dr and Dr. Lu Ma from Argonne National Laboratory; Dr. Michelle Dolgos and Dr. Wesley Surta from Department of Chemistry; Dr. Alex Greaney from University of California, Riverside; Dr. Joerg C. Neufeind from Oak Ridge National Laboratory. I am grateful to Dr. Chih-Hung Chang and Dr. Changqing Pan for their help on the Raman tests. I would like to acknowledge Xin Li from Dr. Rich Carter's group, who is a smart chemist, for the help on the organic synthesis. I would also like to thank Dr. Hanyang Zhang for the great collaboration and help. I would like to thank Dr. William F. Stickle for the help on XPS tests. I would like to thank Dr. Mas Subramanian and Maxwell Wallace for the assistance on the electronic conductivity tests.

I would like to thank Dr. Wei Luo and Dr. Vadivukarasi Raju who guided me to start my work in Ji group, Dr. Zelang Jian who has provided me lots of great suggestions and help, and Dr. Clement Bommier who laid a good foundation for my work. I would also like to thank Dr. Xingfeng Wang, Dr. Bao Wang, Dr. Raghu Subash Chandrabose, Dr. Zhenyu Xing, Dr. Ismael Rodriguez Perez, Daniel Leonard, Dr. Xianyong Wu, Heng Jiang, Jessica Hong, and Woochul Shin, Shengyang Dong, Zhixuan Wei, Chong Zhang, Yunkai Xu and Keun Kim. I would also like to thank the undergrads, Yicong Chen and Zhi Sen Chong, who had been worked with me.

I am deeply thankful to my parents and my family for always being supportive throughout my whole student career. Without their supports, I could not have got to this point.

Lastly, but most importantly, I would like to express my deepest gratitude to my beloved wife, Yiyuan, for always being supportive and encouraging in every way possible. Without your love and sacrifices, I would not be who I am now.

TABLE OF CONTENTS

Page

Chapter 1 Motivation	1
1.1 Grid-scale energy storage.....	1
1.2 Grid-scale energy storage technologies	3
1.3 Objectives of this thesis	5
1.4 Reference	5
Chapter 2 Na-ion Batteries and K-ion Batteries	7
2.1 Background	7
2.2 Na-ion batteries	8
2.2.1 Cathode Materials for NIBs	11
2.2.2 Anode materials for NIBs	16
2.3 K-ion batteries.....	18
2.3.1 Graphite as anode for KIBs	20
2.4 Reference	22
Chapter 3 Na-ion Storage in Non-Graphitic Carbons.....	28
3.1 Background	28
3.2 Non-graphitic carbon	28
3.3 Characterization of non-graphitic carbon by neutron total scattering diffraction	31
3.4 Mechanism of Na-ion storage in hard carbon	34
3.5 Mechanism of Na-ion storage in soft carbon	40
3.6 Heteroatom doping of non-graphitic carbon for Na-ion storage.....	41
3.6.1 Nitrogen doping	42
3.6.2 Phosphorus and sulfur doping.....	43
3.6.3 Boron doping and fluorine doping.....	46
3.7 References.....	48

TABLE OF CONTENTS (Continued)

	<u>Page</u>
Chapter 4 High Capacity of Hard Carbon Anode in Na-Ion Batteries Unlocked by PO _x	
Doping.....	52
4.1 Abstract.....	52
4.2 Introduction.....	52
4.3 Experimental Section.....	55
4.4 Results and Discussion.....	58
4.5 Conclusion.....	69
4.6 References.....	70
Chapter 5 Mechanism of Na-Ion Storage in Hard Carbon Anodes Revealed by Heteroatom Doping.....	76
5.1 Abstract.....	76
5.2 Introduction.....	77
5.3 Experimental Section.....	82
5.4 Results and Discussion.....	85
5.4.1. Structure Characterization of Synthesized Materials.....	85
5.4.2 Electrochemical Behaviors of All Carbons.....	94
5.4.3 Computational Studies of The Na Binding.....	98
5.5 Conclusion.....	109
5.6 References.....	110
Chapter 6 Defective Hard Carbon Anode for Na-ion Batteries.....	115
6.1 Abstract.....	115
6.2 Introduction.....	116
6.3 Experimental Section.....	118
6.4 Results and Discussion.....	121

TABLE OF CONTENTS (Continued)

	<u>Page</u>
6.5 Conclusions.....	135
6.6 References.....	136
Chapter 7 Hard Carbon Anode of Sodium-Ion Batteries: Undervalued Rate Capability	142
7.1 Abstract.....	142
7.2 Introduction.....	142
7.3 Experimental Section	145
7.5 Conclusions.....	153
7.6 References.....	154
Chapter 8 Low-temperature Pyrolyzed Soft Carbon Anodes for K-ion Storage	158
8.1 Abstract.....	158
8.2 Introduction.....	158
8.3 Experimental Section	161
8.4 Results and Discussion.....	163
8.5 Conclusions.....	173
8.6 References.....	174

LIST OF FIGURES

<u>Figure</u>	<u>Page</u>
1.1 The resource composition of energy consumption in the United States from 1776 to 2015. ¹	2
2.1 (a) The predicted demand for lithium-ion batteries from 2015 to 2030. (b) The price change of lithium carbonate.	8
2.2 Schematic of Na-ion battery.	10
2.3 The structural schematic of different types of layered transition metal oxides Na_xMO_2 , where the sheet is composed of edge-sharing MeO_6 octahedra. The phase transition processes upon sodium extraction are also shown. ¹⁵	11
2.4 Galvanostatic sodiation-desodiation curve of $\text{P}_2\text{-Na}_x\text{CoO}_2$. The bottom left inset is the schematic of the structure of $\text{P}_2\text{-Na}_x\text{CoO}_2$ and the top right inset is enlarged galvanostatic sodiation-desodiation curve. ¹⁷	13
2.5 Unit cell structure of $\text{Na}_3\text{V}_2(\text{PO}_4)_3$. ³³	15
2.6 (a) First-cycle galvanostatic potassiation/depotassiation potential profiles at C/10. (b) XRD patterns of electrodes corresponding to the marked SOCs in A. (c) Structure diagrams of different K-GICs, side view (top row) and top view (bottom row). ⁵⁸	20
3.1 Franklin’s schematic representation of the structure of (a) a non-graphitizing carbon, and (b) a graphitizing carbon. ⁴	29
3.2 (a) Neutron total scattering associated PDF of various hard carbons. (b) Schematic local structure of graphene.....	32
3.3 (a) “House of Cards” model for sodium filled hard carbon. (b) Sodium potential profiles for glucose pyrolyzed to 1000°C. ⁹	35
3.4 Potentiogram and schematic of proposed Na-ion three-part storage mechanism. ¹⁵	37
3.5 Sodiation-desodiation profiles of pristine and phosphorus-doped hard carbons at current density of 20 mA/g. The inset is the TEM image of the phosphorus-doped hard carbon. ³²	43

LIST OF FIGURES (Continued)

<u>Figure</u>	<u>Page</u>
3.6 The charge-discharge profiles of disordered carbon before (a) and after sulfur-doping (b) at a current density of 0.02 A g^{-1} . ³¹	45
4.1 (a) N_2 sorption isotherms of doped carbons with and without the addition of GO. SEM images of (b) HC and (c) P-HC.	58
4.2 TEM EDX elemental mappings of P-HC and TEM images of HC and P-HC. (a,b) Elemental mappings for (a) carbon (b) phosphorus in P-HC. TEM images of (c) HC and (d) P-HC.	61
4.3 X-ray adsorption results of P-HC before cycling and P-HC at various state of charge. (a) XPS P-2p signals of P-HC before cycling. (b) Normalized spectra of ex situ XANES for P-HC anode before cycling and at different state of charge in one galvanostatic cycle of sodiation and desodiation.	61
4.4 Electrochemical studies of hard carbons in C/Na half-cells. (a) Sodiation/desodiation potential profiles of HC and P-HC. (b,c) CV curves during initial cycling at a scan rate of 0.1 mV/s (b) HC and (c) P-HC. (d) Cycling performance of P-HC. Inset in (d) is the rate performance of HC and P-HC electrodes	63
4.5 CV curves of two carbon anodes at a scan rate of 0.1 mV/s in a potential range of $0.01\text{-}2 \text{ V}$. (a) Pyrolyzed sucrose without addition of graphene oxide. (b) The 6th cycle CV curve of HC (GO was added).	64
4.6 X-ray diffraction and neutron total scattering studies of P-HC. (a,b) XRD results of HC and P-HC (a) Laboratory XRD patterns and (b) Synchrotron XRD patterns. (c-d) PDF results show local atomic order along ab planes (c) PDF within 5 \AA from neutron total scattering of HC and P-HC. (d) Schematic showing local pairs along graphene sheet.	65
4.7 Neutron total scattering results of HC and P-HC in a range of 20 \AA	67
4.8 Raman spectra of the (a) HC and (b) P-HC and their fitting curves with TPA (dark yellow), D (blue), A (wine), G (green).	68
5.1 SEM images of all carbon samples. (a) HC, (b) P-HC, (c) S-HC and (d) B-HC.	85

LIST OF FIGURES (Continued)

<u>Figure</u>	<u>Page</u>
5.2 High resolution XPS spectra of all carbons. (a) P 2p of P-HC, (b) B 1s of B-HC and (c) S 2p of S-HC.....	87
5.3 XRD studies of all carbons. After P- and S-doping, the (002) peak shifts to a lower angle, which indicates a larger d-spacing. However, B-doping barely shifts the peak.	88
5.4 TEM images of all carbons. (a) HC, (b) P-HC, (c) S-HC and (d) B-HC. All carbons demonstrate a non-graphitic structure comprising curved graphenic layers, where the lines are from the edge-view of the graphenic layers.....	89
5.5 Raman spectra of different carbon samples, which are deconvoluted into four Lorentzian peaks: TPA (dark yellow), D (blue), A (wine) and G (green). (a) HC, (b) P-HC, (c) S-HC and (d) B-HC.	91
5.6 Neutron total scattering and PDF studies of carbons. (a) PDF within 5 Å from neutron total scattering of HC, P-HC, B-HC and S-HC. (b) Schematic local structure of graphene.	93
5.7 Electrochemical performance of hard carbons in C/Na half-cells. (a) Galvanostatic sodiation/desodiation potential profiles of HC and doped hard carbons. (b) Sodiation/desodiation potential profiles of B-HC at current rate of 20 mA/g by charging it to 3.0 V and holding the potential at 3.0 V for 30 h. (c) Cycling performance of doped carbons	95
5.8 CV curves of various carbon anodes at a scan rate of 0.1 mV/s in a potential range of 0.01-2 V. (a) HC, (b) P-HC, (c) S-HC and (d) B-HC.	97
5.9 Comparison of charge distribution from (a) B-doped graphene sheet vs a pristine graphene sheet. (b) P-doped graphene sheet vs a pristine graphene sheet.....	100
5.10 Charge distribution plots of different graphene/Na systems simulated in VASP with the binding energies of sodium ions shown. (a) Pristine graphene. (b) P-doped graphene. (c) B-doped graphene.....	102
5.11 Charge distribution plots of different (a) Edge doped BC ₂ . (b) Edge doped PC ₂	102

LIST OF FIGURES (Continued)

<u>Figure</u>	<u>Page</u>
5.12 Charge distribution plots of (a) In-plane BC_3O . (b) Edge doped BCO_2 . (c) Edge BC_2O	103
5.13 Charge distribution plots of (a) In-plane PC_3O . (b) Edge doped PCO_2 . (c) Edge PC_2O	104
5.14 Charge distribution plots of (a) Edge doped $PC(OH)_2$. (b) Edge doped $PCO(OH)$	105
5.15 Charge distribution plots of different graphene/Na systems simulated in VASP. (a) Monovacancy graphene. (b) Divacancy graphene. (c) A large in-plane defect	106
6.1 First sodiation-desodiation profiles of hard carbon annealed at $600^\circ C$ before and after the microwave treatment at a current density of 20 mA/g.	121
6.2 (a, b) Nitrogen sorption isotherms and XRD patterns of all hard carbons. TEM images of (c) LT-HC, (d) HT-HC, and (e) Area-1 of MV-HC and (f) Area-2 of MV-HC.	122
6.3 SEM images of (a) LT-HC, (b) HT-HC, and (c) MV-HC.	123
6.4 (a) PDF studies associated with the neutron total scattering of LT-HC, HT-HC, and MV-HC. Deconvoluted Raman spectra of all hard carbons with four Lorentzian peaks: TPA (dark yellow), D (blue), A (wine) and G (green). (b) LT-HC, (c) HT-HC, and (d) MV-HC.	125
6.5 (a) The first-cycle galvanostatic sodiation/desodiation potential profiles of three hard carbons at a current rate of 20 mA/g. (b) Rate capability of three hard carbons at various current density in three-electrode cells. Long cycling performance of MV-HC at (c) 20 mA/g and (d) 200 mA/g.	127
6.6 Cyclic voltammetry results of (a) LT-HC and (b) MV-HC.	128
6.7 (a) First sodiation-desodiation potential profiles of hard carbon microwaved for 2 and 10 seconds at a current density of 20 mA/g. (b) Nitrogen sorption isotherms of MV-HC_2 and MV-HC-10.	130

LIST OF FIGURES (Continued)

<u>Figure</u>	<u>Page</u>
6.8	TEM images of (a) MV-HC_2 and (b) MV-HC_10. Deconvoluted Raman spectra of hard carbons with four Lorentzian peaks: TPA (dark yellow), D (blue), A (wine) and G (green). (c) MV-HC_2 and (d) MV-HC_10.....131
6.9	Schematic of three-electrode cell used for rate capability test.132
6.10	Diffusivity as a function of (de)sodiation potentials of hard carbons from GITT measurements (a) First sodiation. Inset: the low potential range, and (b) First desodiation.133
6.11	(a) First sodiation-desodiation potential profiles of LT-HC and MV-HC at a current density of 2 mA/g. (b) The potential profile of the GITT test at the potential of 0.12 V with the parameters labeled.....134
7.1	Schematic of the three-electrode cell setup.147
7.2	(a,b) XRD pattern and Raman spectrum of FP-HC. Raman spectrum was deconvoluted into four Lorentzian peaks: TPA (wine), D (blue), A (orange) and G (green). (c) TEM image of FP-HC.....148
7.3	(a-c) Sodiation-desodiation potential profiles of the fifth cycle of FP-HC at different current rates in (a) three-electrode cell, (b) half-cell, (c) Rate cycling performance of FP-HC in three-electrode cell and half-cell.149
7.4	Sodiation-desodiation potential profiles of FP-HC of the fifth cycle at different current rates in three-electrode cell. The Ewe and Ece vs. specific capacity are plotted. (a) The full sodiation-desodiation profiles (b) The zoomed-in sodiation-desodiation profiles.....151
7.5	Fifth cycle of potassiation-depotassiation profiles of FP-HC at different current rates in three-electrode cell for KIB. The Ewe and Ece vs. specific capacity are plotted. (a) The full potassiation-depotassiation profiles (b) The magnified potassiation-depotassiation profiles.152
8.1	(a) XRD patterns of all the obtained SCs. High-resolution TEM image of SC obtained by the pyrolysis of PTCDA at (b) 700°C (c) 900°C and (d) 1100°C..153
8.2	(a) PDF studies associated with the neutron total scattering of SC700, SC900 and hard carbons. Raman spectra of SCs, where the spectra were

LIST OF FIGURES (Continued)

<u>Figure</u>	<u>Page</u>
deconvoluted with four Lorentzian peaks: TPA (dark yellow), D (blue), A (wine) and G (green). (b) SC700, (c) SC900, and (d) SC1100.	164
8.3 Electrochemical performance of the SCs. (a) Potassiation/depotassiation potential profiles of all SCs at a current rate of 20 mA/g. (b) Rate capability of all SCs in the current range of 100 to 1000 mA/g. (c) Sodiation/desodiation profile of SC700 at a current of 20 mA/g. (d) Potassiation/depotassiation profile of SC700 at the cut-off potential of 0.25 V.	167
8.4 Different simulated graphene/K system with the charge distribution and binding energies shown. The green regions represent a negative charge and the yellow regions represent positive charges. (a) pristine graphene, (b) monovacancy graphene, (c) divacancy graphene.	170
8.5 (a) Cycling performance of SCs at different current rates of 20 mA/g. (b) Cycling performance of SCs at 100 mA/g after rate capability test at the current rates of 100, 200, 500 and 1000mA/g.	172

LIST OF TABLES

<u>Table</u>	<u>Page</u>
2.1 Comparison between lithium, sodium and potassium. ¹⁻⁴	9
5.1 Sodiation/desodiation capacities of HC and doped carbons and their capacities from plateau region and slope region.	96
5.2 Binding energy of Na-ions to pristine and doped graphene sheets.....	100
5.3 Binding energy of Na-ions to different defective graphene sheets.....	106
6.1 The first-cycle reversible Na-ion storage capacities of three hard carbons and the capacities from plateau and slope regions at current density of 20 mA/g.	128
8.1 Na-ion and K-ion binding energy with different structural sites.	170
8.2 Capacity retention of all SCs at different current rates.....	171

Chapter 1 Motivation

1.1 Grid-scale energy storage

Most of the terminal products of energy utilized by our society come in two forms: electricity and fossil fuels. Note that a large portion of the electricity is also generated by the combustion of fossil fuels. Fossil fuels have dominated the U.S. energy consumption for more than 100 years, where 81.5% of the energy consumption was made up by fossil fuels in 2015 (Figure 1).¹ However, the consumption of most fossil fuels always accompanied by the emission of CO₂ and some other pollutants which are posing serious issues on our environment. In addition, the fossil fuels cannot be regenerated once being consumed. On the other hand, electricity itself is clean energy even though the generation of electricity may involve CO₂ emission and other pollutions. Electricity provides a convenient way to transfer energy, and the future electrification of transportation will need much more energy terminal products in the form of electricity. By the centralized electricity generation, the efficiency of energy utilization can be improved, and the pollution issues can be mitigated. More importantly, the generation of electricity can be realized by clean and renewable energy sources such as hydropower, solar energy, and wind energy. Therefore, in order to increase the electricity supplies while reducing the CO₂ emission and mitigating environmental pollutions, it is highly desired to improve the electricity generation from these clean and renewable energy sources.

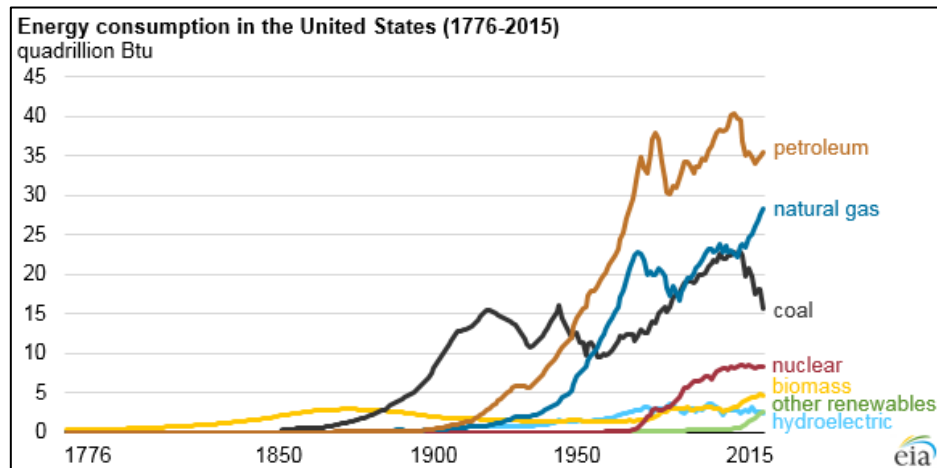


Figure 1.1 The resource composition of energy consumption in the United States from 1776 to 2015.¹

Even though there are lots of advantages of using electricity, electricity cannot be stored by the grid or its producer. All the electricity that once being produced has to be consumed. These clean and renewable energy technologies, especially the solar energy and wind energy are not available all the time which means that they cannot provide stable electricity supplies to the grid. Normally, the peak demand for electricity is in the evening, however, the peak solar electricity generation is in the noon. Therefore, it is highly necessary to integrate energy storage systems, which can store electricity when there is extra electricity available and give it back to the grid when it is needed, to the grid to take full advantage of these renewable energy supplies.

As we mentioned above, energy storage system can bridge up the gap between the electricity generation and consumption. However, that is not the only function of grid-scale energy storage systems. The modern society has a clear trend of electrification,

where the energy consumption in the form of electricity will substantially increase in the future. Particularly, the electrification of transportation which takes around 30% of the current total energy cost will dramatically increase the electricity needs and pose more strict requirements on the grid. Currently, in order to meet the peak demand for electricity, peaking plants must be deployed which have a very low utilization (5%-7%).² These peaking plants are either idling or being shut down during the other time. In addition, they have a rather slow response time which takes from minutes to hours. Grid disruptions would happen if the electricity supply and demand is not balanced, which could be caused by weather changes or some other unexpected issues. In the future, the needs of electricity will be much harder to predict. Imagine that if lots of electric vehicles charge at the same time, a huge burden will be put on the grid and this is hard to predict upon the future electrification of the transportation. The slow response of the peaking plants may lead to a grid disruption in this case. Therefore, a more flexible and rigid grid has to be developed to fit the future electricity market. Grid-scale energy storage systems integrated into the grid, which has a short response time, can address the vulnerabilities of current grid.

1.2 Grid-scale energy storage technologies

Energy storage systems have received much attention in recent years, which have promoted the development of different types of energy storage technologies. According to the principle of how the energy storage system runs, most of the current energy storage technologies can be sorted into two types: mechanical and chemical. Mechanical

energy storage technologies include pump hydro storage, compressed air storage and fly wheels storage which can convert the electricity into potential energy or kinetic energy at low demands and release it back to the grid as electricity at high demands. While these mechanical energy storage technologies are promising, their development are limited by the geographical locations, cost, safety or some other issues.^{3,4}

Chemical energy storage technologies which involve in the conversion between electric energy and chemical energy are promising solutions for grid-scale energy storage systems as they are cheaper, safer and easy to scale up comparing with mechanical energy storage technologies. Among different chemical energy storage technologies, Li-ion batteries (LIBs) have attracted most of the attention. However, the needs for LIBs have dramatically increased due to the high demands from portable electronic devices and electric vehicles. Particularly, the electrification of transportation will rely on LIBs in the near future which would exponentially increase the needs for LIBs. Unfortunately, Li is not an earth-abundant element and it is only concentrated in a few countries. Therefore, the grid-scale energy storage system would need other alternative energy storage technologies that operate with earth-abundant elements. Na-ion batteries (NIBs) and K-ion batteries (KIBs) which are operated with the similar mechanism with LIBs are emerging as alternative energy storage technologies that utilize earth-abundant elements. They have the potential to fit the needs for grid-scale energy storage.

1.3 Objectives of this thesis

Even though NIBs and KIBs have attracted much attention in recent years, they are still in their early stage comparing with LIBs, especially for KIBs. The commercialized anode, graphite, does not show meaningful capacity in NIBs and exhibits poor cycling performance in KIBs. Therefore, the development of other anode materials is urgent for the future commercialization of NIBs and KIBs. So far, non-graphitic carbons have been considered as the most promising anode materials for both NIBs and KIBs. According to the experience from LIBs, non-graphitic carbons most likely will be the anode materials for the first generation commercialized NIBs and KIBs.

The understanding of the mechanism of Na-ion and K-ion storage in non-graphitic carbons is highly desired to design and develop good anode materials for NIBs and KIBs. However, due to the complexity of the structure of non-graphitic carbons, the mechanistic understanding of Na-ion and K-ion storage in non-graphitic carbons is still limited. Therefore, the objective of this thesis is to study the structure-property correlations of Na-ion and K-ion storage in non-graphitic carbons to enable an in-depth mechanistic understanding of Na-ion and K-ion storage in non-graphitic carbon. This understanding would facilitate the design and development of better anode materials for NIBs and KIBs.

1.4 Reference

- (1) U.S. Energy Information Administration. **2016**, July, 1.

- (2) Association, E. S. 35x25 A Vision for Energy Storage. **2017**.
- (3) Aneke, M.; Wang, M. Energy storage technologies and real life applications – A state of the art review. *Applied Energy* **2016**, *179*, 350-377.
- (4) Zhao, H.; Wu, Q.; Hu, S.; Xu, H.; Rasmussen, C. N. Review of energy storage system for wind power integration support. *Applied Energy* **2015**, *137*, 545-553.

Chapter 2 Na-ion Batteries and K-ion Batteries

2.1 Background

Comparing with other state-of-art rechargeable battery technologies, LIBs can provide high energy density and stable cycling life. Since its first commercialization in 1990s, LIBs have been receiving more and more attention, and have become the dominant battery technologies in the market. Particularly, after being utilized in electric vehicles, it is expected that there will be a dramatic increase for the demand of LIBs as shown in Figure 2.1a. However, one major concern for the future development of LIBs is that lithium is not an earth-abundant element. There is only around 0.0065% lithium in the earth. More importantly, lithium is not evenly distributed around the world, where 70% of the lithium is concentrated in South America, and the extraction of lithium is difficult. Therefore, with the surging demand of LIBs, the price of lithium carbonate which is the precursor to produce lithium metal has substantially increased in recent years (Figure 2.1b). Since grid-scale energy storage system would need much more lithium resources, the application of LIBs in grid-scale energy storage system would aggravate the concerns for the shortage of lithium resources and increase the cost. Therefore, it is necessary to find other alternative energy storage devices with earth-abundant elements to address these concerns.

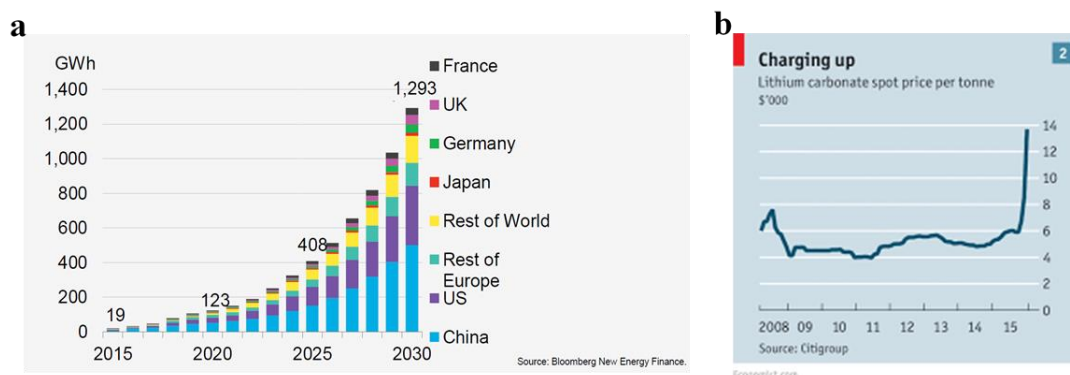


Figure 2.1 (a) The predicted demand for lithium-ion batteries from 2015 to 2030. (b) The price change of lithium carbonate.

2.2 Na-ion batteries

Sodium is in the same group with lithium which is just right below. Therefore, it shares lots of similar chemical properties with lithium. In addition, our earth crust contains around 2.74% sodium which is about 420 times of lithium and it is also much more evenly distributed around the world. The comparison between sodium *vs* lithium is summarized in table 1. It is obvious that the sodium precursor is much cheaper than lithium's. Sodium has a larger molar mass, higher density and higher redox potential which will lead to a lower energy density of NIBs than LIBs. Therefore, NIBs will not be able to compete with LIBs in terms of energy density, and thus may not be able to be used in portable electronics or electric vehicles. However, for grid-scale energy storage, energy density is not as important as the overall cost. Therefore, NIBs would be a promising alternative battery technology for grid-scale energy storage.

Table 2.1 Comparison between lithium, sodium and potassium.¹⁻⁴

	Lithium	Sodium	Potassium
Atomic Number	3	11	19
Atomic Mass [u]	6.941	22.9898	39.0983
Atomic Radius [pm]	145	180	220
Covalent Radius [pm]	128	166	203
Melting Point [°C]	180.54	97.72	63.38
Crust Abundance [mass %]	0.0017	2.3	1.5
Crust Abundance [molar %]	0.005	2.1	0.78
Voltage vs S.H.E. [V]	-3.04	-2.71	-2.93
Cost of carbonate [US\$ ton ⁻¹]	2300	200	1000
Cost of industrial grad metal [US\$ ton ⁻¹]	100000	3000	13000

The investigation of Na-ion batteries was started almost at the same time with LIBs which was back to 1970s.⁵⁻⁷ However, graphite, which was the anode for LIBs, does not show meaningful capacity upon the formation of binary graphite intercalation compounds (GICs). In addition, the commercialization of LIBs in 1990's made LIBs the most attracting battery technology and then much of the efforts were focused on LIBs. Therefore, the research on NIBs was chilled down. There were only a few publications on NIBs before 2000⁸⁻¹⁰ and it was only until 2010s, the research on NIBs resurged and has experienced an exponential increase since then.^{2, 11, 12} Part of the reasons for this resurging is that with a dramatic increase in the demand of LIBs, the price of lithium and its uneven distribution are becoming a serious concern. In addition,

the development of materials science technologies and the mature of LIBs technologies also boost the development of NIBs.

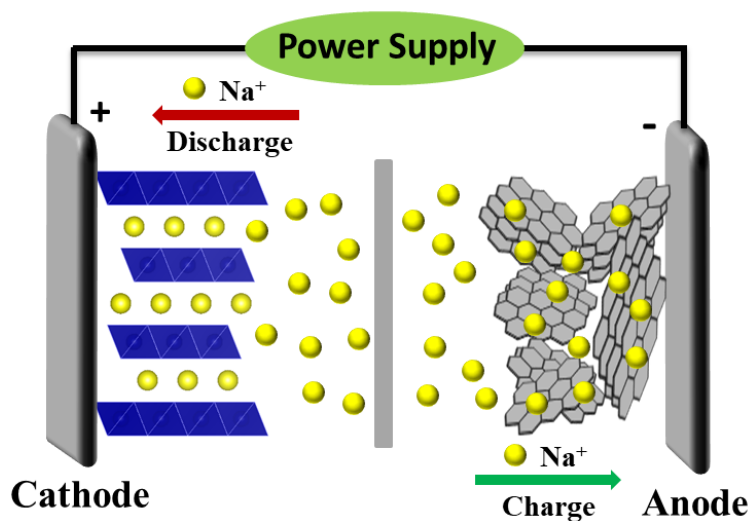


Figure 2.2 Schematic of Na-ion battery.

The schematic of NIB is shown in Figure 2.2. The components of NIBs are the same with LIBs which are cathode, anode, separator and electrolyte. In NIBs, the Na-ion shuttle between the cathode and anode. During the charging process, Na-ions are deinserted from the cathode into the electrolyte and then inserted into the anode. At the same time, the electrons are transferred from the cathode to the anode through the out circuit. The discharging process is just the reverse of the charging process, where Na-ion are deinserted from the anode into electrolyte and then inserted into the cathode. Even though NIBs share similar operational mechanism with LIBs, where some technologies can be transferred from LIBs into NIBs, there are still lots of differences between these two systems. First, the ionic radius of Li^+ is 0.076 nm where it is 0.102 nm for Na^+ . Second, the standard redox potential for Na^+/Na is -2.71 V vs standard

hydrogen electrode (SHE), where it is -3.04 for Li^+/Li vs SHE. These differences lead to new challenges in the development of NIBs. After being extensively investigated for about a decade, remarkable progress has been achieved for NIBs technologies.

2.2.1 Cathode Materials for NIBs

Cathode materials are the key component of rechargeable batteries. Guided by the mature research on LIBs cathodes, a large variety of NIBs cathodes materials have been studied, where some cathode materials show promising Na-ion storage performance. The most studied NIBs cathode materials can be classified into two different categories: layered transition metal oxides and polyanion compounds.^{13, 14}

2.2.1.1 Layered transition metal oxides as NIBs cathode

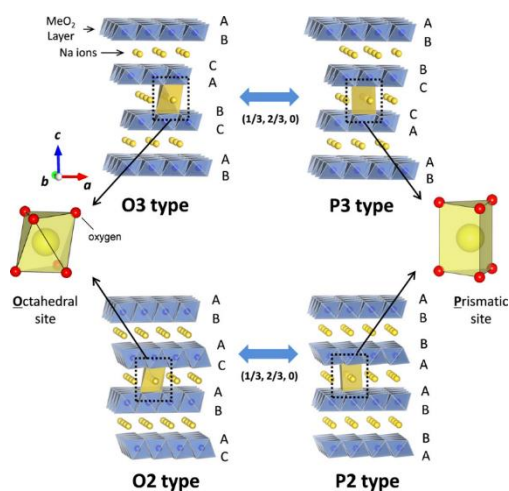


Figure 2.3 The structural schematic of different types of layered transition metal oxides Na_xMO_2 , where the sheet is composed of edge-sharing MeO_6 octahedra. The phase transition processes upon sodium extraction are also shown.¹⁵

Layered transition metal oxides materials are the most studied cathode materials as their Li analogues have been very successful in commercialized LIBs. The general formula of layered transition metal oxides is Na_xMO_2 , where M means the transition metal and it can be Ti, Cr, Mn, Fe, Co, Ni, etc. Typically, the layered transition metal oxide comprises alternatively stacked transition metal layer and Na-ion layer, where the transition metal layers are formed by edge sharing transition metal octahedra (MO_6). According to the surrounding environment of Na-ion site and the number of repeat transition metal layers, layered metal oxides can be grouped into four categories: O3, P3, O2, and P2.^{13, 15} Figure 2.3 shows the structural schematic of these four types of layered transition metal oxides. As shown in Figure 2.3, Na-ions occupy the prismatic sites in the P-type layered transition metal oxide and the Na-ions occupy the octahedral sites in the O-type layered transition metal oxides. So far, P2 and O3 phase layered transition metal oxides are the most studied NIBs cathode materials. In 1970s, Delmas *et al.* had studied the structural properties of Na_xMO_2 and in 1980s they further revealed that O3- Na_xCoO_2 show reversible phase transition upon Na-ion insertion/deinsertion.^{5, 7, 16} In 2010s, they also identified that P2- Na_xCoO_2 can experience reversible single-phase or two-phase transition at different Na-ion concentration (Figure 2.4).¹⁷ Even though the Li analogue of Na_xCoO_2 is widely used in the commercialized LIBs, the cycling performance of Na_xCoO_2 is not satisfied. In addition, most likely, the application of NIBs will be in grid-scale energy storage, where the cost is a key factor. Cobalt is becoming more and more expensive due to the widely application of LiCoO_2 as cathode material for LIBs. Therefore, in recent years, by replacing Co with other

transition metals such as Mn, Fe, Ni and Cr, various layered transition metal oxides have been studied.¹⁸⁻²³ Particularly, Na_xMnO_2 and Na_xFeO_2 that compose of cheap and abundant transition metals are attractive cathode material candidates for NIBs. It has been reported that Na_xFeO_2 exhibit 80 mAh/g reversible capacity under 3.4 V with good cycling stability.²⁰ Na_xMnO_2 with high theoretical capacity has demonstrated a high reversible capacity of ~ 180 mAh/g.²¹ However, the cycling stability of Na_xMnO_2 suffers from its fast structural degradation upon Na-ion insertion/deinsertion. Most of these single transition metal oxides-based cathode materials have their own disadvantages. Therefore, layered transition metal oxides cathode with combinatory transition metals have been developed to improve the overall Na-ion storage performance.

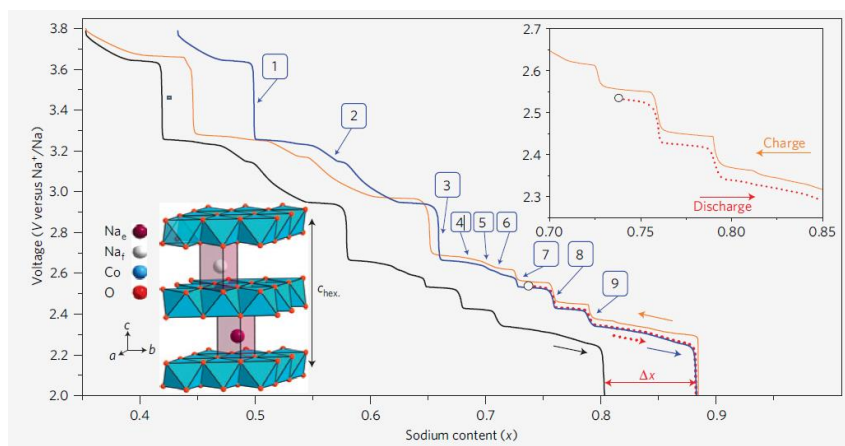


Figure 2.4 Galvanostatic sodiation-desodiation curve of $\text{P}_2\text{-Na}_x\text{CoO}_2$. The bottom left inset is the schematic of the structure of $\text{P}_2\text{-Na}_x\text{CoO}_2$ and the top right inset is enlarged galvanostatic sodiation-desodiation curve.¹⁷

2.2.1.2 Polyanion compounds as NIBs cathode

Compared with layered transition metal oxides, polyanion compounds have been shown stable cycling performance and tunable operation potential.^{14, 24} The strong X-O bond in the tetrahedral polyanion structure unit $(XO_4)^{n-}$ or $(X_mO_{3m+1})^{n-}$ ($X = P$ or S) provides the structural stability of polyanion compounds. Among various types of polyanion compounds, phosphates, pyrophosphates, fluorophosphates, and sulphates are the most popular ones.

The olivine type $LiFePO_4$, the Li analogue of $NaFePO_4$, has been widely applied as cathode materials for commercialized LIBs due to its stable cycling performance and low cost.^{25, 26} However, the most thermodynamically stable phase of $NaFePO_4$ is not olivine $NaFePO_4$ but maricite.²⁷ Unfortunately, the maricite is not electrochemically active for Na-ion storage due to the fact that it does not have the Na-ion diffusion channels.²⁸ Therefore, lots of efforts have been devoted to the synthesis of olivine $NaFePO_4$ by ion-exchange from $LiFePO_4$ which shows a reversible capacity of ~ 125 mAh/g.²⁸⁻³⁰ Recently, it was revealed that nanosized maricite $NaFePO_4$ can deliver a high capacity of ~ 142 mAh/g with good cycling stability.³¹ In addition, amorphous $FePO_4$ has also been demonstrated with a reversible capacity of ~ 150 mAh/g.³²

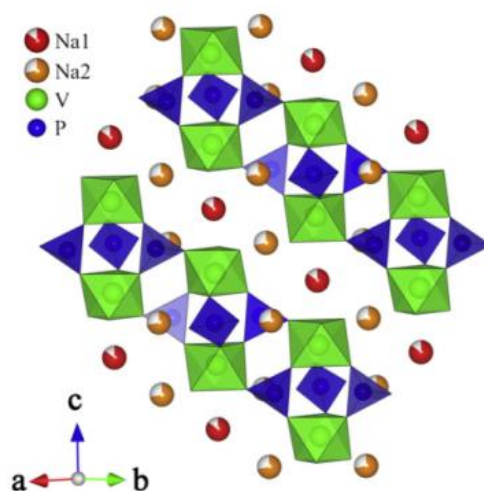


Figure 2.5 Unit cell structure of $\text{Na}_3\text{V}_2(\text{PO}_4)_3$.³³

Phosphates with NASICON framework, particularly $\text{Na}_3\text{V}_2(\text{PO}_4)_3$, have been extensively studied as cathode materials for NIBs.^{34, 35} In $\text{Na}_3\text{V}_2(\text{PO}_4)_3$, one octahedral VO_6 is surrounded by three PO_4 tetrahedrons via corner-sharing to form a three-dimensional open framework with large Na-ion diffusion channels (Figure 2.5). In 2010, $\text{Na}_3\text{V}_2(\text{PO}_4)_3$ was first reported as NIBs cathode material by Yamaki *et al.*, where it delivered a capacity of 140 mAh/g in the voltage range of 1.2-3.5 V.³⁶ However, due to the poor electronic conductivity, the overall Na-ion storage performance of $\text{Na}_3\text{V}_2(\text{PO}_4)_3$ still needs to be further improved. Later, Jian *et al.* synthesized carbon coated $\text{Na}_3\text{V}_2(\text{PO}_4)_3$ which demonstrated a reversible capacity of 93 mAh/g with a flat plateau at 3.4 V, and the carbon coating also improved the cycling performance of the obtained $\text{Na}_3\text{V}_2(\text{PO}_4)_3$.³³ Recently, research on Fe or Mg doping of $\text{Na}_3\text{V}_2(\text{PO}_4)_3$ has also been proved to be effective to improve its electrochemical performance.^{37, 38}

2.2.2 Anode materials for NIBs

In LIBs, graphite is the dominant anode material which accounts for around 89% of the total LIBs anode market due to its low-cost, stable cycling performance and decent capacity with low potential.³⁹ Unfortunately, graphite does not show meaningful capacity in NIBs unless expanded graphite or solvent-cointercalation is conducted.^{40, 41} Therefore, it is highly necessary to develop other type of anode materials for NIBs. So far, carbonaceous materials are the most promising anode materials for NIBs, and other type of anode materials including alloy type anode materials, low-potential transition metal oxides and organic materials have also been developed.

2.2.2.1 Non-graphitic carbon materials as NIBs anode

Hard carbon is one of the most promising NIBs anode. It comprises of short range ordered nanodomains which are stack of graphene sheets and voids in between the nanodomains. It is also known as non-graphitizable carbon as it will remain amorphous even it is pyrolyzed under high temperature (>2800 °C).⁴² Hard carbon was first applied in NIBs in 2000 by Stevens and Dahn which showed a reversible capacity of ~ 300 mAh/g.^{43, 44} They identified that during the charge-discharge, hard carbon showed two distinct regions, namely, the low-potential plateau region (0-0.2 V) and the high-potential slope region (0.2-1 V). In this study, they attributed the low-potential plateau region to Na-ion adsorption into the pores between the nanodomains, and the high-potential slope region to Na-ion insertion into the nanodomains which was called a “house of cards” model. Started in early 2010s, much attention has been devoted into

hard carbon anode, where different explanations and models have been proposed for the interaction between Na-ions and the hard carbon structure.⁴⁵⁻⁵² Various types of precursors and synthetic methods have been studied for the preparation of hard carbon, and the Na-ion storage performance of hard carbon had been improved.^{43, 45, 46, 53, 54}

In addition to hard carbon, soft carbons have also been proved to be promising NIBs anode materials. In contrast to hard carbon, soft carbon is graphitizable non-graphitic carbon that can be turned into ordered structure by annealing at high temperatures. Doeff *et al.* first revealed that petroleum coke derived soft carbon has a reversible Na-ion storage capacity of ~90 mAh/g which corresponds to the formation of NaC₂₄.⁸ Recently, our group studied 3,4,9,10-perylene-tetracarboxylic acid-dianhydride (PTCDA) derived soft carbon as anode for Na-ion storage.⁵⁵ By tuning the pyrolysis temperatures, we were able to tune the interlayer distance of the obtained soft carbon which was found to be an important factor that affects its Na-ion storage performance. The soft carbon obtained at 900 °C delivered a reversible capacity of 197 mAh/g at 20 mA/g. It also demonstrated excellent rate capability, where at 1000 mA/g it still maintained a capacity of 114 mAh/g. Unlike hard carbon, soft carbon does not show a low-potential plateau. This would sacrifice the energy density of full cell. However, it also lowers the risk of dendrite formation and the related safety concerns.

2.3 K-ion batteries

As we mentioned earlier, alternative energy storage devices with earth-abundant and cheap elements are highly desired for grid-scale energy storage, where NIBs and Mg-ion batteries have received dramatically increased attention.^{2, 12, 52, 56, 57} Interestingly, even though potassium is also in the same group with lithium which is right below sodium, not too much attention was paid to K-ion batteries (KIBs) until the first report of graphite anode for KIBs.⁵⁸ The facts that potassium is highly reactive, it is much heavier than lithium and sodium, and its radius size is also much larger than lithium and sodium may explain why KIBs did not receive too much attention as an alternative energy storage device (see table 1). However, it is not fair to just compare the formula weight of the alkali-metal when considering the energy density. First, for the positive electrode, it not only contains the alkali-metal but also other elements which are much heavier than alkali in total. Second, one cannot only think about the energy density of electrodes but also need to take the full configuration of the cell into account when considering at a full-cell scale. Therefore, the overall energy density of KIBs may be comparable with LIBs, and it should be on par with NIBs.

In addition, KIBs have some unique advantages over LIBs and NIBs. Potassium has similar abundance with sodium which is much higher than lithium. The cost of potassium is much smaller than lithium, and the cost of common electrolytes for KIBs is also much lower than the electrolytes for LIBs (Table 1). It is also worth to note that, unlike lithium, potassium does not form alloy with aluminum under low potentials

which means that cheaper aluminum current collector can be used instead of copper for the anode.⁵⁹ It has been well-known that the standard potentials of Li^+/Li , Na^+/Na and K^+/K are -3.040 , -2.714 , and -2.936 V vs SHE, respectively, where the K^+/K redox couple shows a lower redox potential than Na^+/Na . In addition, it has been revealed by both theoretical calculation and experimental measurements that the K^+/K redox couple has the lowest potential compare with Li^+/Li and Na^+/Na in some non-aqueous electrolytes.^{60, 61} For instance, in propylene carbonate (PC) the standard potential of Li^+/Li , Na^+/Na and K^+/K are -2.79 , -2.56 and -2.88 V, respectively.⁶⁰ This low potential of the K^+/K couple could enable a higher cell voltage of KIBs. Surprisingly, even though graphite does not show meaningful capacity in NIBs, it delivers a decent reversible capacity in KIBs regardless of the fact that the size of K^+ is much larger than Na^+ .^{58, 61, 62} Since our group first reported that graphite can reversibly store K^+ , the research in KIBs has exponentially increased. On the anode side, except graphite, other carbonaceous materials and some noncarbon based materials have been studied as anode for KIBs.⁶³⁻⁶⁶ On the cathode, Prussian blue analogues have been the leading materials for KIBs.⁶⁷⁻⁶⁹ Some other layered metal oxides and polyanion compounds have also been developed.⁷⁰⁻⁷³

2.3.1 Graphite as anode for KIBs

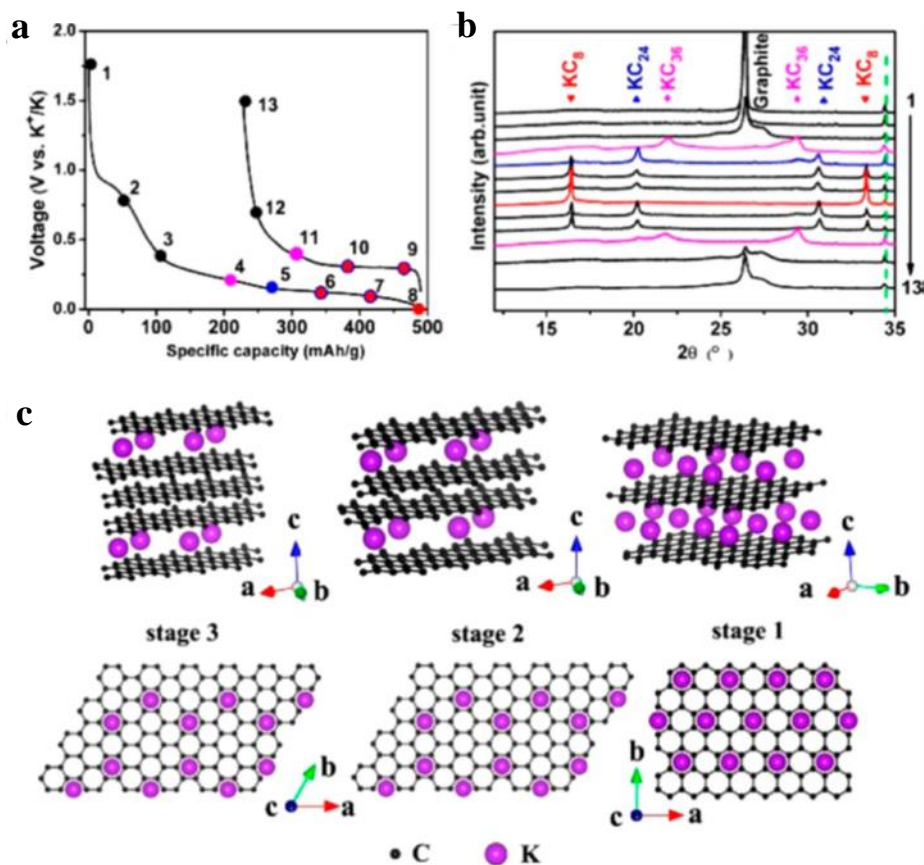


Figure 2.6 (a) First-cycle galvanostatic potassiation/depotassiation potential profiles at C/10. (b) XRD patterns of electrodes corresponding to the marked SOCs in A. (c) Structure diagrams of different K-GICs, side view (top row) and top view (bottom row).⁵⁸

The early study on K-graphite intercalation compounds (GICs) can date back to 1932, and stage one GIC, KC₈, has been synthesized by chemical method.⁷⁴⁻⁷⁷ In GIC chemistry, stage number means the number of graphene layers in between two adjacent intercalation layer, where stage one GICs means that there is an intercalation layer in

every graphene layer. Various staged K-GICs have been synthesized by either vapor-phase synthesis techniques or by soaking potassium metal in organic solvents, where stage two KC_{24} , stage three KC_{36} and stage four KC_{48} have been identified.^{78,79} However, electrochemical intercalation of K into graphite had not been reported until 2015, when our group proved the reversible electrochemical intercalation of K into graphite at room temperature.⁵⁸ In this study, by using synthetic graphite, a reversible K-ion storage capacity of 273 mAh/g was achieved which is close to the theoretical capacity of forming KC_8 (Figure 2.6a). Via ex situ x-ray diffraction (XRD), reversible staging phenomena was revealed upon potassiation/depotassiation, where stage three KC_{36} , stage two KC_{24} and stage one KC_8 were identified (Figure 2.6b, c). Later, Komaba et al. and Hu et al. also reported reversible intercalation of K into graphite, where Komaba et al. also revealed that binder and electrolyte have great impacts on the first cycle coulombic efficiency of graphite for K-ion storage.^{61, 62} The potassium intercalation potential revealed in these studies was around 0.2 V which is higher than that of lithium and thus lowers the risk of potassium metal plating and the related safety issues. By looking into these reports, it is evident that the cycling performance of K-ion storage in graphite is much worse than the case in LIBs. It is found that with the interlayer d-spacing expanded from 3.35 Å to 5.35 Å upon full potassiation, the volume expansion of graphite anode is around ~60%. This huge volume expansion is one of the main reasons that lead to the poor cycling performance of graphite. The poor cycling performance of graphite anode could plague the future commercialization of KIBs.

2.4 Reference

- (1) Sawicki, M.; Shaw, L. L. Advances and challenges of sodium ion batteries as post lithium ion batteries. *RSC Advances* **2015**, *5*, 53129-53154.
- (2) Pan, H.; Hu, Y.-S.; Chen, L. Room-temperature stationary sodium-ion batteries for large-scale electric energy storage. *Energy Environ. Sci.* **2013**, *6*, 2338-2360.
- (3) Martin, G.; Rentsch, L.; Hoeck, M.; Bertau, M. Lithium market research—global supply, future demand and price development. *Energy Storage Mater.* **2017**, *6*, 171-179.
- (4) Pramudita, J. C.; Sehrawat, D.; Goonetilleke, D.; Sharma, N. An Initial Review of the Status of Electrode Materials for Potassium-Ion Batteries. *Adv. Energy Mater.* **2017**, *7*, 160291.
- (5) Delmas, C.; Fouassier, C.; Hagenmuller, P. Structural classification and properties of the layered oxides. *Physica B+C* **1980**, *99*, 81-85.
- (6) Whittingham, M. S. Chemistry of intercalation compounds: metal guests in chalcogenide hosts. *Prog. Solid State Chem.* **1978**, *12*, 41-99.
- (7) Delmas, C.; Braconnier, J.-J.; Fouassier, C.; Hagenmuller, P. Electrochemical intercalation of sodium in Na_xCoO_2 bronzes. *Solid State Ionics* **1981**, *3*, 165-169.
- (8) Doeff, M. M.; Ma, Y.; Visco, S. J.; De Jonghe, L. C. Electrochemical insertion of sodium into carbon. *J. Electrochem. Soc.* **1993**, *140*, L169-L170.
- (9) Spahr, M.; Novak, P.; Haas, O.; Nesper, R. Electrochemical insertion of lithium, sodium, and magnesium in molybdenum(VI) oxide. *J. Power Sources* **1995**, *54*, 346-351.
- (10) Dubois, M.; Ghanbaja, J.; Billaud, D. Electrochemical intercalation of sodium ions into poly(para-phenylene) in carbonate-based electrolytes. *Synth. Met.* **1997**, *90*, 127-134.
- (11) Kim, S. W.; Seo, D. H.; Ma, X.; Ceder, G.; Kang, K. Electrode materials for rechargeable sodium-ion batteries: potential alternatives to current lithium-ion batteries. *Adv. Energy Mater.* **2012**, *2*, 710-721.
- (12) Yabuuchi, N.; Kubota, K.; Dahbi, M.; Komaba, S. Research development on sodium-ion batteries. *Chem. Rev.* **2014**, *114*, 11636-11682.
- (13) Wang, P. F.; You, Y.; Yin, Y. X.; Guo, Y. G. Layered Oxide Cathodes for Sodium-Ion Batteries: Phase Transition, Air Stability, and Performance. *Adv. Energy Mater.* **2018**, *8*, 1701912.
- (14) Ni, Q.; Bai, Y.; Wu, F.; Wu, C. Polyanion-Type Electrode Materials for Sodium-Ion Batteries. *Adv. Sci.* **2017**, *4*, 1600275
- (15) Yabuuchi, N.; Komaba, S. Recent research progress on iron-and manganese-based positive electrode materials for rechargeable sodium batteries. *Sci. Technol. Adv. Mater.* **2014**, *15*, 043501.

- (16) Fouassier, C.; Delmas, C.; Hagemuller, P. Evolution structurale et proprietes physiques des phases A_xMO_2 ($A = Na, K; M = Cr, Mn, Co$) ($x \leq 1$). *Mater. Res. Bull.* **1975**, *10*, 443-449.
- (17) Berthelot, R.; Carlier, D.; Delmas, C. Electrochemical investigation of the $P2-Na_xCoO_2$ phase diagram. *Nat. Mater.* **2011**, *10*, 74-80.
- (18) Komaba, S.; Takei, C.; Nakayama, T.; Ogata, A.; Yabuuchi, N. Electrochemical intercalation activity of layered $NaCrO_2$ vs. $LiCrO_2$. *Electrochem. Commun.* **2010**, *12*, 355-358.
- (19) Ding, J.-J.; Zhou, Y.-N.; Sun, Q.; Fu, Z.-W. Cycle performance improvement of $NaCrO_2$ cathode by carbon coating for sodium ion batteries. *Electrochem. Commun.* **2012**, *22*, 85-88.
- (20) Yabuuchi, N.; Yoshida, H.; Komaba, S. Crystal structures and electrode performance of α - $NaFeO_2$ for rechargeable sodium batteries. *Electrochemistry* **2012**, *80*, 716-719.
- (21) Ma, X.; Chen, H.; Ceder, G. Electrochemical properties of monoclinic $NaMnO_2$. *J. Electrochem. Soc.* **2011**, *158*, A1307-A1312.
- (22) Lu, Z.; Dahn, J. In Situ X-Ray Diffraction Study of $P2 Na_{2/3}[Ni_{1/3}Mn_{2/3}]O_2$. *J. Electrochem. Soc.* **2001**, *148*, A1225-A1229.
- (23) Yoshida, H.; Yabuuchi, N.; Kubota, K.; Ikeuchi, I.; Garsuch, A.; Schulz-Dobrick, M.; Komaba, S. $P2$ -type $Na_{2/3}Ni_{1/3}Mn_{2/3-x}Ti_xO_2$ as a new positive electrode for higher energy Na-ion batteries. *Chem. Commun.* **2014**, *50*, 3677-3680.
- (24) Ha, K. H.; Woo, S. H.; Mok, D.; Choi, N. S.; Park, Y.; Oh, S. M.; Kim, Y.; Kim, J.; Lee, J.; Nazar, L. F. $Na_{4-\alpha}M_{2+\alpha/2}(P_2O_7)_2$ ($2/3 \leq \alpha \leq 7/8$, $M = Fe, Fe_{0.5}Mn_{0.5}, Mn$): A Promising Sodium Ion Cathode for Na-ion Batteries. *Adv. Energy Mater.* **2013**, *3*, 770-776.
- (25) Padhi, A. K.; Nanjundaswamy, K. S.; Goodenough, J. B. Phospho-olivines as positive-electrode materials for rechargeable lithium batteries. *J. Electrochem. Soc.* **1997**, *144*, 1188-1194.
- (26) Padhi, A.; Nanjundaswamy, K.; Masquelier, C.; Okada, S.; Goodenough, J. Effect of structure on the Fe^{3+}/Fe^{2+} redox couple in iron phosphates. *J. Electrochem. Soc.* **1997**, *144*, 1609-1613.
- (27) Bridson, J. N.; Quinlan, S. E.; Tremaine, P. R. Synthesis and crystal structure of maricite and sodium iron (III) hydroxyphosphate. *Chem. Mater.* **1998**, *10*, 763-768.
- (28) Zaghbi, K.; Trottier, J.; Hovington, P.; Brochu, F.; Guerfi, A.; Mauger, A.; Julien, C. Characterization of Na-based phosphate as electrode materials for electrochemical cells. *J. Power Sources* **2011**, *196*, 9612-9617.
- (29) Moreau, P.; Guyomard, D.; Gaubicher, J.; Boucher, F. Structure and stability of sodium intercalated phases in olivine $FePO_4$. *Chem. Mater.* **2010**, *22*, 4126-4128.

- (30) Oh, S.-M.; Myung, S.-T.; Hassoun, J.; Scrosati, B.; Sun, Y.-K. Reversible NaFePO₄ electrode for sodium secondary batteries. *Electrochem. Commun.* **2012**, *22*, 149-152.
- (31) Kim, J.; Seo, D.-H.; Kim, H.; Park, I.; Yoo, J.-K.; Jung, S.-K.; Park, Y.-U.; Goddard III, W. A.; Kang, K. Unexpected discovery of low-cost maricite NaFePO₄ as a high-performance electrode for Na-ion batteries. *Energy Environ. Sci.* **2015**, *8*, 540-545.
- (32) Li, C.; Miao, X.; Chu, W.; Wu, P.; Tong, D. G. Hollow amorphous NaFePO₄ nanospheres as a high-capacity and high-rate cathode for sodium-ion batteries. *J. Mater. Chem. A* **2015**, *3*, 8265-8271.
- (33) Jian, Z.; Zhao, L.; Pan, H.; Hu, Y.-S.; Li, H.; Chen, W.; Chen, L. Carbon coated Na₃V₂(PO₄)₃ as novel electrode material for sodium ion batteries. *Electrochem. Commun.* **2012**, *14*, 86-89.
- (34) Anantharamulu, N.; Rao, K. K.; Rambabu, G.; Kumar, B. V.; Radha, V.; Vithal, M. A wide-ranging review on NASICON type materials. *J Mater Sci* **2011**, *46*, 2821-2837.
- (35) Jian, Z.; Hu, Y. S.; Ji, X.; Chen, W. NASICON-structured materials for energy storage. *Adv. Mater.* **2017**, *29*, 1601925.
- (36) Plashnitsa, L. S.; Kobayashi, E.; Noguchi, Y.; Okada, S.; Yamaki, J.-i. Performance of NASICON symmetric cell with ionic liquid electrolyte. *J. Electrochem. Soc.* **2010**, *157*, A536-A543.
- (37) Li, H.; Yu, X.; Bai, Y.; Wu, F.; Wu, C.; Liu, L.-Y.; Yang, X.-Q. Effects of Mg doping on the remarkably enhanced electrochemical performance of Na₃V₂(PO₄)₃ cathode materials for sodium ion batteries. *J. Mater. Chem. A* **2015**, *3*, 9578-9586.
- (38) Aragon, M.; Lavela, P.; Ortiz, G.; Tirado, J. Effect of iron substitution in the electrochemical performance of Na₃V₂(PO₄)₃ as cathode for Na-ion batteries. *J. Electrochem. Soc.* **2015**, *162*, A3077-A3083.
- (39) Schmuch, R.; Wagner, R.; Hörpel, G.; Placke, T.; Winter, M. Performance and cost of materials for lithium-based rechargeable automotive batteries. *Nature Energy* **2018**, *3*, 267.
- (40) Jache, B.; Adelhelm, P. Use of Graphite as a Highly Reversible Electrode with Superior Cycle Life for Sodium-Ion Batteries by Making Use of Co-Intercalation Phenomena. *Angew. Chem. Int. Ed.* **2014**, *53*, 10169-10173.
- (41) Wen, Y.; He, K.; Zhu, Y.; Han, F.; Xu, Y.; Matsuda, I.; Ishii, Y.; Cumings, J.; Wang, C. Expanded graphite as superior anode for sodium-ion batteries. *Nat. Commun.* **2014**, *5*, 4033.
- (42) Franklin, R. E. Crystallite growth in graphitizing and non-graphitizing carbons. *Proc. R. Soc. London, Ser.* **1951**, *209*, 196-218.
- (43) Stevens, D.; Dahn, J. High Capacity Anode Materials for Rechargeable Sodium-Ion Batteries. *J. Electrochem. Soc.* **2000**, *147*, 1271-1273.

- (44) Stevens, D.; Dahn, J. An In Situ Small-Angle X-Ray Scattering Study of Sodium Insertion into a Nanoporous Carbon Anode Material within an Operating Electrochemical Cell. *J. Electrochem. Soc.* **2000**, *147*, 4428-4431.
- (45) Ding, J.; Wang, H.; Li, Z.; Kohandehghan, A.; Cui, K.; Xu, Z.; Zahiri, B.; Tan, X.; Lotfabad, E. M.; Olsen, B. C. Carbon nanosheet frameworks derived from peat moss as high performance sodium ion battery anodes. *ACS Nano* **2013**, *7*, 11004-11015.
- (46) Lotfabad, E. M.; Ding, J.; Cui, K.; Kohandehghan, A.; Kalisvaart, W. P.; Hazelton, M.; Mitlin, D. High-density sodium and lithium ion battery anodes from banana peels. *ACS Nano* **2014**, *8*, 7115-7129.
- (47) Li, Z.; Bommier, C.; Chong, Z. S.; Jian, Z.; Surta, T. W.; Wang, X.; Xing, Z.; Neufeind, J. C.; Stickle, W. F.; Dolgos, M. Mechanism of Na-Ion Storage in Hard Carbon Anodes Revealed by Heteroatom Doping. *Adv. Energy Mater.* **2017**, *7*, 1602894.
- (48) Qiu, S.; Xiao, L.; Sushko, M. L.; Han, K. S.; Shao, Y.; Yan, M.; Liang, X.; Mai, L.; Feng, J.; Cao, Y. Manipulating Adsorption–Insertion Mechanisms in Nanostructured Carbon Materials for High-Efficiency Sodium Ion Storage. *Adv. Energy Mater.* **2017**, *7*, 1700403.
- (49) Zhang, B.; Ghimbeu, C. M.; Laberty, C.; Vix-Guterl, C.; Tarascon, J. M. Correlation between microstructure and Na storage behavior in hard carbon. *Adv. Energy Mater.* **2016**, *6*, 1501588.
- (50) Komaba, S.; Murata, W.; Ishikawa, T.; Yabuuchi, N.; Ozeki, T.; Nakayama, T.; Ogata, A.; Gotoh, K.; Fujiwara, K. Electrochemical Na insertion and solid electrolyte interphase for hard-carbon electrodes and application to Na-Ion batteries. *Adv. Funct. Mater.* **2011**, *21*, 3859-3867.
- (51) Bommier, C.; Surta, T. W.; Dolgos, M.; Ji, X. New mechanistic insights on Na-ion storage in nongraphitizable carbon. *Nano Lett.* **2015**, *15*, 5888-5892.
- (52) Cao, Y.; Xiao, L.; Sushko, M. L.; Wang, W.; Schwenzler, B.; Xiao, J.; Nie, Z.; Saraf, L. V.; Yang, Z.; Liu, J. Sodium ion insertion in hollow carbon nanowires for battery applications. *Nano Lett.* **2012**, *12*, 3783-3787.
- (53) Li, Y.; Hu, Y. S.; Titirici, M. M.; Chen, L.; Huang, X. Hard Carbon Microtubes Made from Renewable Cotton as High-Performance Anode Material for Sodium-Ion Batteries. *Adv. Energy Mater.* **2016**, *6*, 1600659.
- (54) Shen, F.; Luo, W.; Dai, J.; Yao, Y.; Zhu, M.; Hitz, E.; Tang, Y.; Chen, Y.; Sprenkle, V. L.; Li, X., et al. Ultra-Thick, Low-Tortuosity, and Mesoporous Wood Carbon Anode for High-Performance Sodium-Ion Batteries. *Adv. Energy Mater.* **2016**, *6*, 1600377.
- (55) Luo, W.; Jian, Z.; Xing, Z.; Wang, W.; Bommier, C.; Lerner, M. M.; Ji, X. Electrochemically expandable soft carbon as anodes for Na-ion batteries. *ACS Cent. Sci.* **2015**, *1*, 516-522.

- (56) Shao, Y.; Gu, M.; Li, X.; Nie, Z.; Zuo, P.; Li, G.; Liu, T.; Xiao, J.; Cheng, Y.; Wang, C. Highly reversible Mg insertion in nanostructured Bi for Mg ion batteries. *Nano Lett.* **2013**, *14*, 255-260.
- (57) Aurbach, D.; Lu, Z.; Schechter, A.; Gofer, Y.; Gizbar, H.; Turgeman, R.; Cohen, Y.; Moshkovich, M.; Levi, E. Prototype systems for rechargeable magnesium batteries. *Nature* **2000**, *407*, 724-727.
- (58) Jian, Z.; Luo, W.; Ji, X. Carbon electrodes for K-ion batteries. *J. Am. Chem. Soc.* **2015**, *137*, 11566-11569.
- (59) Eftekhari, A.; Jian, Z.; Ji, X. Potassium secondary batteries. *ACS Appl. Mater. Interfaces* **2016**, *9*, 4404-4419.
- (60) Matsuura, N.; Umemoto, K.; Takeuchi, Z. i. Standard potentials of alkali metals, silver, and thallium metal/ion couples in N, N'-dimethylformamide, dimethyl sulfoxide, and propylene carbonate. *Bull. Chem. Soc. Jpn.* **1974**, *47*, 813-817.
- (61) Komaba, S.; Hasegawa, T.; Dahbi, M.; Kubota, K. Potassium intercalation into graphite to realize high-voltage/high-power potassium-ion batteries and potassium-ion capacitors. *Electrochem. Commun.* **2015**, *60*, 172-175.
- (62) Luo, W.; Wan, J.; Ozdemir, B.; Bao, W.; Chen, Y.; Dai, J.; Lin, H.; Xu, Y.; Gu, F.; Barone, V. Potassium ion batteries with graphitic materials. *Nano Lett.* **2015**, *15*, 7671-7677.
- (63) Jian, Z.; Xing, Z.; Bommier, C.; Li, Z.; Ji, X. Hard Carbon Microspheres: Potassium-Ion Anode Versus Sodium-Ion Anode. *Adv. Energy Mater.* **2016**, *6*, 1501874.
- (64) Jian, Z.; Hwang, S.; Li, Z.; Hernandez, A. S.; Wang, X.; Xing, Z.; Su, D.; Ji, X. Hard-Soft Composite Carbon as a Long-Cycling and High-Rate Anode for Potassium-Ion Batteries. *Adv. Funct. Mater.* **2017**, *27*, 1700324.
- (65) Share, K.; Cohn, A. P.; Carter, R.; Rogers, B.; Pint, C. L. Role of nitrogen-doped graphene for improved high-capacity potassium ion battery anodes. *ACS Nano* **2016**, *10*, 9738-9744.
- (66) Zhang, W.; Mao, J.; Li, S.; Chen, Z.; Guo, Z. Phosphorus-based alloy materials for advanced potassium-ion battery anode. *J. Am. Chem. Soc.* **2017**, *139*, 3316-3319.
- (67) Wu, X.; Jian, Z.; Li, Z.; Ji, X. Prussian white analogues as promising cathode for non-aqueous potassium-ion batteries. *Electrochem. Commun.* **2017**, *77*, 54-57.
- (68) Liao, J.; Hu, Q.; Yu, Y.; Wang, H.; Tang, Z.; Wen, Z.; Chen, C. A potassium-rich iron hexacyanoferrate/dipotassium terephthalate@ carbon nanotube composite used for K-ion full-cells with an optimized electrolyte. *J. Mater. Chem. A* **2017**, *5*, 19017-19024.
- (69) Bie, X.; Kubota, K.; Hosaka, T.; Chihara, K.; Komaba, S. A novel K-ion battery: hexacyanoferrate (II)/graphite cell. *J. Mater. Chem. A* **2017**, *5*, 4325-4330.

- (70) Hironaka, Y.; Kubota, K.; Komaba, S. P2-and P3-K_xCoO₂ as an electrochemical potassium intercalation host. *Chem. Commun.* **2017**, *53*, 3693-3696.
- (71) Kim, H.; Kim, J. C.; Bo, S. H.; Shi, T.; Kwon, D. H.; Ceder, G. K-Ion Batteries Based on a P2-Type K_{0.6}CoO₂ Cathode. *Adv. Energy Mater.* **2017**, *7*, 1700098.
- (72) Lin, X.; Huang, J.; Tan, H.; Huang, J.; Zhang, B. K₃V₂(PO₄)₂F₃ as a Robust Cathode for Potassium-Ion Batteries. *Energy Storage Mater.* **2019**, *16*, 97-101.
- (73) Han, J.; Niu, Y.; Bao, S.-j.; Yu, Y.-N.; Lu, S.-Y.; Xu, M. Nanocubic KTi₂(PO₄)₃ electrodes for potassium-ion batteries. *Chem. Commun.* **2016**, *52*, 11661-11664.
- (74) Lerf, A. Storylines in intercalation chemistry. *Dalton Transactions* **2014**, *43*, 10276-10291.
- (75) Dresselhaus, M. S.; Dresselhaus, G. Intercalation compounds of graphite. *Adv Phys.* **2002**, *51*, 1-186.
- (76) Kim, H.; Hahn, H. T.; Viculis, L. M.; Gilje, S.; Kaner, R. B. Electrical conductivity of graphite/polystyrene composites made from potassium intercalated graphite. *Carbon* **2007**, *45*, 1578-1582.
- (77) Viculis, L. M.; Mack, J. J.; Mayer, O. M.; Hahn, H. T.; Kaner, R. B. Intercalation and exfoliation routes to graphite nanoplatelets. *J. Mater. Chem.* **2005**, *15*, 974-978.
- (78) Nixon, D.; Parry, G. Formation and structure of the potassium graphites. *J. Phys. D: Appl. Phys.* **1968**, *1*, 291-298.
- (79) Rüdorff, W.; Schulze, E. Über Alkaligraphitverbindungen. *Z. Anorg. Allg. Chem.* **1954**, *277*, 156-171.

Chapter 3 Na-ion Storage in Non-Graphitic Carbons

3.1 Background

As the sixth most abundant element on earth, carbon is one of the most critical elements to human being. Carbon compounds account for over 95% of all known compounds.¹ Ranging from gaseous CO₂ to lots of organic molecules, carbon is everywhere in our life. In terms of pure carbon, it also has different types of allotropes including graphite, diamond, graphene, amorphous carbon, etc. This thesis will focus on amorphous carbon which has been used as anode for NIBs.

3.2 Non-graphitic carbon

Carbon can form different types of hybridization, including sp¹, sp² and sp³. Among these three hybridized carbon, sp² and sp³ are the most common ones. Graphite, which is composed of stack of pure sp² carbon layers, is soft and conductive. While, diamond, which is composed of pure sp³ carbon, is the hardest material and it is not conductive.¹ There are various types of carbon allotropes exist in between these two extreme cases. Amorphous carbons with mixed sp² and sp³ carbon are one type of carbon that lacks crystallinity and has been considered as a carbon allotrope. The term ‘amorphous carbon’ usually means that the carbon materials do not have long-range order, but short-range order exists. Often time, the term ‘amorphous carbon’ is interchangeably with ‘non-graphitic carbon’ in the literatures. However, these two terms are slightly different, where non-graphitic carbon indicates that there is certain degree of ordering along the

two-dimensional hexagonal lattice where some near parallel layers stacked but without any measurable order in the c -direction.^{2,3} Most of the carbon involved in this thesis all have a certain degree of ordering along the ab plane with stacking of graphene layers and thus we will call them non-graphitic carbons.

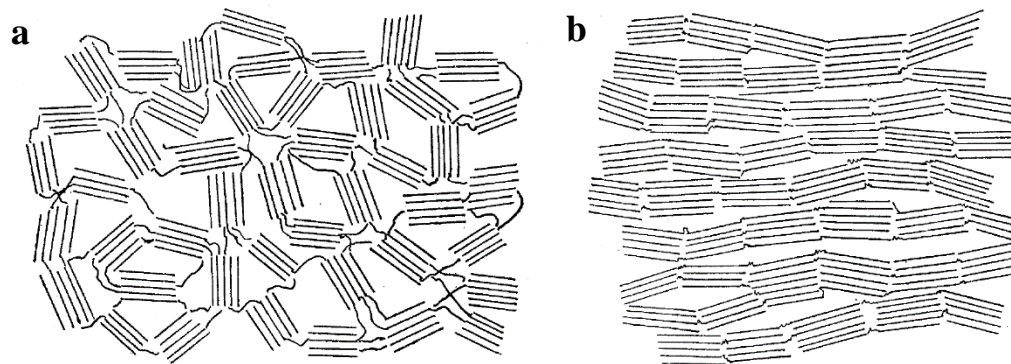


Figure 3.1 Franklin's schematic representation of the structure of (a) a non-graphitizing carbon, and (b) a graphitizing carbon.⁴

In 1951, Franklin proposed two models for two types of non-graphitic carbons, namely, non-graphitizable carbon and graphitizable carbon.⁴ The structure model of these two types of carbons is shown in (Figure 3.1). According to her models, there exist graphite crystallites in both two types of carbons, where such crystallites are cross-linked. For non-graphitizable carbon, even under high pyrolysis temperature (1700-3000°C), graphite-like structure cannot be formed and therefore it is also named “hard carbon”. However, for graphitizable carbon, the transformation into crystalline graphite occurs under high temperature pyrolysis and thus it is also called “soft carbon”. Franklin attributed the main reason that leads to this difference to the structure difference of these two types of carbons. As shown in Figure 3.1a, the graphite crystallites in the non-

graphitizable carbon is randomly oriented, and the formation of crystalline graphite must involve in the motion of the entire crystallites. The activation energy requires for such motion is too high, and thus the graphite cannot be formed. On the other hand, the graphite crystallites in graphitizable carbon is pre-oriented (Figure 3.1b) where the crystallites are more parallel to each other, and thus the transformation of such structure into graphite is much easier.

Even though Franklin's models provide valuable information to understand the structure of non-graphitic carbons, these models simplified the complex structure of non-graphitic carbons and did not specify the nature of the cross-linking. Later, the development of more advanced characterization techniques, especially, transmission electron microscopy (TEM), played an important role on further understanding the complex structure of non-graphitic carbons, where the curvature of non-graphitic carbon had been revealed.⁵⁻⁷ With the supports of TEM results, Harris *et al.* proposed a new fullerene-like model for non-graphitizable carbon where pentagons and heptagons are taken into account for the first time.⁶ Despite that this model may not represent the real structure of non-graphitizable carbon, the randomly dispersed pentagons and heptagons illustrated in this model explains the presence of curvatures in non-graphitizable carbon. Even though significant advances have been made toward a better understanding of the structure of non-graphitic carbon, more research is still needed to gain more in-depth understanding of its complex structure.

3.3 Characterization of non-graphitic carbon by neutron total scattering diffraction

This thesis focuses on the understanding of the structure-property correlations of Na-ion and K-ion storage in non-graphitic carbon. Therefore, it is of great importance to have an in-depth understanding of the structure of non-graphitic carbon. XRD has been one of the most common characterization techniques to characterize the structure of materials. XRD utilizes x-ray as the radiation source and it interacts with the sample that being tested, and x-ray diffraction occurs when the conditions satisfy the Bragg's law. However, to meet Bragg's law, the sample must have lattice periodicity or in another word, long-range order. Unfortunately, non-graphitic carbon does not have long-range order, where only small size nanodomains with short-range order exists. Therefore, non-graphitic carbon only shows two broad peaks in XRD, where the average d-spacing can be obtained from XRD. It is challenging to obtain some other structural information such as defect concentration and coherence length from conventional XRD. However, all these structural properties of non-graphitic carbon are crucial for the electrochemical properties of non-graphitic carbon. Therefore, other characterization techniques have to be applied to gather more structural information of non-graphitic carbon.

Neutron total scattering associated with pair distribution function (PDF) has been proved to be a reliable and effective characterization technique for studying the structural properties of non-graphitic carbon. In contrast to XRD, neutron total

scattering uses neutron as the radiation source. Instead of interacting with surrounding electrons, neutron interacts with the nuclei of the sample which renders neutron scattering some unique advantages over conventional x-ray scattering. First, unlike XRD, which is much more sensitive to heavy metals, neutron scattering is also sensitive to light elements such as H, Li and O. Second, neutron scattering can differentiate isotopes which could be helpful in some cases. More importantly, with strong neutron radiation source, neutron total scattering takes account of both Bragg diffraction from the average structure and elastic diffuse scattering from the local structure. Therefore, neutron total scattering cannot only reveal the long-range order structural information but also the short-range and mid-range order structural information. Associated with PDF, neutron total scattering gives a more complete structural information in real space.

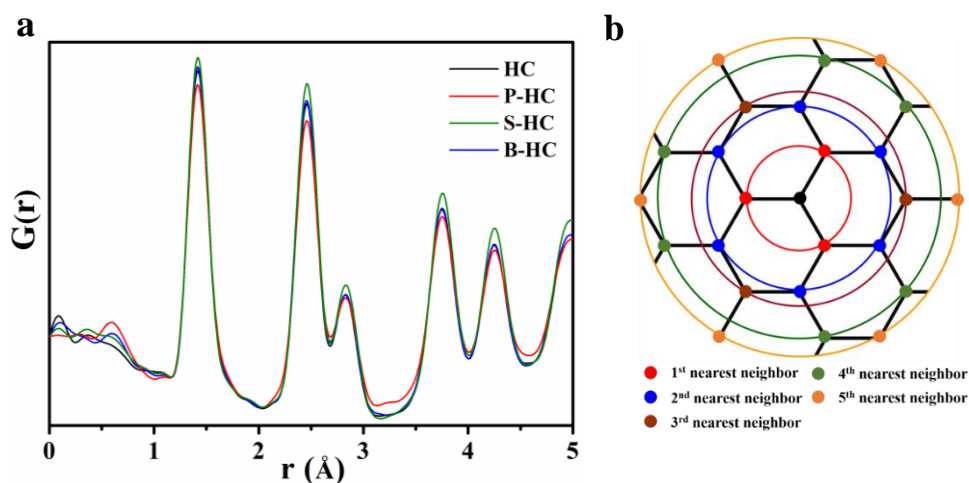


Figure 3.2 (a) Neutron total scattering associated PDF of various hard carbons. (b) Schematic local structure of graphene.

The neutron total scattering data is usually presented by PDF which is essentially a Fourier transformation of the scattering data. The scattering data of a sample is first collected and normalized to obtain the total scattering structure function ($S(Q)$), which contains both Bragg scattering and diffuse scattering.⁸ Then, the $G(r)$, which is the PDF, can be generated by Fourier transformation of the total scattering structure function $S(Q)$ according to equation (1):

$$G(r) = \frac{4}{\pi} \int_0^{\infty} Q[S(Q) - 1] \sin(Qr) dQ \quad (1)$$

In this equation, r is the distance and Q is the wave vector. The PDF plots of several non-graphitic carbons are shown in Figure 3.2a. The PDF plot is basically a radial distribution map, where r is the distance between a randomly selected central carbon atom and its surrounding neighbors. The first peak around 1.4 Å is corresponding to the distance between the central carbon atom and its first nearest carbon atoms that lies on the red circle as shown in Figure 3.2b. The second peak is corresponding to the distance between the central carbon atom and its second nearest carbon atoms. Therefore, the peak amplitude is proportional to the probability of finding carbon atoms at the specific distance and thus the peak amplitude can indicate the order degree of non-graphitic carbon. A higher peak amplitude suggests a higher order degree and a lower peak amplitude means a higher defect concentration. In addition, the peak amplitude attenuates with increasing distance where the loss of signals is indicative of the coherence length of non-graphitic carbons.

Neutron total scattering can provide valuable local structural information of non-graphitic carbons which is crucial for the study of structure-property correlations of Na-ion and K-ion storage in non-graphitic carbons. Unfortunately, the generation of neutrons and the operation of neutron total scattering is complicated and the access to neutron total scattering is limited to only a few places around the world.

3.4 Mechanism of Na-ion storage in hard carbon

In 2000, Dahn *et al.* first reported glucose derived hard carbon as anode for Na-ion storage, and by comparing with Li-ion storage in the same hard carbon, they proposed the first “House of cards” model about Na-ion storage in hard carbon (Figure 3.3a).⁹ Two distinct regions were identified in the galvanostatic charge-discharge potential profiles, namely, the high-potential sloping region and low-potential plateau region (Figure 3.3b). They attributed the high-potential sloping region to Na-ion insertion into the graphene layers of the turbostratic nanodomains and the low-potential plateau region to Na-ion insertion into the nanopores. They rationalized that the wide range of potential in this region is due to the inserted Na-ions change the potential for further Na-ion insertion and thus lead to a distribution of the insertion potentials. They also mentioned that the terminated hydrogen may also play a role for this wide potential range and for the hysteresis between Na-ion insertion and de-insertion.

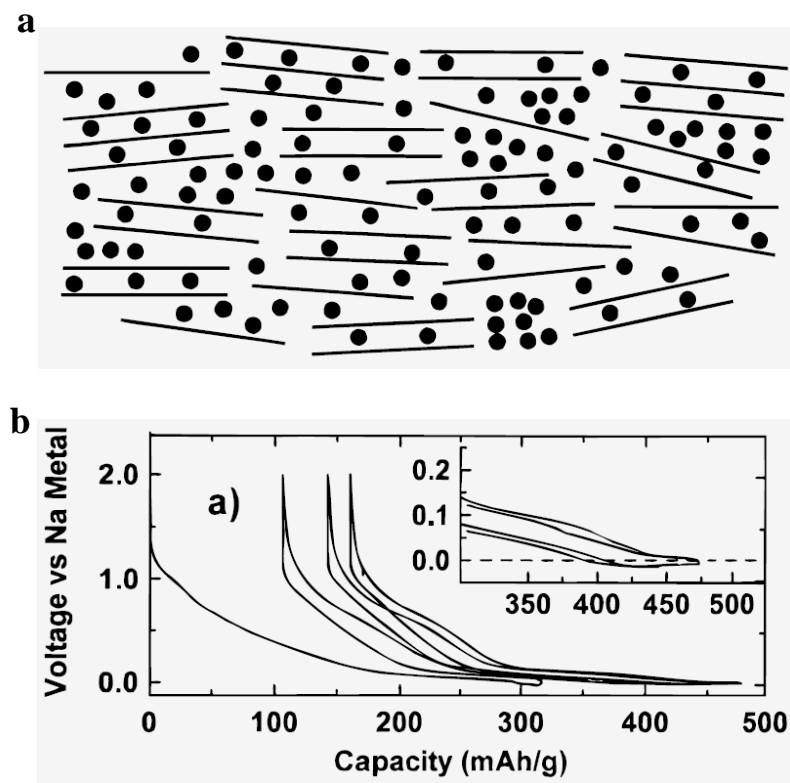


Figure 3.3 (a) “House of Cards” model for sodium filled hard carbon. (b) Sodium potential profiles for glucose pyrolyzed to 1000°C.⁹

Subsequently, to further explore the mechanism of Na-ion storage in hard carbon, Dahn *et al.* conducted in situ XRD and in situ small-angle x-ray scattering (SAXS) experiments for hard carbon anode. The results they obtained further support the “House of cards” model which also named as insertion-adsorption model. There were not too many follow-up studies on hard carbon anode for Na-ion storage until 2010s and this model has been widely accepted in the field in early 2010s. For instance, in 2011, via ex situ XRD, SAXS and Raman spectra, Komaba *et al.* further proved the insertion-adsorption model proposed by Dahn *et al.* with commercial hard carbon. Solid state

nuclear magnetic resonance (NMR), which is sensitive to the state of Na-ion in hard carbon matrix, was utilized to study Na-ion storage in hard carbon by Gotoh *et al.*¹⁰ Their results also agreed with the previous model. But they also pointed out that quasi-metallic clusters do not form in the pores of hard carbon upon sodiation.

With increasing attention had been paid to hard carbon anode for NIBs, different opinions about the mechanism of Na-ion storage in hard carbon came up in early 2010s. In 2012, Cao and Liu *et al.* reported hollow carbon nanowire as anode for NIBs where they proposed a different mechanism of Na-ion storage in hard carbon.¹¹ According to their mechanism, the high-voltage sloping region is due to charge transfer on the surface of small graphitic clusters and the low-voltage plateau region is attributed to Na-ion insertion in the interlayer of nanodomains. Via theoretical simulation, they proposed that Na-ion intercalation can take place when the interlayer distance of the nanodomains is higher than 0.37 nm. By pyrolyzing peat moss and banana peels at different temperatures, Mitlin *et al.* synthesized different hard carbons and studied their Na-ion storage performance.^{12, 13} They revealed that with increasing annealing temperature, the porosity of the obtained hard carbons decreased. However, their plateau capacity was improved with decreased porosity which does not agree with the insertion-adsorption model. In addition, their *ex situ* XRD results show dilation of the interlayer distance of hard carbon nanodomains which indicates that Na-ions are intercalated into the interlayer of the nanodomains at low-potential. By *ab initio* calculations, Yamada *et al.* also revealed that defects, especially mono-vacancy and di-vacancy in the graphene

sheets, have stronger binding energy with Na-ions and thus contribute to the high-potential sloping capacity.¹⁴ Their calculations also suggest that larger interlayer spacing of the graphene sheets can also increase the sodiation potential, and the plateau region is due to Na-ion intercalation into graphene sheets.

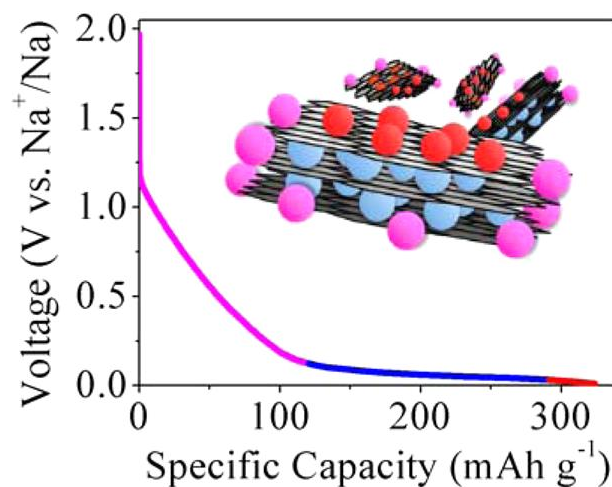


Figure 3.4 Potentiogram and schematic of proposed Na-ion three-part storage mechanism.¹⁵

In 2015, our group studied the mechanism of Na-ion storage in hard carbon anode by using sucrose derived hard carbons obtained at different pyrolysis temperature together with glassy carbon.¹⁵ The structure and electrochemical properties of these carbons were thoroughly characterized by neutron total scattering associated with PDF, XRD, Raman, electrochemical sodiation/desodiation and diffusivity tests. The capacity from the high-potential sloping region was found to be proportional with the defect concentration of the obtained hard carbons. Interlayer dilation was also revealed via ex situ XRD at low-potential upon sodiation which was rationalized by Na-ion intercalation in between the

graphene sheets of nanodomains. The steep increase of diffusivity at the very end of sodiation was attributed to Na-ion plating. Based on these results, we proposed a new model for Na-ion storage in hard carbon, where the sloping region is attributed to Na-ion absorption on defect sites, most of the plateau region is assigned to Na-ion intercalation into nanodomains and the very end of the plateau region is correlated with Na-ion plating in nanopores (Figure 3.4).

In 2016, Grey *et al.* conducted *operando* solid state NMR and PDF analysis on Na-ion storage in hard carbon.¹⁶ The NMR results suggest that Na-ions stored at high potentials have ionic interaction with the carbon structure which prefer the defect sites. Whereas at low potentials, Na-ions become more metallic and some clusters are formed at low potentials, and they attributed this phenomenon to Na-ion intercalation between graphene sheets with large interlayer spacing and Na-ion plating in pores. Their PDF results also indicate that the hard carbon structure has significant curvature which may play a critical role for Na-ion storage. Tarascon *et al.* studied the Na-ion storage in carbon nanofibers (CNFs) obtained from a wide temperature range (650-2800°C) and proposed a three steps sodiation process of CNFs.¹⁷ According to their mechanism, the higher sloping region is due to Na-ion adsorption on defect sites, the sloping region from 1 to 0.1 V is assigned to Na-ion adsorption to disordered isolated graphene sheets, and the plateau region below 0.1 V is attributed to mesopore filling.

Recently, we used heteroatom doping to fine tune the structure of sucrose derived hard carbons with consistently low surface area and then monitored their electrochemical performance.¹⁸ Our results further confirmed our previously proposed adsorption-intercalation model. At almost the same time, Cao and Liu et al. also reported a combined experimental and computational study of Na-ion storage in hard carbon. Their results also support the adsorption-intercalation model.¹⁹ In addition, their NMR results also exclude the possibility of Na-ion plating in the pores.

Overall, even though lots of efforts have been dedicated to understanding the mechanism of Na-ion storage in hard carbon, this is still a controversial topic in the field. However, researchers are reaching consensus that the high-potential sloping region is due to Na-ion adsorption on defect sites, whereas there are still different opinions in terms of the origin of the low-potential plateau region. The complex of hard carbon's structure which leads to the difficulties on its characterization is one of the main reasons that causes the discrepancies on the understanding of Na-ion storage in hard carbon. In addition, hard carbon obtained from different precursors and preparation conditions may have different porosity, defect concentration, type of defects, interlayer spacing, and some hard carbons even have closed pores which are hard to be detected. All these factors could lead to different Na-ion storage behavior of hard carbons and thus different understanding regarding the mechanism Na-ion storage hard carbon.

3.5 Mechanism of Na-ion storage in soft carbon

In 1993, Doeff et al. first reported soft carbon as anode for Na-ion storage.²⁰ In their work, the petroleum coke derived soft carbon demonstrated a reversible Na-ion storage capacity of ~90 mAh/g, corresponding to the formation of NaC₂₄. In sharp contrast to hard carbon, the research on Na-ion storage in soft carbon has received much less attention which may be due to its relatively low Na-ion storage capacity. In 2015, our group reported a soft carbon anode by pyrolyzing 3,4,9,10-perylene-tetracarboxylic acid-dianhydride (PTCDA) for Na-ion storage.²¹ The obtained soft carbon demonstrated a reversible capacity of 197 mAh/g at 20 mA/g. Even though its capacity is not as high as hard carbon, it exhibited excellent rate capability and cycling stability. In addition, the obtained soft carbon showed a different sodiation/desodiation profile with hard carbon, where the soft carbon does not have low-potential plateau region.

The difference of the sodiation/desodiation profiles between soft carbon and hard carbon should be due to their different Na-ion storage mechanism. Therefore, in 2017, our group conducted a comprehensive study on two typical soft carbons along with hard carbon to explore the mechanism of Na-ion storage in soft carbon.²² Via in situ TEM and ex situ XRD, it is revealed that the irreversible quasi-plateau at around 0.5 V versus Na⁺/Na is due to Na-ion intercalation into defective graphenic layers which traps Na-ions. Neutron total scattering associated with PDF demonstrates that the obtained soft carbon has high defect concentration. Density functional theory (DFT) analysis was conducted to study Na-ion binding with local carbon structural sites. The computational

results prove that Na-ion prefer to bind with defect sites and the simulated potential profiles match well with the experimental results. These results indicate that the high potential sloping profile of Na-ion storage in soft carbon is due to Na-ion binding with defects.

3.6 Heteroatom doping of non-graphitic carbon for Na-ion storage

Heteroatom doping has been considered as an effective strategy to tune the structural properties and enhance the electronic conductivity of carbon materials, and thus improve the Na-ion storage performance of the obtained carbon materials. Among different dopants, nitrogen, phosphorus and sulfur are the most studied elements.²³⁻³² Some other elements such as boron and fluorine have also been reported as dopant for carbon materials.^{18, 33} Most of these elements can form bond with carbon atom, where the heteroatom either exist as part of functional groups that attach to the surface of carbon or be incorporated into the carbon lattice. The surface functional groups can change the electrolyte-electrode interface interaction, induce more surface redox reaction and change the electronic conductivity of the obtained carbon materials. The dopant which is incorporated into the carbon lattice can be considered as defect if its binding energy with Na-ion is different with carbon atom. In addition, the incorporation of some heteroatom into carbon structure can also create more vacancies, lead to more curvatures and in some case expand the interlayer spacing. All these changes caused by heteroatom doping could enhance Na-ion storage performance of carbon materials. Therefore, heteroatom doping has received much attention as a facile method to improve

the Na-ion storage performance of non-graphitic carbon materials, especially hard carbon materials. Note that there are lots of reports about heteroatom doped graphene as anode for NIBs. However, most of these materials show large surface area and thus low first cycle coulombic efficiency and high average potential. In addition, the cost of graphene-based materials is much higher than that of non-graphitic carbons. Therefore, the heteroatom doped graphene will not be discussed in this section.

3.6.1 Nitrogen doping

Nitrogen, which is right next to carbon with one more extra valence electron, is one of the most studied dopants for non-graphitic carbons. Because nitrogen can bring extra electron to the carbon lattice, nitrogen doping has been proved to be able to improve the electronic conductivity of carbon materials. In addition, it has been reported that the nitrogen functional groups on the surface of carbon materials can introduce pseudo-capacitance and thus improve the capacity. Nitrogen doping of carbon materials can be achieved either by annealing the carbon precursors under N_2 or NH_3 gas or by annealing nitrogen containing precursors such as poly-acetonitrile (PAN), polyaniline (PANI), poly-pyrrole (PPY) or biomass materials.^{17, 24, 27, 34, 35} The percentage of dopants can be tuned by varying the annealing temperature, where higher annealing temperature normally lead to lower percentage of dopant. The incorporated nitrogen atom can exist as pyridinic-N, pyrrolic-N, graphitic-N and quaternary-N in the carbon lattice.

The reversible Na-ion storage capacity delivered by the reported N-doped carbons ranges from 172 mAh/g to 350 mAh/g, with good rate capability and cycling stability. The increased rate capability and cycling stability has been attributed to the improved electronic conductivity, Na-ion diffusivity, surface redox reactions and large surface area of the N-doped carbons. However, it is worth to note that the large surface area of the N-doped carbons also leads to low first cycle coulombic efficiency. In addition, most of the improved capacity is contributed from the high-potential sloping part which originates from the surface pseudo-capacitance. Such high-potential capacity does not contribute too much in the full cell.

3.6.2 Phosphorus and Sulfur doping

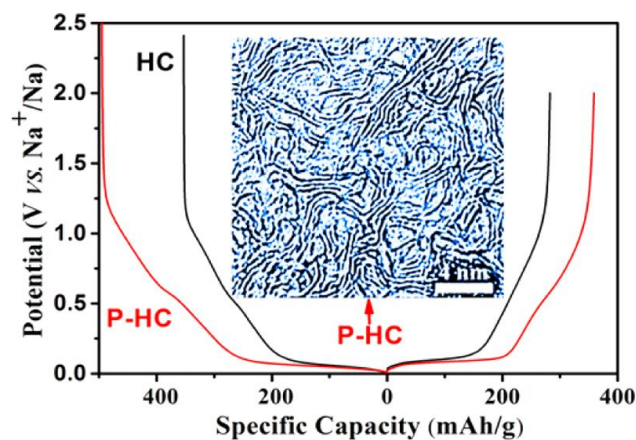


Figure 3.5 Sodiation-desodiation profiles of pristine and phosphorus-doped hard carbons at current density of 20 mA/g. The inset is the TEM image of the phosphorus-doped hard carbon.³²

In addition to N-doping, P- and S-doping have also received much attention. The synthesis of P-doped carbon rely more on a second phosphorus-containing precursor such as phosphoric acid to introduce phosphorus to the carbon structure. In 2014, Huang et al. reported phosphoric acid treated hard carbon as anode for NIBs, which delivered a high capacity of 315 mAh/g at a current of 50 mA/g.²⁸ However, due to its large surface area (1272 m²/g), it shows a very low first cycle coulombic efficiency of 27%. Later, our group reported the synthesis of P-doped hard carbon by mixing the carbon precursor with phosphoric acid and graphene oxide (GO) solution.³² The GO served as a dehydration agent which effectively limits the surface area of the obtained hard carbon to 7 m²/g and the obtained P-doped hard carbon contains lots of curvatures (Figure 3.5). The low surface area P-doped hard carbon shows a high reversible Na-ion storage capacity of 359 mAh/g with high first cycle coulombic efficiency of 73%, where the capacity is much higher than the non-doped hard carbon (283 mAh/g, Figure 3.5). In both these two reports, a larger interlayer d-spacing caused by the incorporation of lager phosphorus or PO_x has been considered as one of the main reasons that lead to the improved reversible capacity. P-doping induced higher defect concentration of P-doped hard carbon has also been identified as one reason for the improved capacity of the latter one.

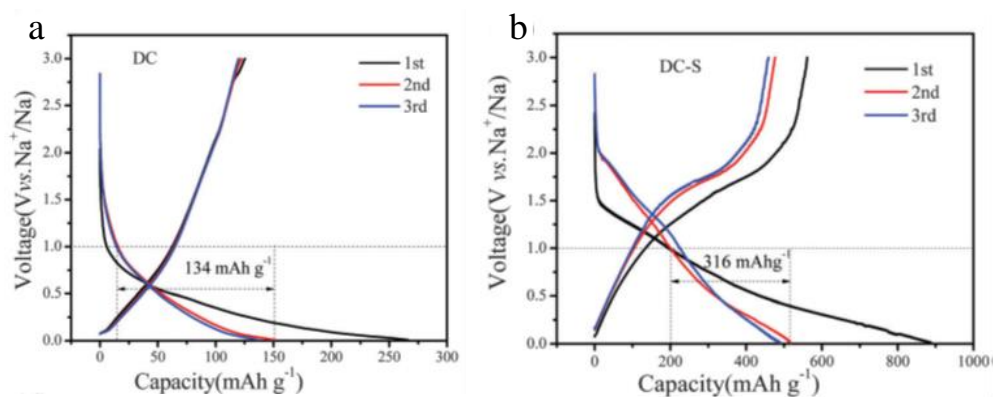


Figure 3.6 The charge-discharge profiles of disordered carbon before (a) and after sulfur-doping (b) at a current density of 0.02 A g^{-1} .³¹

Similar with P-doping, S-doping has also been reported to be able to improve the interlayer d-spacing of the doped carbons and thus enhance the reversible capacity. In 2015, Huang et al. reported a S-doped carbon as anode for NIBs by the pyrolysis of sulfur-containing precursor poly(3,4-ethylenedioxythiophene) (PEDOT). The obtained S-doped carbon has a high sulfur content of 15.17 wt%.²⁹ It demonstrated a high reversible capacity of 482 mAh/g at a current density of 0.1 A/g with high first cycle coulombic efficiency (73.6%). By pyrolysis of a mixture of carbon precursor (1,4,5,8-naphthalenetetracarboxylic dianhydride, NTCDA) with elemental sulfur, Jiang et al. synthesized S-doped carbon with even higher sulfur content of 26.9 wt%.³¹ With such high sulfur content, the reversible capacity improved from 126 mAh/g of pristine carbon to 516 mAh/g of the S-doped carbon at 0.02 A/g (Figure 3.6). It is worth to note that both phosphorus and sulfur can form alloy with Na-ion at relative high potential. Even both these two reports named the obtained product as S-doped carbon, with such a high sulfur content, a pure elemental sulfur phase may exist, especially in the latter

case where sulfur redox peaks have been identified. In addition, such S-doped carbon also shows high average potential even the low-potential capacity also increased compare with non-doped carbon (Figure 3.6). However, the its low-potential capacity is on par with other reported non-doped hard carbons. Therefore, this S-doped carbon with high average potential would not show high energy density in the full cell. In contrast to these two reports, we synthesized S-doped hard carbon by adding concentrated sulfuric acid to the aqueous carbon precursor. The obtained S-doped carbon had a low sulfur content of 0.1 wt%.¹⁸ However, with such low sulfur content, it still improved the reversible capacity of hard carbon from 283 mAh/g to 328 mAh/g at a current density of 20 mA/g with low average potential. The increased capacity was attributed to the expanded interlayer d-spacing of the obtained hard carbon.

3.6.3 Boron doping and fluorine doping

Compare with N-, P- and S-doping, B-doping and F-doping have rarely been reported. Boron can form in-plane sp^2 bond with carbon atom which can also serve as a dopant for carbon materials. Computational studies have demonstrated that B-doping can improve the capacity of graphene for Na-ion storage with increased electrons and Na-ion mobility.³⁶ However, our experimental results showed that B-doped hard carbon delivers a much lower reversible Na-ion storage capacity (147 mAh/g) than non-doped hard carbon (283 mAh/g) even though it has a large first sodiation capacity.¹⁸ The obtained B-doped hard carbon has a low surface area of 8.0 m^2/g , where the formation of solid electrolyte interface (SEI) cannot be the only reason that lead to such low first

cycle coulombic efficiency. Combining computational studies with high voltage desodiation test, we hypothesized that the low reversibility of B-doped hard carbon is due to the large binding energy between boron defect sites in the carbon lattice with the inserted Na-ions which leads to the difficulty of desodiation. Another reported B-doped carbon synthesized by annealing the mixture of BBr_3 and C_6H_6 shows a reversible capacity of 278 mAh/g at 100 mA/g.³⁷ However, considering its high average operation potential, its Na-ion storage performance is not superior than other non-doped hard carbons.

So far, there has been only one report about F-doped carbon as anode for NIBs. The F-doped carbon was obtained by the pyrolysis of fluorine-containing lotus petioles.³³ The F-doped carbon exhibited a larger interlayer d-spacing compare with non-doped carbon and thus delivered a reversible capacity of 230 mAh/g at current density of 50 mA/g. Again, comparing with other non-doped carbon anode for Na-ion storage, the capacity of the F-doped carbon did not demonstrate the advantages of F-doping.

Overall, extensive efforts have been dedicated to the development of heteroatom doped carbon materials to enhance their Na-ion storage performance. However, most of the reported heteroatom doped carbons were synthesized with different precursors, methods and conditions which lead to the difficulty of comparing different heteroatom doped carbons among different studies. This would limit the in-depth understanding of the effects of heteroatom doping on the performance of Na-ion storage. Our study that

investigated the Na-ion storage performance of B-, P-, S-doped and non-doped hard carbons with consistently low surface area which were obtained with same preparation method serves as the first example of systematical study of heteroatom doped carbons.³³ We were able to reveal the effects of heteroatom doping on the structural properties and electrochemical properties of the obtained doped hard carbons by this systematical study, and thus build up the correlation between the structure of hard carbon and its Na-ion storage performance. Future work that focuses on the fundamental understanding of how heteroatom doping improves the Na-ion storage performance of carbon materials could be beneficial to the field. The study of other dopants other than the above mentioned dopants and co-doping also worth to be explored.

3.7 References

- (1) Falcao, E. H.; Wudl, F. Carbon allotropes: beyond graphite and diamond. *J. Chem. Technol. Biotechnol.* **2007**, *82*, 524-531.
- (2) Faber, K.; Badaczewski, F.; Ruland, W.; Smarsly, B. M. Investigation of the Microstructure of Disordered, Non-graphitic Carbons by an Advanced Analysis Method for Wide-Angle X-ray Scattering. *Z. Anorg. Allg. Chem.* **2014**, *640*, 3107-3117.
- (3) Ruland, W.; Smarsly, B. X-ray scattering of non-graphitic carbon: an improved method of evaluation. *J. Appl. Crystallogr.* **2002**, *35*, 624-633.
- (4) Franklin, R. E. Crystallite growth in graphitizing and non-graphitizing carbons. *Proc. R. Soc. London, Ser.* **1951**, *209*, 196-218.
- (5) Ban, L.; Crawford, D.; Marsh, H. Lattice-resolution electron microscopy in structural studies of non-graphitizing carbons from polyvinylidene chloride (PVDC). *J. Appl. Crystallogr.* **1975**, *8*, 415-420.
- (6) Harris, P. J.; Tsang, S. C. High-resolution electron microscopy studies of non-graphitizing carbons. *Philos. Mag. A* **1997**, *76*, 667-677.
- (7) Harris, P. J.; Liu, Z.; Suenaga, K. Imaging the atomic structure of activated carbon. *J. Phys.: Condens. Matter* **2008**, *20*, 362201.

- (8) Egami, T.; Billinge, S. J. Underneath the Bragg Peaks: Structural Analysis of Complex Materials. *Pergamon Materials Series*. **2012**, *16*.
- (9) Stevens, D.; Dahn, J. High Capacity Anode Materials for Rechargeable Sodium-Ion Batteries. *J. Electrochem. Soc.* **2000**, *147*, 1271-1273.
- (10) Gotoh, K.; Ishikawa, T.; Shimadzu, S.; Yabuuchi, N.; Komaba, S.; Takeda, K.; Goto, A.; Deguchi, K.; Ohki, S.; Hashi, K. NMR study for electrochemically inserted Na in hard carbon electrode of sodium ion battery. *J. Power Sources* **2013**, *225*, 137-140.
- (11) Cao, Y.; Xiao, L.; Sushko, M. L.; Wang, W.; Schwenzler, B.; Xiao, J.; Nie, Z.; Saraf, L. V.; Yang, Z.; Liu, J. Sodium ion insertion in hollow carbon nanowires for battery applications. *Nano Lett.* **2012**, *12*, 3783-3787.
- (12) Ding, J.; Wang, H.; Li, Z.; Kohandehghan, A.; Cui, K.; Xu, Z.; Zahiri, B.; Tan, X.; Lotfabad, E. M.; Olsen, B. C. Carbon nanosheet frameworks derived from peat moss as high performance sodium ion battery anodes. *ACS Nano* **2013**, *7*, 11004-11015.
- (13) Lotfabad, E. M.; Ding, J.; Cui, K.; Kohandehghan, A.; Kalisvaart, W. P.; Hazelton, M.; Mitlin, D. High-density sodium and lithium ion battery anodes from banana peels. *ACS Nano* **2014**, *8*, 7115-7129.
- (14) Tsai, P.-C.; Chung, S.-C.; Lin, S.-K.; Yamada, A. Ab initio study of sodium intercalation into disordered carbon. *J. Mater. Chem. A* **2015**, *3*, 9763-9768.
- (15) Bommier, C.; Surta, T. W.; Dolgos, M.; Ji, X. New mechanistic insights on Na-ion storage in nongraphitizable carbon. *Nano Lett.* **2015**, *15*, 5888-5892.
- (16) Stratford, J. M.; Allan, P. K.; Pecher, O.; Chater, P. A.; Grey, C. P. Mechanistic insights into sodium storage in hard carbon anodes using local structure probes. *Chem. Commun.* **2016**, *52*, 12430-12433.
- (17) Zhang, B.; Ghimbeu, C. M.; Laberty, C.; Vix-Guterl, C.; Tarascon, J. M. Correlation between microstructure and Na storage behavior in hard carbon. *Adv. Energy Mater.* **2016**, *6*, 1501588.
- (18) Li, Z.; Bommier, C.; Chong, Z. S.; Jian, Z.; Surta, T. W.; Wang, X.; Xing, Z.; Neuefeind, J. C.; Stickle, W. F.; Dolgos, M. Mechanism of Na-Ion Storage in Hard Carbon Anodes Revealed by Heteroatom Doping. *Adv. Energy Mater.* **2017**, *7*, 1602894.
- (19) Qiu, S.; Xiao, L.; Sushko, M. L.; Han, K. S.; Shao, Y.; Yan, M.; Liang, X.; Mai, L.; Feng, J.; Cao, Y. Manipulating Adsorption–Insertion Mechanisms in Nanostructured Carbon Materials for High-Efficiency Sodium Ion Storage. *Adv. Energy Mater.* **2017**, *7*, 1700403.
- (20) Doeff, M. M.; Ma, Y.; Visco, S. J.; De Jonghe, L. C. Electrochemical insertion of sodium into carbon. *J. Electrochem. Soc.* **1993**, *140*, L169-L170.
- (21) Luo, W.; Jian, Z.; Xing, Z.; Wang, W.; Bommier, C.; Lerner, M. M.; Ji, X. Electrochemically expandable soft carbon as anodes for Na-ion batteries. *ACS Cent. Sci.* **2015**, *1*, 516-522.

- (22) Jian, Z.; Bommier, C.; Luo, L.; Li, Z.; Wang, W.; Wang, C.; Greaney, P. A.; Ji, X. Insights on the mechanism of Na-ion storage in soft carbon anode. *Chem. Mater.* **2017**, *29*, 2314-2320.
- (23) Fu, L.; Tang, K.; Song, K.; van Aken, P. A.; Yu, Y.; Maier, J. Nitrogen doped porous carbon fibres as anode materials for sodium ion batteries with excellent rate performance. *Nanoscale* **2014**, *6*, 1384-1389.
- (24) Wang, Z.; Qie, L.; Yuan, L.; Zhang, W.; Hu, X.; Huang, Y. Functionalized N-doped interconnected carbon nanofibers as an anode material for sodium-ion storage with excellent performance. *Carbon* **2013**, *55*, 328-334.
- (25) Yang, F.; Zhang, Z.; Du, K.; Zhao, X.; Chen, W.; Lai, Y.; Li, J. Dopamine derived nitrogen-doped carbon sheets as anode materials for high-performance sodium ion batteries. *Carbon* **2015**, *91*, 88-95.
- (26) Zhu, J.; Chen, C.; Lu, Y.; Ge, Y.; Jiang, H.; Fu, K.; Zhang, X. Nitrogen-doped carbon nanofibers derived from polyacrylonitrile for use as anode material in sodium-ion batteries. *Carbon* **2015**, *94*, 189-195.
- (27) Yang, T.; Qian, T.; Wang, M.; Shen, X.; Xu, N.; Sun, Z.; Yan, C. A sustainable route from biomass byproduct okara to high content nitrogen-doped carbon sheets for efficient sodium ion batteries. *Adv. Mater.* **2016**, *28*, 539-545.
- (28) Hong, K.-l.; Qie, L.; Zeng, R.; Yi, Z.-q.; Zhang, W.; Wang, D.; Yin, W.; Wu, C.; Fan, Q.-j.; Zhang, W.-x. Biomass derived hard carbon used as a high performance anode material for sodium ion batteries. *J. Mater. Chem. A* **2014**, *2*, 12733-12738.
- (29) Qie, L.; Chen, W.; Xiong, X.; Hu, C.; Zou, F.; Hu, P.; Huang, Y. Sulfur-Doped Carbon with Enlarged Interlayer Distance as a High-Performance Anode Material for Sodium-Ion Batteries. *Adv. Sci.* **2015**, *2*, 1500195.
- (30) Hou, H.; Shao, L.; Zhang, Y.; Zou, G.; Chen, J.; Ji, X. Large-Area Carbon Nanosheets Doped with Phosphorus: A High-Performance Anode Material for Sodium-Ion Batteries. *Adv. Sci.* **2016**, *4*, 1600243.
- (31) Li, W.; Zhou, M.; Li, H.; Wang, K.; Cheng, S.; Jiang, K. A high performance sulfur-doped disordered carbon anode for sodium ion batteries. *Energy Environ. Sci.* **2015**, *8*, 2916-2921.
- (32) Li, Z.; Ma, L.; Surta, T. W.; Bommier, C.; Jian, Z.; Xing, Z.; Stickle, W. F.; Dolgos, M.; Amine, K.; Lu, J. High Capacity of Hard Carbon Anode in Na-Ion Batteries Unlocked by POx Doping. *ACS Energy Lett.* **2016**, *1*, 395-401.
- (33) Wang, P.; Qiao, B.; Du, Y.; Li, Y.; Zhou, X.; Dai, Z.; Bao, J. Fluorine-Doped Carbon Particles Derived from Lotus Petioles as High-Performance Anode Materials for Sodium-Ion Batteries. *J. Phys. Chem. C* **2015**, *119*, 21336-21344.
- (34) Wang, H. G.; Wu, Z.; Meng, F. L.; Ma, D. L.; Huang, X. L.; Wang, L. M.; Zhang, X. B. Nitrogen-Doped Porous Carbon Nanosheets as Low-Cost, High-Performance Anode Material for Sodium-Ion Batteries. *ChemSusChem* **2013**, *6*, 56-60.

- (35) Xiao, L.; Cao, Y.; Henderson, W. A.; Sushko, M. L.; Shao, Y.; Xiao, J.; Wang, W.; Engelhard, M. H.; Nie, Z.; Liu, J. Hard carbon nanoparticles as high-capacity, high-stability anodic materials for Na-ion batteries. *Nano Energy* **2016**, *19*, 279-288.
- (36) Ling, C.; Mizuno, F. Boron-doped graphene as a promising anode for Na-ion batteries. *Phys. Chem. Chem. Phys.* **2014**, *16*, 10419-10424.
- (37) Stadie, N. P.; Billeter, E.; Piveteau, L.; Kravchyk, K. V.; Döbeli, M.; Kovalenko, M. V. Direct synthesis of bulk boron-doped graphitic carbon. *Chem. Mater.* **2017**, *29*, 3211-3218.

Chapter 4 High Capacity of Hard Carbon Anode in Na-Ion Batteries Unlocked by PO_x Doping

4.1 Abstract

Capacity of hard carbon anodes in Na-ion batteries rarely reaches values beyond 300 mAh/g. Herein, we report that doping PO_x into local structures of hard carbon increases its reversible capacity from 283 to 359 mAh/g. We confirm that the doped PO_x is redox inactive by x-ray adsorption near edge structure measurements, thus not contributing to the higher capacity. We observe two significant changes of hard carbon's local structures caused by doping. Firstly, the (002) d-spacing inside the turbostratic nanodomains is increased, revealed by both laboratory and synchrotron x-ray diffraction. Secondly, doping turns turbostratic nanodomains more defective along ab planes, indicated by neutron total scattering and the associated pair distribution function (PDF) studies. The local structural changes of hard carbon are correlated to the higher capacity, where both the plateau and slope regions in the potential profiles are enhanced. Our study demonstrates that Na-ion storage in hard carbon heavily depends on carbon local structures, where such structures, despite being disordered, can be tuned toward unusually high capacities.

4.2 Introduction

The scarcity of lithium calls for alternative battery technologies based on Earth-abundant elements. Such batteries are demanded for stationary applications to enable intermittent renewable energy sources, smart grids, and microgrids.¹⁻⁶ Na-ion batteries

(NIBs) are intrinsically competitive due to the abundance and globally ubiquitous distribution of sodium as well as their similar rocking-chair operation mechanism as lithium-ion batteries (LIBs).^{7, 8} Rapid progress has been made on NIB cathodes,⁹⁻¹³ including layered metal oxides¹⁴⁻¹⁹ and polyanionic compounds.²⁰⁻²³ On the anode side, materials, including metal alloys,²⁴⁻²⁶ metal oxides,^{27, 28} phosphorus-based anodes^{29, 30} and sodium metal³¹ have been investigated. Futuristic commercialization of NIBs may rely on high-performing carbon anodes. The remarkable successes of LIBs would not be achieved without adopting graphite anodes that exhibit a capacity of ca. 360 mAh/g by forming LiC₆, the stage-I graphite intercalation compound (GIC). Unfortunately, sodium-GICs cannot be formed due to the unfavorable thermodynamics between graphite and Na unless electrolyte solvents are co-intercalated³² or graphite goes through sequential treatments of oxidation and reduction to generate a more defective turbostratic structure.^{33, 34} Fortunately, nongraphitic carbons as anodes can provide meaningful capacities for NIBs.³⁵⁻³⁷ Among them, hard carbon, also known as nongraphitizable carbon, has become the leading candidate since Stevens and Dahn first reported a reversible capacity of ~300 mAh/g on pyrolyzed glucose.³⁸⁻⁴¹

During the last 15 years, intense effort has been made to pursue higher capacities of hard carbon NIB anodes. One strategy is to identify unique precursors in combination with optimal reaction conditions; a wide spectrum of biomasses have been investigated for pyrolysis, such as sucrose,⁴² cellulose,⁴³ lignin,⁴⁴ banana peels,^{45, 46} and peat moss.⁴⁷ As the highest capacity reported to date, Mitlin *et al.* realized a reversible capacity of

ca. 350 mAh/g from pyrolyzed banana peels annealed at 1400 °C.⁴⁶ Another strategy is about tuning carbon structures with heteroatoms, where various dopants, including nitrogen, fluorine, phosphorus and their co-doping have been studied.⁴⁸⁻⁵⁹ These doped carbons exhibit unique and interesting properties; however, they often lose the key electrochemical characteristics of hard carbon—low operation potentials and high first cycle coulombic efficiency (CE@1st). Most recently, aromatics-derived carbons doped by sulfur species were demonstrated with large capacities over 400 mAh/g, where the high capacities are attributed to the increased d-spacing of the turbostratic domains as well as the redox reactivity of the doped sulfur species.^{60, 61} It is worth noting that the average desodiation potential of such carbons is rather high. To date, it remains challenging to significantly increase the capacity while maintaining the key desirable characteristics of hard carbon.

A primary knowledge gap is the lack of basic empirical understanding on the structure-capacity relationship for hard carbon anodes. To reveal such a relationship, one straightforward strategy is to vary the local structures and measure the consequent capacities, thus identifying the trend. For practical applications, ideally the designed carbons should exhibit a consistently low specific surface area as a controlling factor so that the trend will not be covered up by the extensive formation of solid electrolyte interphase (SEI). Furthermore, a low surface area will promote the key characteristics of hard carbon.

Herein, we report that doping of phosphorus oxide (PO_x) in hard carbon renders the structure of hard carbon more favorable in Na-ion storage, thus increasing its reversible desodiation capacity from 283 mAh/g to 359 mAh/g with a low operation potential. Interestingly, the capacities from both the plateau region (from 0.01 to 0.2 V) and the slope region (from 0.2 to 2.0 V) are increased. We determine that the doped PO_x is redox inactive, thus not contributing to the higher capacity, by monitoring the oxidation state of phosphorus over cycling. It is the doping-caused changes of carbon local structures that lead to the higher capacity.^{59, 60} In terms of the structural changes, the (002) d-spacing of turbostratic nanodomains (TNs) is enlarged, and the ab planes of TNs gets more defective, revealed by neutron total scattering.

4.3 Experimental Section

Synthesis of P-HC: Aqueous suspension of GO was prepared via modified Hummer's method for the preparation for both HC and P-HC. Sucrose, H_3PO_4 and GO with the mass ratio of 80:4:1 were mixed in an aqueous solution before sonication. The obtained solution/suspension was dried at 80 °C for 48 h, dehydrated at 180 °C for 24 h and then pyrolyzed at 1100 °C for 5 h under Ar flow. The HC was prepared with the same conditions but without the addition of H_3PO_4 .

Materials Characterization: Brunauer-Emmett-Teller (BET) surface area was obtained by N_2 sorption measurements on a Micromeritics TriStar II 3020 analyzer. The morphology of HC and P-HC were obtained by an FEI NOVA 230 high resolution

scanning electron microscopy (SEM). Energy-dispersive X-ray (EDX) mapping were obtained on a FEI Titan 80-300 (S) transmission electron microscopy (TEM) with an EDX attachment. To reveal the doping dispersion inside hard carbon particles and eliminate the impact from surface species, a specimen (100 nm thick) was carved out of a large carbon particle by focused-ion beam (FIB) before EDX mapping. TEM images were recorded by a FEI Titan 80-200 TEM. X-ray photoelectron spectroscopy (XPS) measurements were performed in a Physical Electronics Quantera Scanning ESCA Microprobe with a focused monochromatic Al K α X-ray (1486.6 eV) source for excitation. The x-ray beam used was a 25 W, 100 μ m X-ray beam spot at the sample. Phosphorus K-edge XANES data were collected at the Advanced Photon Source (APS) on the beamline 9-BM-B with electron energy of 7 GeV and average current of 100 mA. The radiation was monochromatized by a Si (111) double-crystal monochromator. Harmonic rejection was accomplished with a Rh-coated mirror. The samples were measured in a He-purged sample chamber and data were collected in fluorescence mode using a four-element Vortex Si-Drift detector. The phosphorus pentoxide (P₂O₅) was used for energy calibration by setting the first derivative to 2149 eV. The XRD patterns of obtained materials were collected on a Rigaku Ultima IV Diffractometer with Cu K α (λ = 1.5406 Å) radiation and the patterns are fitted with the PDXL software. The high-energy synchrotron XRD was carried out at the 11-ID-C beamline of the Advanced Photon Source, Argonne National Laboratory. The wavelength was 0.11798Å. The XRD patterns were collected in the transmission mode using a Perkin Elmer large area detector. The collected two-dimensional patterns were then integrated into conventional

one-dimensional patterns (intensity versus 2θ) for final data analysis using the Fit2d software. Raman spectra were obtained from WITec confocal Raman spectrometer with a 514 nm laser source and the fitting was done by Origin 8.5. Neutron total scattering data were collected at the Nanoscale Ordered Materials Diffractometer (NOMAD), Spallation Neutron Source, at Oak Ridge National Laboratory. Samples were loaded into quartz capillaries for analysis.

Electrochemical Measurements: Coin cells (CR2032) are used for all the electrochemical measurements. The electrodes consisted of hard carbon, polyvinylidene fluoride (PVdF) and carbon black with a mass ratio of 80:10:10. For preparation of electrodes, electrode components are grounded in N-Methyl-2-pyrrolidone (NMP), and the obtained slurry is coated onto Al foil by doctor blade and dried at 100 °C for 12 h under vacuum. The active mass loading for all electrodes are between 1.5 to 2 mg/cm². Sodium metal is used as the counter/reference electrode and 1.0 mol/L NaPF₆ solution in ethylene carbonate (EC)/diethyl carbonate (DEC) (1:1 in volume) is used as the electrolyte. Galvanostatic sodiation/desodiation tests are performed in the potential range of 0.01-2 V vs Na⁺/Na on Arbin BT2000 system at room temperature. CV curves are collected on a VMP-3 multichannel workstation at a scan rate of 0.1 mV/S at room temperature.

4.4 Results and Discussion

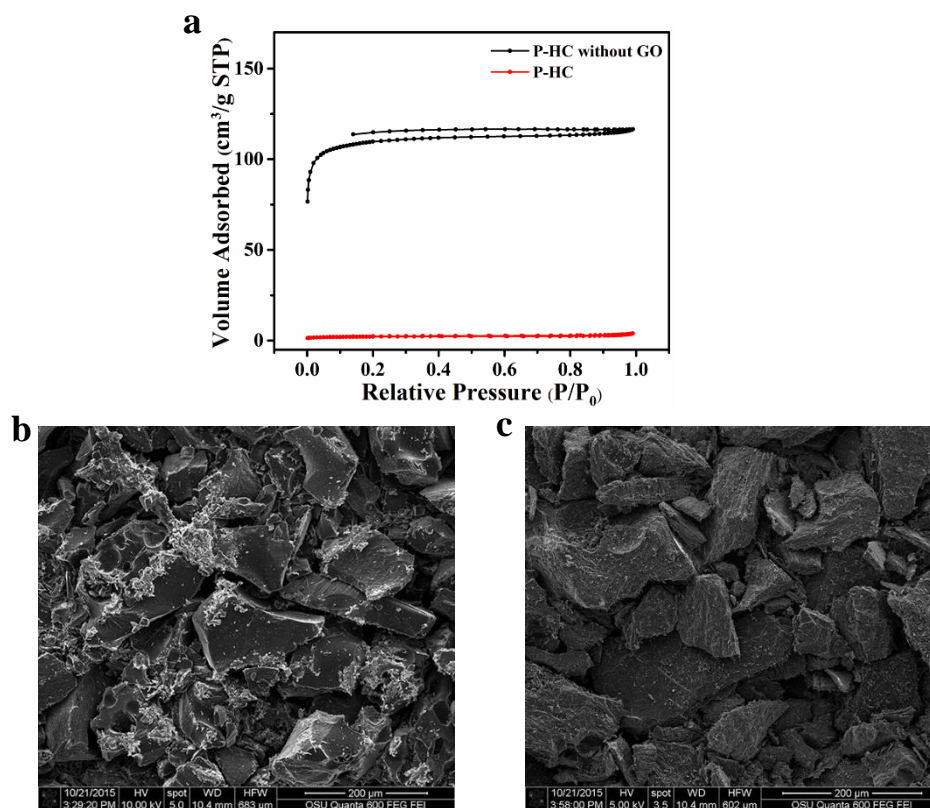


Figure 4.1 (a) N₂ sorption isotherms of doped carbons with and without the addition of GO. SEM images of (b) HC and (c) P-HC.

To dope phosphorus species into carbon, H₃PO₄ is the natural choice of precursor as a molecular level of mixing between H₃PO₄ and sucrose can be achieved in an aqueous solution, thus resulting in uniform doping after carbonization. However, annealing the mixture of H₃PO₄ and carbon precursors typically renders carbon activation, where the specific surface area of the “doped” carbons is greatly increased, thus qualifying for capacitive charge storage.^{62, 63} Our prior research showed that a higher surface area of hard carbon typically results in a lower capacity and low CE@1st due to more SEI

formation.⁶⁴ Therefore, the challenge is to prevent the activation effect on the doped carbon when using H_3PO_4 as the precursor.

Recently, we discovered that the surface area of pyrolyzed sucrose can be made extremely low, *e.g.*, $5 \text{ m}^2/\text{g}$, when sucrose is dehydrated and pyrolyzed in the presence of well mixed graphene oxide (GO).⁶⁵ Such a low surface area of pyrolyzed sugar was only possible when very high annealing temperatures were used, *e.g.*, $>1600 \text{ }^\circ\text{C}$, whereas we only use $1100 \text{ }^\circ\text{C}$. The impact of GO addition is significant, where the difference is $7 \text{ m}^2/\text{g}$ vs $353 \text{ m}^2/\text{g}$, with and without GO addition, respectively, for the pyrolyzed mixture of sucrose and H_3PO_4 (Figure 4.1a). As shown in scanning electron microscopy (SEM) images (Figure 4.1b and c), both undoped hard carbon (named as HC, where GO is also added) and P-doped hard carbon (P-HC) exhibit very large particle sizes. We determine the doping level of phosphorus to be 3 wt% in P-HC by inductively coupled plasma optical emission spectrometry (ICP-OES). In order to examine the dopant's dispersion degree, we collect elemental mappings by energy dispersive x-ray (EDX) spectroscopy associated with transmission electron microscopy (TEM). Indeed, the EDX P-signals are nearly atomically dispersed in the specimen, indicating a molecular-level of doping (Figure 4.2a and b). In terms of the size of the doped P-containing species, the molecular level of mixing between solvated H_3PO_4 and sucrose during the preparation, and the near atomic dispersion of P-signals in the resulting doped carbon collectively suggest that there is a lack of any degree of agglomeration of P-species. Note that the TEM/EDX specimen was prepared by focus

ion beam (FIB), where a thin slice (~100 nm thick) was lifted from a large particle, so as to reveal the true doping dispersion in the bulk phase of carbon particles. TEM images of both HC and P-HC (Figure 4.2c, d) do not show apparent difference, and it is difficult to determine their interlayer d-spacings simply based on these images. Thus, we use other characterization methods as discussed later. Moreover, we attempt to reveal the oxidation states of phosphorus in P-HC, where we employ x-ray photoelectron spectroscopy (XPS) first. The phosphorus 2p signal is deconvoluted into three components at 134.5, 133.1 and 131.0 eV, ascribed to P(V), P(II), and P-C bonds, respectively (Figure 4.3a).^{66, 67} The signal peak intensity corresponding to P-C bonds is relatively low, which suggests that most of the doped phosphorus species contain oxygen atoms. To further confirm the results, we collect x-ray absorption near edge structure (XANES) of P-HC (Figure 4.3b). Based on the edge positions of the standards—NaH₂PO₂ for P(I) and P₂O₅ for P(V),⁶⁸ the two peaks at 2146.4 eV and 2149.0 eV are assigned to P(III) and P(IV)/P(V), respectively, where there is even no signal from phosphorus of zero oxidation state. Therefore, according to the XPS and XANES results, it is evident that most doped phosphorus species occur as PO_x instead of elemental phosphorus.

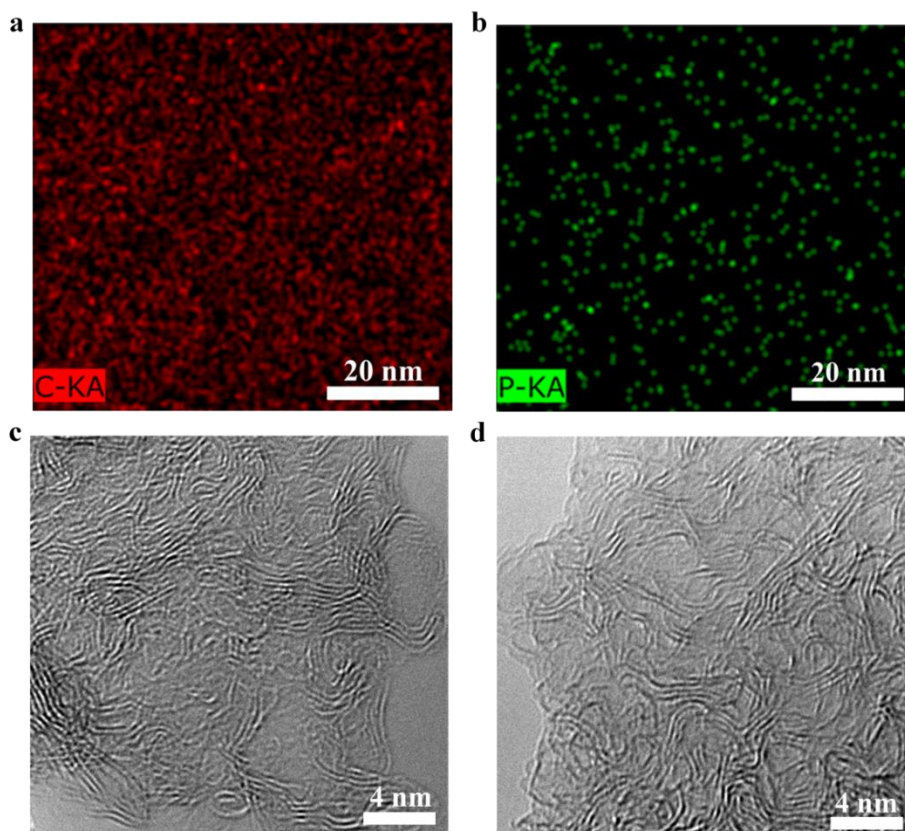


Figure 4.2 TEM EDX elemental mappings of P-HC and TEM images of HC and P-HC. (a,b) Elemental mappings for (a) carbon (b) phosphorus in P-HC. TEM images of (c) HC and (d) P-HC.

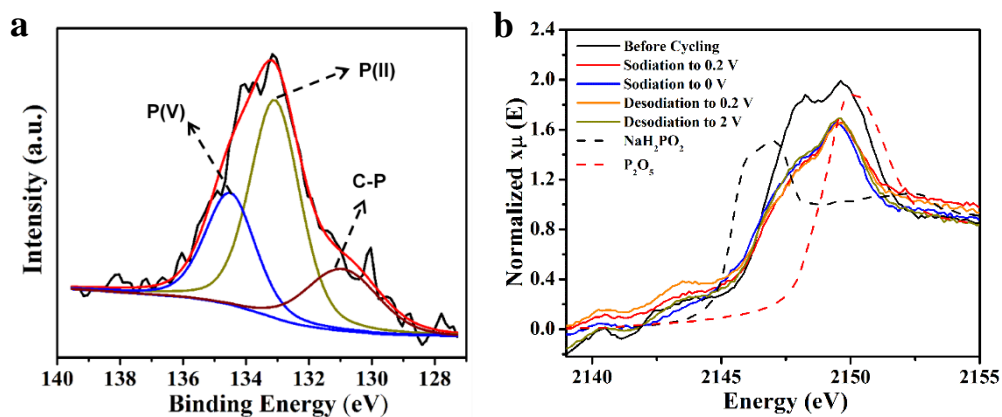


Figure 4.3 X-ray adsorption results of P-HC before cycling and P-HC at various state of charge. (a) XPS P-2p signals of P-HC before cycling. (b) Normalized spectra of ex situ XANES for P-HC anode before cycling and at different state of charge in one galvanostatic cycle of sodiation and desodiation.

P-HC does exhibit an impressive desodiation capacity of 359 mAh/g vs 283 mAh/g (active mass loading: 1.5 to 2 mg/cm²) for the HC at a current density of 20 mA/g, as shown in their potential profiles (Figure 4.4a). The reported capacities in this study are all median values of results from at least five cells. Note that P-HC electrode retains well the key characteristic features of hard carbon—a low operation potential and a relatively high CE@1st, 73%. By positioning the sodiation/desodiation curves of HC and P-HC with an overlapping of their inflection points, it is evident that both the plateau region and the slope region of P-HC are of higher capacities than those of HC. Specifically, the plateau capacity rises from 169 to 222 mAh/g while the slope capacity is increased from 114 to 137 mAh/g.

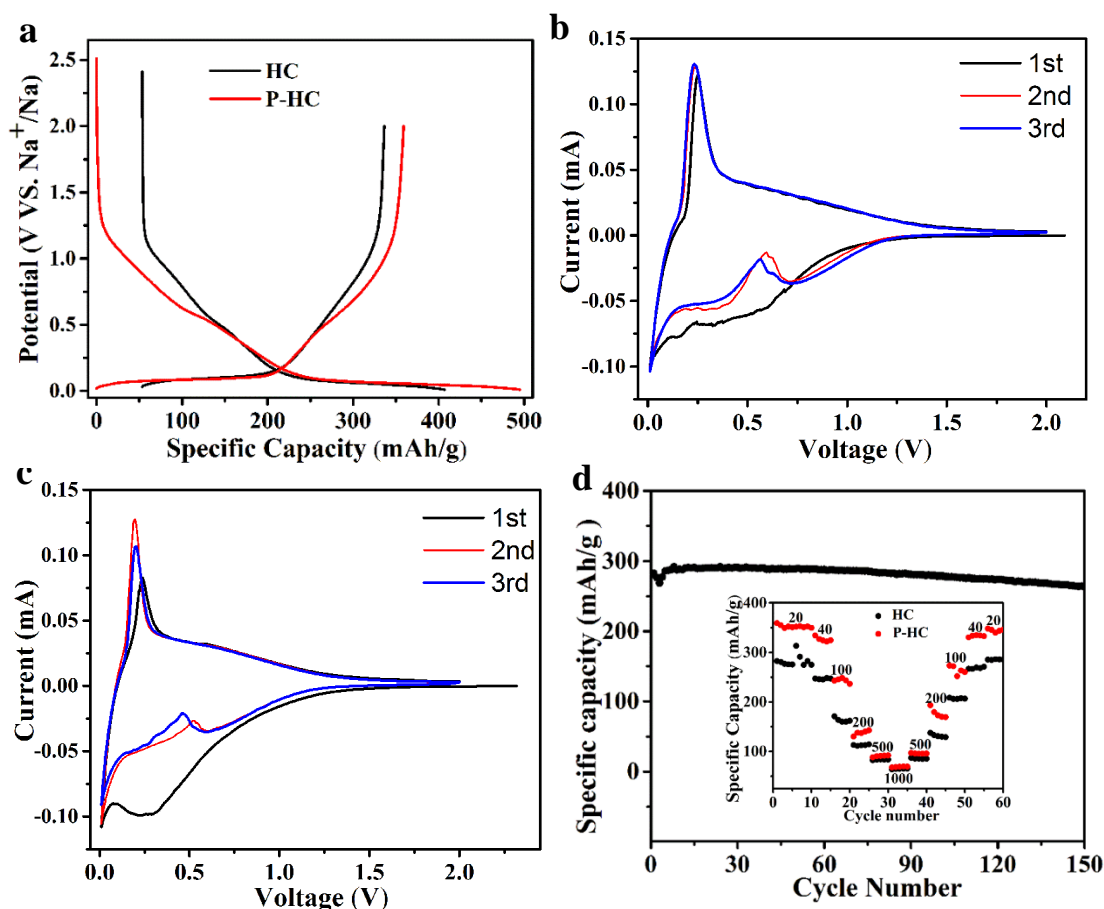


Figure 4.4 Electrochemical studies of hard carbons in C/Na half-cells. The potential is vs Na^+/Na . (a) Sodiatio/desodiation potential profiles of HC and P-HC at a current rate of 20 mA/g. The sodiatio/desodiation profiles of HC are shifted right to show its difference from the profiles of P-HC. (b,c) CV curves during initial cycling of various carbon anodes at a scan rate of 0.1 mV/s in a potential range of 0.01-2 V of (b) HC and (c) P-HC. (d) Cycling performance of P-HC, the carbon electrode is sodiated at 40 mA/g and desodiated at 200 mA/g in the potential range of 0.01-2 V vs Na^+/Na . Inset in (d) is the rate performance of HC and P-HC electrodes at various current densities from 20 to 1000 mA/g.

One question is whether the GO trapped in the hard carbon structure contributes to the high capacity of P-HC. First of all, it is important to note that GO does not occupy much mass of the final products as the mass ratio between sucrose and GO during preparation

is as high as 80/1. The above question can be answered by comparing the electrochemical behavior in cyclic voltammetry (CV) of P-HC, HC and a pyrolyzed sucrose without GO addition (Figure 4.4b, c and Figure 4.5a). In fact, the trapped GO is redox active, revealed by the very different shapes of CV peaks of both HC and P-HC, compared to the pure pyrolyzed sucrose. Both HC and P-HC exhibit cathodic peaks at 0.75 V and 0.35 V vs Na^+/Na in the second and the third CV cycle, whereas pure pyrolyzed sucrose does not. Furthermore, the reduction reactions shown by the cathodic peaks appear reversible, demonstrated by the broad anodic current bump. Figure 4.5b shows that these cathodic peaks of HC do not decay much even on the 6th cycle, indicating the redox reactivity and its reversibility of the trapped GO. Unfortunately, HC's limited capacity of 283 mAh/g clearly shows that GO's contribution to the additional capacity of P-HC is quite limited.

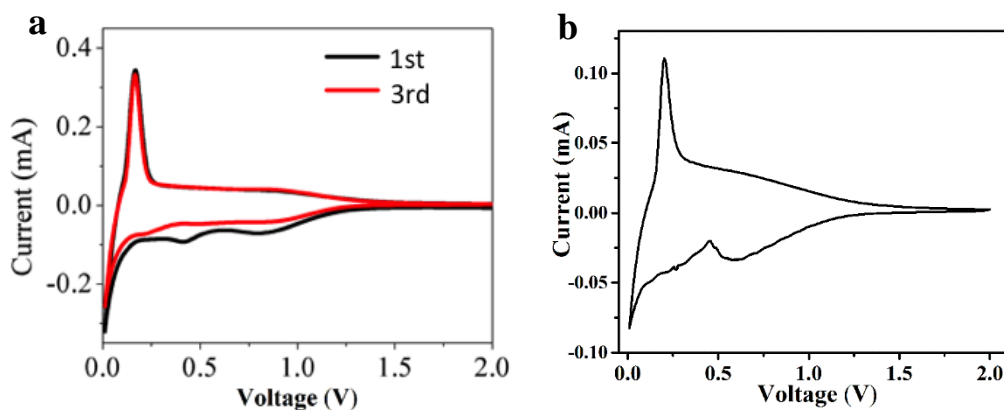


Figure 4.5 CV curves of two carbon anodes at a scan rate of 0.1 mV/s in a potential range of 0.01-2 V. (a) Pyrolyzed sucrose without addition of graphene oxide. (b) The 6th cycle CV curve of HC (GO was added).

The cathodic scans in the first CV cycle of all carbon anodes show a certain level of irreversibility, which is related to the well-known SEI formation. Particularly, P-HC exhibits an irreversible cathodic peak at $\sim 0.2-0.4$ V, which can only be assigned to reduction of PO_x species. This irreversible behavior explains a slightly lower $\text{CE}@1\text{st}$ for P-HC than HC. In CV curves of all P-HC, HC, and pyrolyzed sucrose, a couple of sharp cathodic and anodic peaks at around 0.1 V vs Na^+/Na are attributed to the insertion and extraction of Na-ions with the hard carbon structures, respectively.

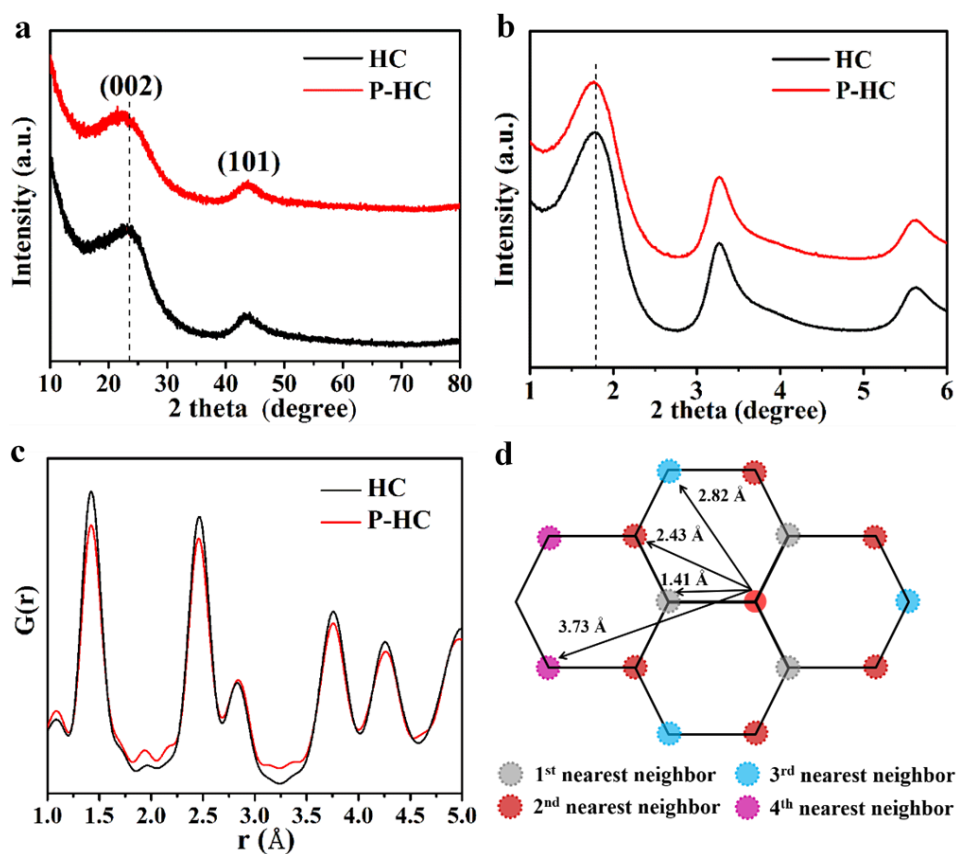


Figure 4.6 X-ray diffraction and neutron total scattering studies of P-HC. (a,b) XRD results of HC and P-HC (a) Laboratory XRD patterns and (b) Synchrotron XRD patterns. (c-d) PDF results show local atomic order along ab planes (c) PDF within 5 Å from neutron total scattering of HC and P-HC. (d) Schematic showing local pairs along graphene sheet.

P-HC exhibits a much higher capacity than HC, which could be the results of two major factors—the possible redox reactivity of PO_x and/or the favorable changes of carbon structures. For PO_x 's reactivity, as the CV results show, PO_x could be reduced to a certain extent in the first sodiation. The question is whether such redox reactions contribute to the higher desodiation capacity of P-HC. To address this question, we monitor the evolving oxidation states of phosphorus by *ex situ* XANES at selected state of charge (SOC) (Figure 4.3b). After the first sodiation to 0.2 V vs Na^+/Na , both phosphorus peaks in XANES at 2146.4 and 2149.0 eV become less intense, where the former diminishes much more significantly than the latter. Interestingly, intensity of the two peaks no longer change upon further sodiation to 0.01 V and the following desodiation. Combining this observation and the aforementioned CV results gives rise to two important insights. Firstly, the relatively low CE@1st (73%) for P-HC is primarily caused by the irreducible reduction of P(III). Secondly, PO_x does not contribute to the higher desodiation capacity of P-HC, where such higher capacity must be the result of the altered local structures of hard carbon.

The structural changes of hard carbon can be primarily from two directions: along c-axis and across ab planes. Figure 4.6a shows the x-ray diffraction (XRD) patterns of HC and P-HC, showing that PO_x doping enlarges the (002) d-spacing from 3.79 to 3.86 Å as the (002) peak shifts from 23.6° to 23.0° . We also conducted synchrotron XRD measurements, where the (002) peak shifts from 1.78° to 1.76° , confirming the d-spacing enlargement (Figure 4.6b). As reported by Huang et al., a larger (002) d-spacing

should increase the capacity of hard carbon materials for Na-ion storage.⁵³ Herein, we assign the significant increase of the plateau capacity from 169 to 222 mAh/g to the enlarged d-spacing (Figure 4.4a). It is reasonable to consider that a larger d-spacing would facilitate intercalation of more Na-ions in between the carbon layers of TNs inside hard carbon.

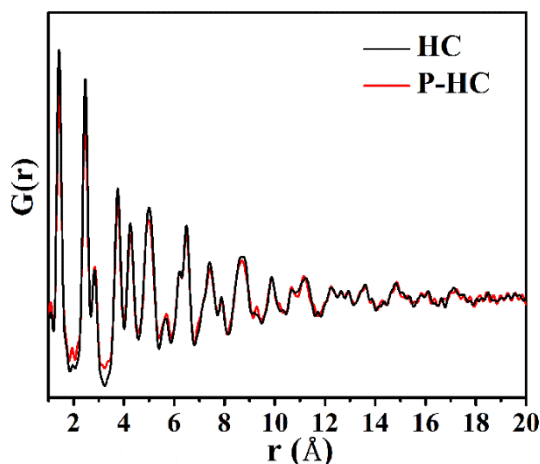


Figure 4.7 Neutron total scattering results of HC and P-HC in a range of 20 Å.

In addition, PO_x doping also generates large impacts on local structures along *ab* plane, revealed by neutron total scattering and the associated pair distribution function (PDF). As Figure 4.6c shows, $G(r)$ peak intensity decreases after doping. $G(r)$ peak intensity is proportional to the scattering power of the atoms and the coordination number of the correlated pair (Figure 4.6d).⁶⁹ The observed lower intensity cannot only be explained by the change in scattering power, which suggests a more defective structure along *ab* planes. This evidence further confirms that the structure of P-HC is more defective after PO_x doping. There is no peak or shoulder at 3.4-3.5 Å for both HC and P-HC, which

indicates that graphene sheets are not stacked with an ordered AB type registry as they do in graphite. As shown in the long-range neutron total scattering results (Figure 4.7), the peaks diminished and are almost gone at 20 Å. The loss of structural coherence above 20 Å is most likely due to the curvature of the sheets, which can be seen from the TEM images (Figure 4.2c and d). Raman spectra were also collected for both HC and P-HC, which are deconvoluted into four Lorentzian peaks according to Hu et al. (Figure 4.8).⁷⁰ The I_D/I_G values determined by the intensity ratios of D-band ($\sim 1350\text{ cm}^{-1}$) over G-band ($\sim 1590\text{ cm}^{-1}$) are 1.30 and 1.39 for HC and P-HC, respectively. The increased I_D/I_G value indicates that the average L_a values along ab planes in TNs decreased after PO_x doping, which means that there are more edge carbon atoms in P-HC due to the smaller domains sizes. This agrees with the neutron scattering and the PDF results. We attribute P-HC's higher capacity from the slope region, raised from 114 to 137 mAh/g to the more defects induced by PO_x doping (Figure 4.4a). The assignment for the capacity enhanced in both plateau and slope regions are well aligned with and can be explained by the recently reported sodium storage models in hard carbon.^{47, 71, 72}

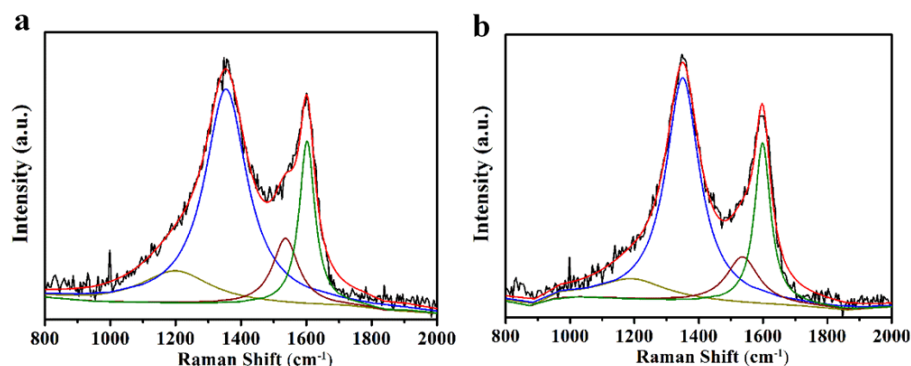


Figure 4.8 Raman spectra of the (a) HC and (b) P-HC and their fitting curves with TPA (dark yellow), D (blue), A (wine), G (green).

Lastly, we evaluate the rate performance of P-HC and HC at different current densities, ranging from 20 to 1000 mA/g and the cycling performance of P-HC (Figure 4.4d). Compared with HC, P-HC exhibits a higher capacity at all current densities, especially at low current rates. With the current density switched back to 20 mA/g, the capacity of 346 mAh/g is still retained by P-HC after 60 cycles. The doping does not affect the cycling performance of hard carbon negatively. For longer cycling performance, we sodiate and desodiate P-HC at 40 mA/g and 200 mA/g, respectively. After 150 cycles, P-HC retains 92% of its original capacity.

4.5 Conclusion

In summary, we increase the capacity of a model hard carbon from 283 mAh/g to 359 mAh/g, one of the highest capacity values, by doping this low-surface-area hard carbon with PO_x . The key electrochemical characteristics of hard carbon are retained. Near-atomic dispersion of PO_x in hard carbon is achieved. Doping does increase (002) d-spacing and causes a more defective structure across ab planes. We confirm that the doped PO_x does not contribute to the higher capacity by redox reactions. The evidence suggests that the enlarged interlayer d-spacing and the more defective structure are responsible for the enhanced capacity. This study provides important insights on the design principle of local atomic structures in hard carbon as an anode in NIBs.

4.6 References

- (1) Lin, M.-C.; Gong, M.; Lu, B.; Wu, Y.; Wang, D.-Y.; Guan, M.; Angell, M.; Chen, C.; Yang, J.; Hwang, B.-J. An ultrafast rechargeable aluminium-ion battery. *Nature* **2015**, *520*, 324-328.
- (2) Cohn, G.; Ma, L.; Archer, L. A. A novel non-aqueous aluminum sulfur battery. *J. Power Sources* **2015**, *283*, 416-422.
- (3) Saha, P.; Datta, M. K.; Velikokhatnyi, O. I.; Manivannan, A.; Alman, D.; Kumta, P. N. Rechargeable magnesium battery: Current status and key challenges for the future. *Prog. Mater. Sci.* **2014**, *66*, 1-86.
- (4) Wu, N.; Yang, Z. Z.; Yao, H. R.; Yin, Y. X.; Gu, L.; Guo, Y. G. Improving the Electrochemical Performance of the $\text{Li}_4\text{Ti}_5\text{O}_{12}$ Electrode in a Rechargeable Magnesium Battery by Lithium–Magnesium Co-Intercalation. *Angew. Chem. Int. Ed.* **2015**, *127*, 5849-5853.
- (5) Jian, Z.; Luo, W.; Ji, X. Carbon Electrodes for K-Ion Batteries. *J. Am. Chem. Soc.* **2015**, *137*, 11566-11569.
- (6) Lu, X.; Bowden, M. E.; Sprenkle, V. L.; Liu, J. A Low Cost, High Energy Density, and Long Cycle Life Potassium–Sulfur Battery for Grid-Scale Energy Storage. *Adv. Mater.* **2015**, *27*, 5915-5922.
- (7) Luo, W.; Shen, F.; Bommier, C.; Zhu, H.; Ji, X.; Hu, L. Na-Ion Battery Anodes: Materials and Electrochemistry. *Acc. Chem. Res.* **2016**, *49*, 231–240.
- (8) Kundu, D.; Talaie, E.; Duffort, V.; Nazar, L. F. The emerging chemistry of sodium ion batteries for electrochemical energy storage. *Angew. Chem. Int. Ed.* **2015**, *54*, 3431-3448.
- (9) Lee, H. W.; Wang, R. Y.; Pasta, M.; Lee, S. W.; Liu, N.; Cui, Y. Manganese hexacyanomanganate open framework as a high-capacity positive electrode material for sodium-ion batteries. *Nat. Commun.* **2014**, *5*, 5280.
- (10) Kundu, D.; Tripathi, R.; Popov, G.; Makahnouk, W.; Nazar, L. F. Synthesis, Structure, and Na-Ion Migration in $\text{Na}_4\text{NiP}_2\text{O}_7\text{F}_2$: A Prospective High Voltage Positive Electrode Material for the Na-Ion Battery. *Chem. Mater.* **2015**, *27*, 885-891.
- (11) Liu, Y.; Xu, Y.; Han, X.; Pellegrinelli, C.; Zhu, Y.; Zhu, H.; Wan, J.; Chung, A. C.; Vaaland, O.; Wang, C. Porous amorphous FePO_4 nanoparticles connected by single-wall carbon nanotubes for sodium ion battery cathodes. *Nano Lett.* **2012**, *12*, 5664-5668.
- (12) Hwang, J.-Y.; Oh, S.-M.; Myung, S.-T.; Chung, K. Y.; Belharouak, I.; Sun, Y.-K. Radially aligned hierarchical columnar structure as a cathode material for high energy density sodium-ion batteries. *Nat. Commun.* **2015**, *6*, 6865.

- (13) Oh, S.-M.; Myung, S.-T.; Yoon, C. S.; Lu, J.; Hassoun, J.; Scrosati, B.; Amine, K.; Sun, Y.-K. Advanced Na[Ni_{0.25}Fe_{0.5}Mn_{0.25}]O₂/C–Fe₃O₄ sodium-ion batteries using EMS electrolyte for energy storage. *Nano Lett.* **2014**, *14*, 1620-1626.
- (14) Yuan, S.; Liu, Y. B.; Xu, D.; Ma, D. L.; Wang, S.; Yang, X. H.; Cao, Z. Y.; Zhang, X. B. Pure Single-Crystalline Na_{1.1}V₃O_{7.9} Nanobelts as Superior Cathode Materials for Rechargeable Sodium-Ion Batteries. *Adv. Sci.* **2015**, *2*, 1400018.
- (15) Berthelot, R.; Carlier, D.; Delmas, C. Electrochemical investigation of the P2–Na_xCoO₂ phase diagram. *Nat. Mater.* **2011**, *10*, 74-80.
- (16) Yabuuchi, N.; Kajiyama, M.; Iwatate, J.; Nishikawa, H.; Hitomi, S.; Okuyama, R.; Usui, R.; Yamada, Y.; Komaba, S. P2-type Na_x[Fe_{1/2}Mn_{1/2}]O₂ made from earth-abundant elements for rechargeable Na batteries. *Nat. Mater.* **2012**, *11*, 512-517.
- (17) Guo, S.; Liu, P.; Sun, Y.; Zhu, K.; Yi, J.; Chen, M.; Ishida, M.; Zhou, H. A High-Voltage and Ultralong-Life Sodium Full Cell for Stationary Energy Storage. *Angew. Chem., Int. Ed.* **2015**, *54*, 11701-11705.
- (18) Mu, L.; Xu, S.; Li, Y.; Hu, Y. S.; Li, H.; Chen, L.; Huang, X. Prototype Sodium-Ion Batteries Using an Air-Stable and Co/Ni-Free O3-Layered Metal Oxide Cathode. *Adv. Mater.* **2015**, *27*, 6928-6933.
- (19) Li, Y.; Wang, D.; An, Q.; Ren, B.; Rong, Y.; Yao, Y. Flexible electrode for long-life rechargeable sodium-ion batteries: effect of oxygen vacancy in MoO_{3-x}. *J. Mater. Chem. A* **2016**, *4*, 5402–5405.
- (20) Jian, Z.; Han, W.; Lu, X.; Yang, H.; Hu, Y. S.; Zhou, J.; Zhou, Z.; Li, J.; Chen, W.; Chen, D. Superior Electrochemical Performance and Storage Mechanism of Na₃V₂(PO₄)₃ Cathode for Room-Temperature Sodium-Ion Batteries. *Adv. Energy Mater.* **2013**, *3*, 156-160.
- (21) Li, S.; Dong, Y.; Xu, L.; Xu, X.; He, L.; Mai, L. Effect of Carbon Matrix Dimensions on the Electrochemical Properties of Na₃V₂(PO₄)₃ Nanograins for High-Performance Symmetric Sodium-Ion Batteries. *Adv. Mater.* **2014**, *26*, 3545-3553.
- (22) Wang, X.; Niu, C.; Meng, J.; Hu, P.; Xu, X.; Wei, X.; Zhou, L.; Zhao, K.; Luo, W.; Yan, M., et al. Novel K₃V₂(PO₄)₃/C Bundled Nanowires as Superior Sodium-Ion Battery Electrode with Ultrahigh Cycling Stability. *Adv. Energy Mater.* **2015**, *5*, 1500716.
- (23) Zhu, C.; Kopold, P.; van Aken, P. A.; Maier, J.; Yu, Y. High Power–High Energy Sodium Battery Based on Threefold Interpenetrating Network. *Adv. Mater.* **2016**, *28*, 2409–2416.
- (24) Darwiche, A.; Marino, C.; Sougrati, M. T.; Fraise, B.; Stievano, L.; Monconduit, L. Better cycling performances of bulk Sb in Na-ion batteries compared to Li-ion systems: an unexpected electrochemical mechanism. *J. Am. Chem. Soc.* **2012**, *134*, 20805-20811.

- (25) Farbod, B.; Cui, K.; Kalisvaart, W. P.; Kupsta, M.; Zahiri, B.; Kohandehghan, A.; Lotfabad, E. M.; Li, Z.; Lubner, E. J.; Mitlin, D. Anodes for sodium ion batteries based on tin–germanium–antimony alloys. *ACS Nano* **2014**, *8*, 4415–4429.
- (26) Mao, J.; Fan, X.; Luo, C.; Wang, C. Building self-healing alloy architecture for stable sodium-ion batteries anodes: a case study of Tin anode materials. *ACS Appl. Mater. Interfaces* **2016**, *8*, 7147–7155.
- (27) Ni, J.; Fu, S.; Wu, C.; Maier, J.; Yu, Y.; Li, L. Self-Supported Nanotube Arrays of Sulfur-Doped TiO₂ Enabling Ultrastable and Robust Sodium Storage. *Adv. Mater.* **2016**, *28*, 2259–2265.
- (28) Zhu, X.; Li, Q.; Fang, Y.; Liu, X.; Xiao, L.; Ai, X.; Yang, H.; Cao, Y. Graphene-Modified TiO₂ Microspheres Synthesized by a Facile Spray-Drying Route for Enhanced Sodium-Ion Storage. *Part. Part. Syst. Charact.* **2016**, *33*, 545–552.
- (29) Qian, J. F.; Wu, X. Y.; Cao, Y. L.; Ai, X. P.; Yang, H. X. High Capacity and Rate Capability of Amorphous Phosphorus for Sodium Ion Batteries. *Angew. Chem., Int. Ed.* **2013**, *52*, 4633–4636.
- (30) Jie Sun, H.-W. L., Mauro Pasta, Hongtao Yuan, Guangyuan Zheng, Yongming Sun, Li, Yuzhang; Cui, Y. A phosphorene–graphene hybrid material as a high-capacity anode for sodium-ion batteries. *Nat. Nanotechnol.* **2015**, *10*, 980–985.
- (31) Seh, Z. W.; Sun, J.; Sun, Y.; Cui, Y. A highly reversible room-temperature sodium metal anode. *ACS Cent. Sci.* **2015**, *1*, 449–455.
- (32) Jache, B.; Adelhelm, P. Use of Graphite as a Highly Reversible Electrode with Superior Cycle Life for Sodium-Ion Batteries by Making Use of Co-Intercalation Phenomena. *Angew. Chem. Int. Ed.* **2014**, *53*, 10169–10173.
- (33) Wen, Y.; He, K.; Zhu, Y.; Han, F.; Xu, Y.; Matsuda, I.; Ishii, Y.; Cumings, J.; Wang, C. Expanded graphite as superior anode for sodium-ion batteries. *Nat. Commun.* **2014**, *5*, 4033.
- (34) David, L.; Singh, G. reduced graphene oxide paper electrode: opposing effect of thermal annealing on Li and Na cyclability. *J. Phys. Chem. C* **2014**, *118*, 28401–28408.
- (35) Luo, W.; Jian, Z.; Xing, Z.; Wang, W.; Bommier, C.; Lerner, M. M.; Ji, X. Electrochemically Expandable Soft Carbon as Anodes for Na-Ion Batteries. *ACS Cent. Sci.* **2015**, *1*, 516–522.
- (36) Li, H.; Shen, F.; Luo, W.; Dai, J.; Han, X.; Chen, Y.; Yao, Y.; Fu, K.; Zhu, H.; Hitz, E. M. Carbonized leaf membrane with anisotropic surfaces for sodium ion battery. *ACS Appl. Mater. Interfaces* **2016**, *8*, 2204–2210.
- (37) Jo, C.; Park, Y.; Jeong, J.; Lee, K. T.; Lee, J. Structural effect on electrochemical performance of ordered porous carbon electrodes for Na-ion batteries. *ACS Appl. Mater. Interfaces* **2015**, *7*, 11748–11754.
- (38) Li, Y.; Xu, S.; Wu, X.; Yu, J.; Wang, Y.; Hu, Y.-S.; Li, H.; Chen, L.; Huang, X. Amorphous monodispersed hard carbon micro-spherules derived from biomass as a

high performance negative electrode material for sodium-ion batteries. *J. Mater. Chem. A* **2015**, *3*, 71-77.

(39) Franklin, R. E. Crystallite growth in graphitizing and nongraphitizing carbons. *Proc. R. Soc. London, Ser. A* **1951**, *209*, 196–218.

(40) Stevens, D.; Dahn, J. High Capacity Anode Materials for Rechargeable Sodium-Ion Batteries. *J. Electrochem. Soc.* **2000**, *147*, 1271-1273.

(41) Xiao, L.; Cao, Y.; Henderson, W. A.; Sushko, M. L.; Shao, Y.; Xiao, J.; Wang, W.; Engelhard, M. H.; Nie, Z.; Liu, J. Hard carbon nanoparticles as high-capacity, high-stability anodic materials for Na-ion batteries. *Nano Energy* **2016**, *19*, 279-288.

(42) Ponrouch, A.; Goñi, A.; Palacín, M. R. High capacity hard carbon anodes for sodium ion batteries in additive free electrolyte. *Electrochem. Commun.* **2013**, *27*, 85-88.

(43) Luo, W.; Wang, B.; Heron, C. G.; Allen, M. J.; Morre, J.; Maier, C. S.; Stickle, W. F.; Ji, X. Pyrolysis of cellulose under ammonia leads to nitrogen-doped nanoporous carbon generated through methane formation. *Nano Lett.* **2014**, *14*, 2225-2229.

(44) Li, Y.; Hu, Y.-S.; Li, H.; Chen, L.; Huang, X. A superior low-cost amorphous carbon anode made from pitch and lignin for sodium-ion batteries. *J. Mater. Chem. A* **2016**, *4*, 96–104.

(45) Lotfabad, E. M.; Ding, J.; Cui, K.; Kohandehghan, A.; Kalisvaart, W. P.; Hazelton, M.; Mitlin, D. High-density sodium and lithium ion battery anodes from banana peels. *ACS Nano* **2014**, *8*, 7115-7129.

(46) Memarzadeh, E.; Kalisvaart, P.; Kohandehghan, A.; Mitlin, D. Origin of non-SEI related coulombic efficiency loss in carbons tested against Na and Li. *J. Mater. Chem. A* **2014**, *2*, 19685-19695.

(47) Ding, J.; Wang, H.; Li, Z.; Kohandehghan, A.; Cui, K.; Xu, Z.; Zahiri, B.; Tan, X.; Lotfabad, E. M.; Olsen, B. C. Carbon nanosheet frameworks derived from peat moss as high performance sodium ion battery anodes. *ACS Nano* **2013**, *7*, 11004-11015.

(48) Wang, Z.; Qie, L.; Yuan, L.; Zhang, W.; Hu, X.; Huang, Y. Functionalized N-doped interconnected carbon nanofibers as an anode material for sodium-ion storage with excellent performance. *Carbon* **2013**, *55*, 328-334.

(49) Fu, L.; Tang, K.; Song, K.; van Aken, P. A.; Yu, Y.; Maier, J. Nitrogen doped porous carbon fibres as anode materials for sodium ion batteries with excellent rate performance. *Nanoscale* **2014**, *6*, 1384-1389.

(50) Wang, H. G.; Wu, Z.; Meng, F. L.; Ma, D. L.; Huang, X. L.; Wang, L. M.; Zhang, X. B. Nitrogen-Doped Porous Carbon Nanosheets as Low-Cost, High-Performance Anode Material for Sodium-Ion Batteries. *ChemSusChem* **2013**, *6*, 56-60.

(51) Wang, P.; Qiao, B.; Du, Y.; Li, Y.; Zhou, X.; Dai, Z.; Bao, J. Fluorine-Doped Carbon Particles Derived from Lotus Petioles as High-Performance Anode Materials for Sodium-Ion Batteries. *J. Phys. Chem. C* **2015**, *119*, 21336-21344.

- (52) Hong, K.-l.; Qie, L.; Zeng, R.; Yi, Z.-q.; Zhang, W.; Wang, D.; Yin, W.; Wu, C.; Fan, Q.-j.; Zhang, W.-x., et al. Biomass derived hard carbon used as a high performance anode material for sodium ion batteries. *J. Mater. Chem. A* **2014**, *2*, 12733-12738.
- (53) Xu, D.; Chen, C.; Xie, J.; Zhang, B.; Miao, L.; Cai, J.; Huang, Y.; Zhang, L. A Hierarchical N/S-Codoped Carbon Anode Fabricated Facilely from Cellulose/Polyaniline Microspheres for High-Performance Sodium-Ion Batteries. *Adv. Energy Mater.* **2016**, *6*, 1501929.
- (54) Yan, D.; Yu, C.; Zhang, X.; Qin, W.; Lu, T.; Hu, B.; Li, H.; Pan, L. Nitrogen-doped carbon microspheres derived from oatmeal as high capacity and superior long life anode material for sodium ion battery. *Electrochim Acta* **2016**, *191*, 385–391.
- (55) Wen, Y.; Wang, B.; Luo, B.; Wang, L. Long-Term Cycling Performance of Nitrogen-Doped Hollow Carbon Nanospheres as Anode Materials for Sodium-Ion Batteries. *Eur. J. Inorg. Chem.* **2016**, *2016*, 2051–2055.
- (56) Zhang, J.; Zhang, Z.; Zhao, X. A graphene/nitrogen-doped carbon nanofiber composite as an anode material for sodium-ion batteries. *RSC Advances* **2015**, *5*, 104822-104828.
- (57) Selvamani, V.; Ravikumar, R.; Suryanarayanan, V.; Velayutham, D.; Gopukumar, S. Garlic peel derived high capacity hierarchical N-doped porous carbon anode for sodium/lithium ion cell. *Electrochim. Acta* **2016**, *190*, 337-345.
- (58) Li, Y.; Wang, Z.; Li, L.; Peng, S.; Zhang, L.; Srinivasan, M.; Ramakrishna, S. Preparation of nitrogen-and phosphorous co-doped carbon microspheres and their superior performance as anode in sodium-ion batteries. *Carbon* **2016**, *99*, 556-563.
- (59) Wang, S.; Xia, L.; Yu, L.; Zhang, L.; Wang, H.; Lou, X. W. D. Free-Standing Nitrogen-Doped Carbon Nanofiber Films: Integrated Electrodes for Sodium-Ion Batteries with Ultralong Cycle Life and Superior Rate Capability. *Adv. Energy Mater.* **2015**, *6*, 1502217.
- (60) Li, W.; Zhou, M.; Li, H.; Wang, K.; Cheng, S.; Jiang, K. A High Performance Sulfur-Doped Disordered Carbon Anode for Sodium Ion Batteries. *Energy Environ. Sci.* **2015**, *8*, 2916–2921.
- (61) Qie, L.; Chen, W.; Xiong, X.; Hu, C.; Zou, F.; Hu, P.; Huang, Y. Sulfur-Doped Carbon with Enlarged Interlayer Distance as a High-Performance Anode Material for Sodium-Ion Batteries. *Adv. Sci.* **2015**, *2*, 1500195.
- (62) Teng, H.; Yeh, T.-S.; Hsu, L.-Y. Preparation of activated carbon from bituminous coal with phosphoric acid activation. *Carbon* **1998**, *36*, 1387-1395.
- (63) Paraknowitsch, J. P.; Thomas, A. Doping carbons beyond nitrogen: an overview of advanced heteroatom doped carbons with boron, sulphur and phosphorus for energy applications. *Energ. Environ. Sci.* **2013**, *6*, 2839-2855.

- (64) Bommier, C.; Luo, W.; Gao, W.-Y.; Greaney, A.; Ma, S.; Ji, X. Predicting capacity of hard carbon anodes in sodium-ion batteries using porosity measurements. *Carbon* **2014**, *76*, 165-174.
- (65) Luo, W.; Bommier, C.; Jian, Z.; Li, X.; Carter, R.; Vail, S.; Lu, Y.; Lee, J.-J.; Ji, X. Low-surface-area hard carbon anode for Na-ion batteries via graphene oxide as a dehydration agent. *ACS Appl. Mater. Interfaces* **2015**, *7*, 2626-2631.
- (66) Latorre-Sánchez, M.; Primo, A.; García, H. P-Doped Graphene Obtained by Pyrolysis of Modified Alginate as a Photocatalyst for Hydrogen Generation from Water–Methanol Mixtures. *Angew. Chem., Int. Ed.* **2013**, *52*, 11813-11816.
- (67) Qu, B.; Ma, C.; Ji, G.; Xu, C.; Xu, J.; Meng, Y. S.; Wang, T.; Lee, J. Y. Layered SnS₂-Reduced Graphene Oxide Composite—A High-Capacity, High-Rate, and Long-Cycle Life Sodium-Ion Battery Anode Material. *Adv. Mater.* **2014**, *26*, 3854-3859.
- (68) Khare, N.; Martin, J. D.; Hesterberg, D. Phosphate bonding configuration on ferrihydrite based on molecular orbital calculations and XANES fingerprinting. *Geochim. Cosmochim. Acta* **2007**, *71*, 4405-4415.
- (69) Petkov, V.; DiFrancesco, R.; Billinge, S.; Acharya, M.; Foley, H. Local structure of nanoporous carbons. *Philos. Mag. B* **1999**, *79*, 1519-1530.
- (70) Hu, C.; Sedghi, S.; Silvestre-Albero, A.; Andersson, G. G.; Sharma, A.; Pendleton, P.; Rodríguez-Reinoso, F.; Kaneko, K.; Biggs, M. J. Raman spectroscopy study of the transformation of the carbonaceous skeleton of a polymer-based nanoporous carbon along the thermal annealing pathway. *Carbon* **2015**, *85*, 147-158.
- (71) Bommier, C.; Surta, T. W.; Dolgos, M.; Ji, X. New mechanistic insights on Na-ion storage in nongraphitizable carbon. *Nano Lett.* **2015**, *15*, 5888-5892.
- (72) Tsai, P. C.; Chung, S. C.; Lin, S. K.; Yamada, A. Ab initio study of sodium intercalation into disordered carbon. *J. Mater. Chem. A* **2015**, *3*, 9763-9768.

Chapter 5 Mechanism of Na-Ion Storage in Hard Carbon Anodes Revealed by Heteroatom Doping

5.1 Abstract

Hard carbon is the leading candidate anode for commercialization of Na-ion batteries. Hard carbon has a unique local atomic structure, which is composed of nanodomains of layered rumpled sheets that have short-range local order resembling graphene within each layer but complete disorder along the c-axis between layers. A primary challenge holding back the development of Na-ion batteries is that a complete understanding of the structure-capacity correlations of Na-ion storage in hard carbon has remained elusive. This article presents two key discoveries: first that characteristics of hard carbon's structure can be modified systematically by heteroatom doping, and second, that these structural changes greatly affect Na-ion storage properties, which reveals the mechanisms for Na storage in hard carbon. Specifically, via P or S doping, the interlayer spacing is dilated, which extends the low-voltage plateau capacity, while increasing the defect concentration with P or B doping leads to higher slope sodiation capacity. Our combined experimental studies and first principles calculations reveal that it is the Na-ion-defect binding that corresponds to the slope capacity, while the Na intercalation between graphenic layers causes the low-potential plateau capacity. The new understanding provides a new set of guiding principles to optimize hard carbon for Na-ion battery applications.

5.2 Introduction

Na-ion batteries (NIBs) represent one of the most promising solutions for grid-scale storage of electrical energy produced by intermittent renewable energy sources, such as wind and solar power. Their potential for massive scale-up is high because they are electrochemically similar to Li-ion batteries (LIBs), but unlike LIBs can be composed entirely of inexpensive and earth abundant elements. Cathode materials, including layered oxides and polyanion compounds, have exhibited very promising performance for NIBs.¹⁻⁵ Unfortunately the principal anode materials for LIBs, graphite, only stores sodium up to a stoichiometry of NaC_{64} , one tenth of its capacity for lithium storage unless graphite is expanded or solvent co-intercalation occurs,^{6, 7} and so alternative anode materials are being sought. These candidate materials, in addition to having high sodium capacity, must also meet the requirements for scale-up by being inexpensive to produce in large quantities with minimal environmental impact.

Currently the most promising candidate is an allotrope of carbon called *hard carbon*. This is an amorphous form of turbostratic carbon comprising nanoscale domains of stacked ruffled graphenic sheets.⁸ Within each plane, the sheets have graphene-like order, but the sheets lack long-range ordering and are therefore disordered along the *c*-axis. The titular adjective *hard* refers to the material's reluctance to transform to graphite during annealing and its sp^3 carbon atoms contained, and as such it is also known as non-graphitizable carbon. The ability of hard carbon to accommodate a large quantity of Na-ions electrochemically was first demonstrated by Stevens and Dahn in

2000.⁹ Since then a worldwide research effort has enhanced this storage capacity, and advanced numerous processes for synthesizing hard carbon from abundant feed stocks, such as sucrose,¹⁰ peat moss,¹¹ cotton,¹² wood¹³ and even banana skins.¹⁴ Most of this advancement has been Edisonian in nature, because efforts to attribute features of the sodiation profile to hard carbon's structure have not fully appreciated the subtlety of its structure. That hard carbon does not readily transform to graphite indicates that, unlike other amorphous (non-graphitic) carbons, its graphenic sheets possess a topology that cannot be unfolded and flattened — topology that is also beneficial for Na-storage.

Early work proposed a Na-ion storage mechanism that followed that for Li, where storage during the sloping region in the sodiation profile is attributed to intercalation of Na-ions into turbostratic nanodomains, and the capacity from the low-potential plateau is attributed to nano-plating inside the enclosed micropores between the domains. Our recent studies lead us to question this model. We annealed hard carbon at high temperatures, with the aim that the resulting increased size of turbostratic nanodomains would increase the capacity under the sloping region of the discharge profile.¹⁵ Instead we found the reverse, that the capacity of the sloping region was reduced. This contradiction suggests an alternative correlation where the removal of defects by annealing results in the decrease of sloping capacity, and thus we tentatively attribute the sloping capacity to favorable binding of Na at local defects rather than indiscriminate Na-ion intercalation. Other experiments have also led us to question which Na storage sites are filled during the plateau region of the discharge profile. X-

ray diffraction measurements of the (002) d-spacing (the average inter-sheet spacing) show marked dilation between sheets during the low-potential plateau sodiation, which indicates that the plateau capacity might originate from inter-sheet intercalation of Na ions instead of nanoplating in micropores.^{11, 16} One can test this hypothesis by determining whether a higher capacity is obtained by a hard carbon with a larger initial (002) d-spacing between the graphene sheets inside turbostratic nanodomains. It is reasonable to hypothesize that a larger initial sheet spacing incurs a lower strain energy penalty for Na-ion intercalation. Recently, Huang *et al.* and Jiang *et al.* investigated heteroatom doping into carbon structures, where these authors report that doping facilitates a larger d-spacing, which is responsible for the higher capacity.^{17, 18} It is important to note that these reported carbons are not conventional hard carbon known by the field as they were pyrolyzed at relatively low temperatures, and therefore do not exhibit a low-potential plateau behavior. So, unfortunately, these doped structures cannot provide mechanistic insights on the Na-ion storage in conventional hard carbon.

A straightforward empirical approach to reveal storage mechanisms is to enhance the hypothesized-desirable local structures of hard carbon and monitor the corresponding capacity variation. The most promising method for engineering the structure of hard carbon is through heteroatom doping, and to date, many dopants have been investigated for various hard carbon materials.^{17, 19-26} However, thus far there has been no systematic knowledge of how doping affects the local structure of hard carbon, and the carbon materials reported in the literature vary hugely in their specific surface areas. This makes

it difficult to compare carbon structures because in materials with large surface area the formation of solid electrolyte interphase (SEI) can mask the reversible capacity from the internal local structures.²⁷

In this article we elucidate the structure-capacity correlation for hard carbon with a systematic set of experiments that address the challenges above using controlled syntheses combined with detailed structural and electrochemical characterization as well as first principles density functional theory (DFT) calculation of Na-ion binding energetics with representative structural sites. The work is presented in two parts. The first demonstrates that we have used boron, phosphorous, and sulfur doping to tune two different structural characteristics of turbostratic nanodomains: the interlayer spacing, and the defect concentration. The second part of the article presents detailed electrochemical characterization of these materials and computational analysis of probable Na storage sites.

We have prepared “conventional” hard carbons by pyrolysis of sucrose at 1100 °C, and all hard carbon samples in this study are of consistently low specific surface areas, *i.e.*, <10 m²/g enabled by our well-established method.^{10, 28} Recently, we reported that P-doped hard carbon exhibits a record-high reversible desodiation capacity of 359 mAh/g at 20 mA/g; though hypothesis of favorable structural sites is raised, the structure-capacity correlation is not solidified.¹⁰ In this study, we introduce two more doped hard carbon materials: B-doped and S-doped additional to the P-doped hard carbon. B-

doping was used to increase the number of in-plane local defects because boron can only form three bonds in the absence of strong Lewis bases, thus B-doping more likely takes place within the graphenic planes. It is either the doped-B atoms or doping-induced carbon vacancies that will serve for the more enhanced presence of in-plane defects. Note that a computational study suggested that boron-doping can improve the performance of graphene as an anode in NIBs.²⁹ We selected doping phosphorus and sulfur to increase the interlayer spacing between graphene sheets by steric occupancy. We used boric acid, phosphoric acid and sulfuric acid as precursors because the respective oxo-acids can be mixed with carbon precursor sucrose in a molecular level, which ensures the near-atomic dispersion of the dopants.

Synthesis of these materials was followed by detailed structural and chemical characterization using x-ray diffraction (XRD), Raman spectroscopy, neutron total scattering, and transition electron microscopy (TEM) equipped with energy-dispersive x-ray mapping (EDX). Together these provided a picture of the doped hard carbons' mesoscale structure, chemical structure, and short- and intermediate-range atomic order. It was revealed that both P- and B-doping that bring more defects produce significantly enlarged Na-storage capacity in the first sodiation sloping region of the potential profiles. Both S- and P-doping increase the interlayer spacing between graphenic sheets and have increased Na-storage capacity in low-potential plateau region. Our computation results further confirm that P- and B-doped sites as well as carbon vacancies bind with inserted Na-ions much more strongly than a defect-free graphene sheet, resulting in relatively

high sodiation potentials—typically seen on the sloping region. Our results provide solid evidence that supports our hypothesis of structure-capacity correlation, where the low-potential plateau is attributed to the Na-ion binding on low-energy sites, most likely inside turbostratic nanodomains and the sloping region corresponds to the Na-ion binding on high-energy defective sites. We also find that the large first sodiation capacity of B-doped hard carbon is highly irreversible in the following desodiation process. Our combined experimental and first principles studies reveal that it is the high binding energy between the in-plane B-dopants and Na-ions that cause the irreversibility. This raises a new trapping mechanism that has nothing to do with solid electrolyte interphase (SEI) and an associated corresponding design principle, where one should avoid introducing high-energy defects inside turbostratic nanodomains.

5.3 Experimental Section

Materials Synthesis: Modified Hummer's method was applied to prepare aqueous GO suspension. In a typical experiment, 2 g sucrose was added to GO suspension (1.8 mg/mL) with a mass ratio of 80:1. Then, an oxo-acid precursor, H_3PO_4 , or H_2SO_4 or H_3BO_3 was added to the suspension with a designed mass ratio of the corresponding dopant of 5 wt% for P-HC, S-HC and B-HC. Un-doped hard carbon suspension was prepared with the same method without adding a dopant precursor. The obtained suspension was dried at 80 °C for 48 h, dehydrated at 180 °C for 24 h, and then pyrolyzed at 1100 °C for 5 h under Ar flow.

Materials Characterization: The doping levels of all doped carbon were measured by inductively coupled plasma optical emission spectrometry (ICP-OES). The density of all carbons were measured by a density measurement kit using cyclohexane as the solvent. N₂ sorption measurements were performed on a Micromeritics TriStar II 3020 analyzer for Brunauer-Emmett-Teller (BET) surface area. X-ray photoelectron spectroscopy (XPS) measurements were performed in a Physical Electronics Quantera Scanning ESCA Microprobe with a focused monochromatic Al K α x-ray (1486.6 eV) source for excitation. The x-ray beam used was a 25 W, 100 μ m x-ray beam spot at the sample. High resolution scanning electron microscopy (SEM) was performed on FEI NOVA 230 to obtain the morphology of all carbons. TEM images were recorded by a FEI Titan 80-200 TEM. The XRD patterns of obtained materials were collected on a Rigaku Ultima IV Diffractometer with Cu K α ($\lambda = 1.5406 \text{ \AA}$) radiation and the patterns were fitted with the PDXL software. WITec confocal Raman spectrometer with a 514 nm laser source was used to gather Raman spectra and the spectra were fitted by Origin 8.5. Neutron total scattering data were collected at the Nanoscale Ordered Materials Diffractometer (NOMAD), Spallation Neutron Source, at Oak Ridge National Laboratory. Samples were loaded into quartz capillaries for analysis.

Electrochemical Measurements: All the electrochemical measurements were done with coin cells (CR2032). The electrodes were composed of active materials, polyvinylidene fluoride (PVdF) and carbon black with a mass ratio of 80:10:10. All these components were mixed together in a mortar and grounded in N-Methyl-2-

pyrrolidone (NMP), and the obtained slurry is coated onto Al foil by doctor blade and dried at 100 °C for 12 h under vacuum. The active mass loading for all electrodes are between 1.5 to 2 mg/cm². The counter/reference electrode was sodium metal and the electrolyte was 1.0 mol/L NaPF₆ solution in ethylene carbonate (EC)/diethyl carbonate (DEC) (1:1 in volume). Arbin BT2000 system was used to test galvanostatic sodiation/desodiation in the potential range of 0.01-2 V vs Na⁺/Na under room temperature.

Computation Section

Calculations were performed with the Vienna ab initio simulation package (VASP)³⁰⁻³² using projector augmented wave (PAW) pseudopotentials^{33, 34} with general gradient approximation (GGA) and the Perdew–Burke–Ernzerhof (PBE) exchange-correlation functional.³⁵ Additionally, the DFT-D3 method^{36, 37} was used to account for the long-range van der waals forces present within the system. An energy cutoff of 500 eV was, and a 6x1x1 Monkhorst-Pack³⁸ KPOINT scheme was used for the brillouin zone integration. Semi-core electronic states for the atoms were used.

The graphene sheets, and doped graphene sheets were designed using a self-made program, and rendered into VASP using the Atomic Simulation Environment (ASE) programming package. The heteroatoms tested were boron, and phosphorous, while the defects included in graphene layers were monovacancy, divacancy, and ‘edge-like’ defects. The graphene layers were ionically relaxed until the force present was of less than 0.01eV/Angstrom. Voltages were obtained by comparing the value of the final structure with the sodium atom, to that of the

unsodiated graphene structure, and the energy of a sodium metal atom in a BCC unit cell. That energy was found to be -1.31 eV, which is in accordance to what had been previously found.³⁹

5.4 Results and Discussion

5.4.1. Structure Characterization of Synthesized Materials

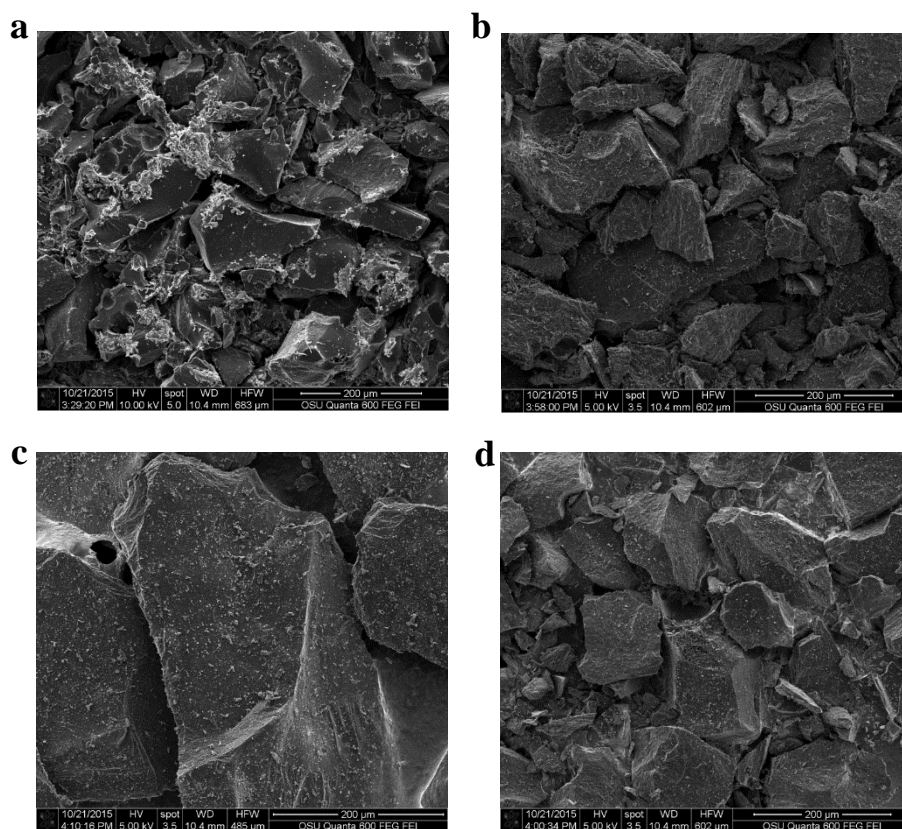


Figure 5.1 SEM images of all carbon samples. (a) HC, (b) P-HC, (c) S-HC and (d) B-HC.

All the dopant precursors are soluble in the sucrose aqueous solution, this helps achieve the atomic dispersion of dopants in the final products, as demonstrated in our previous

work.¹⁰ We aim at 5 wt.% of doping by assuming that the dopants are not volatile and the yield of sucrose carbonization is 25 wt%. We determined the doping levels by inductively coupled plasma optical emission spectrometry (ICP-OES) to be 3.0 wt.%, 3.0 wt.% and 0.1 wt.% for P-doped (P-HC), B-doped (B-HC) and S-doped (S-HC) hard carbon, respectively. Note that the S-doping level is significantly lower than the target amount of doping because sulfuric acid is most likely reduced into SO₂ gas during pyrolysis. Near-atomic level distribution of dopant was achieved, as shown in P-HC in our previous work.¹⁰ The densities for all carbons were measured based on Archimedes' principle, which are 1.60, 1.42, 1.50, and 1.49 g/cm³ for non-doped hard carbon (HC), P-HC, B-HC, and S-HC, respectively. The much lowered densities of all these carbons compared to graphite (2.11 g/cm³, our measured value) indicate larger d-spacing between graphenic layers or more enclosed nano-voids in the structures⁴⁰. All as-obtained HC, P-HC, B-HC and S-HC exhibit very low Brunauer-Emmett-Teller (BET) surface area of 8.5 m²/g, 7.3 m²/g, 8.0 m²/g and 5.2 m²/g, respectively. All these carbons consist of bulk particles, tens of microns large, as shown in the scanning electron microscope (SEM) images (Figure 5.1). The consistently low surface area and similar morphology of these carbons will facilitate a faithful comparison between their local structures and the corresponding electrochemical performance. Importantly, by pyrolysis treatment at 1100 °C, these carbon samples belong to the category of “conventional” hard carbon so that the mechanistic insights obtained on them can be employed to explain phenomena of the most hard carbon materials in the literature.

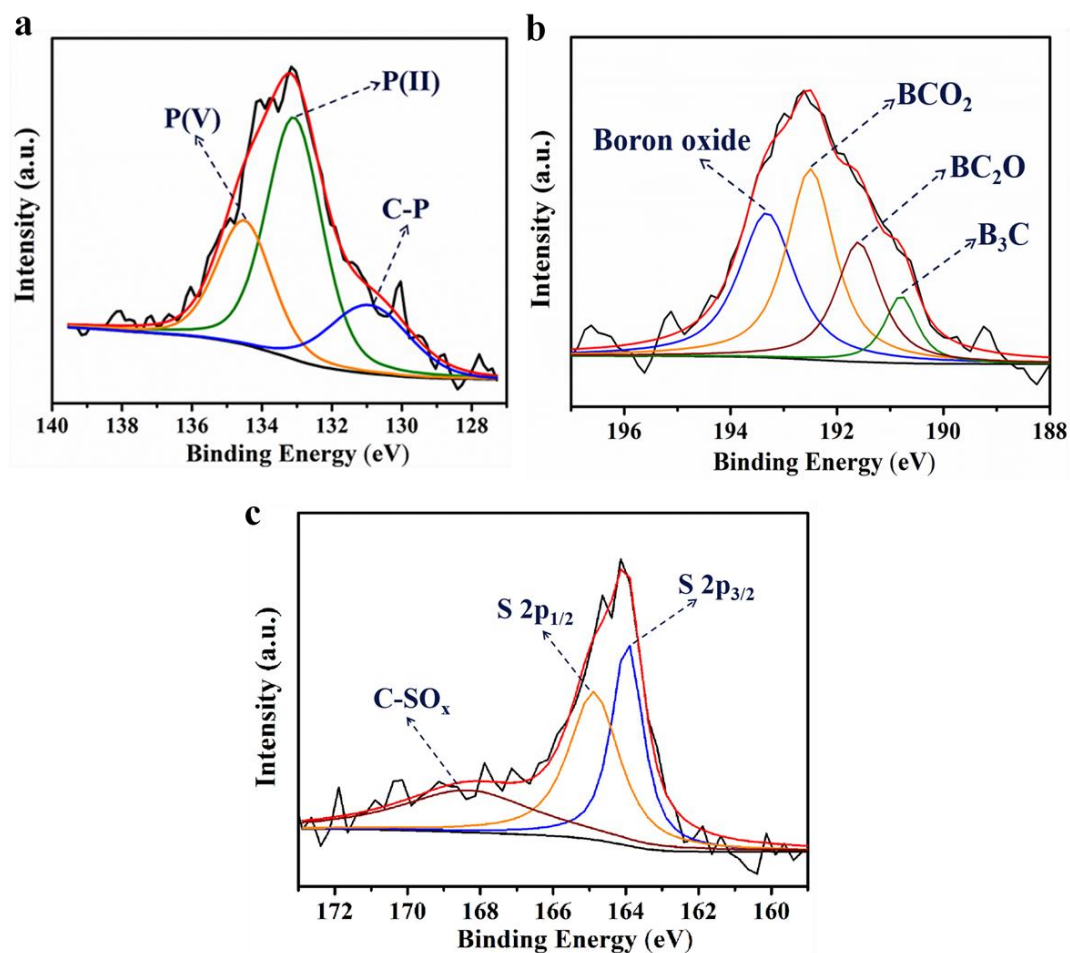


Figure 5.2 High resolution XPS spectra of all carbons. (a) P 2p of P-HC, (b) B 1s of B-HC and (c) S 2p of S-HC.

We investigated the oxidation states of the dopants by x-ray photoelectron spectroscopy (XPS) (Figure 5.2). None of the dopants became fully reduced to its elemental valance from their oxo-acid precursors. Phosphorus in P-HC occurs in P(V), P(II), and P-C bonds with its 2p signal deconvoluted into components at 134.5, 133.1 and 131.0 eV, respectively (Figure 5.2a).^{41, 42} As for S-HC, the sulfur 2p signal is deconvoluted into peaks at 168.3, 164.9 and 163.9 eV, attributed to C-SO_x, S 2p_{1/2} and S 2p_{3/2} of C-S-C,

respectively (Figure 5.2b).^{17, 43} For B-HC, boron may occur in the doped sample in boron oxide, BCO_2 , BC_2O and B_3C , as suggested by deconvoluted B_{1s} peaks at 193.3, 192.5, 191.6 and 190.8 eV, respectively (Figure 5.2c).⁴⁴

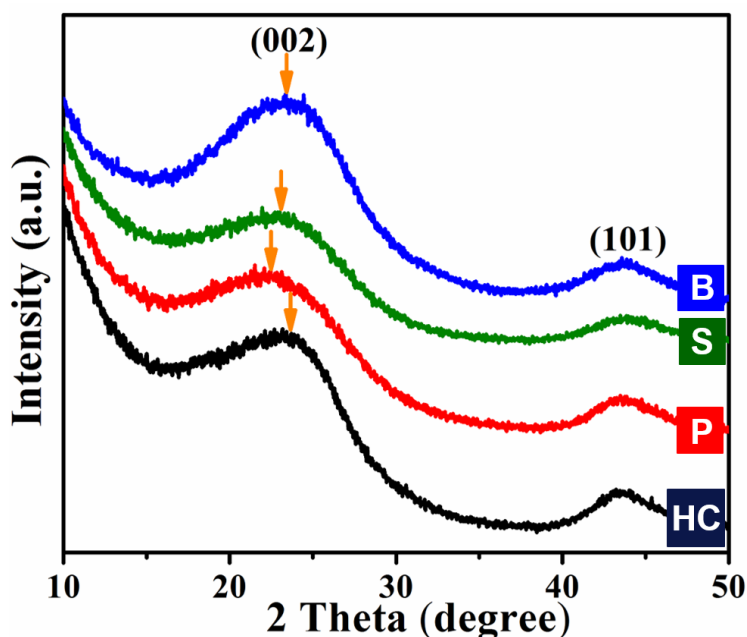


Figure 5.3 XRD studies of all carbons. After P- and S-doping, the (002) peak shifts to a lower angle, which indicates a larger d-spacing. However, B-doping barely shifts the peak.

The x-ray diffraction (XRD) results reveal the non-graphitic structure of carbons and confirm our hypothesis that P- and S-doping would increase the interlayer d-spacing, whereas the interlayer distance of B-HC stays nearly the same. The positions of (002) peaks determined by the PDXL software are at 23.6° , 22.5° , 23.2° , and 23.5° , indicating d-spacing values of 3.77 \AA , 3.95 \AA , 3.83 \AA and 3.78 \AA for HC, P-HC, S-HC, and B-HC, respectively (Figure 5.3). The error bar for these d-spacing values is $\sim \pm 0.01 \text{ \AA}$, related to the measurement setup. High-resolution TEM images demonstrate typical hard

carbon turbostratic structures, as shown in Figure 5.4. It seems that graphenic layers in P-HC are more curved than those in HC, while some graphenic layers in B-HC are longer and less curved than HC.

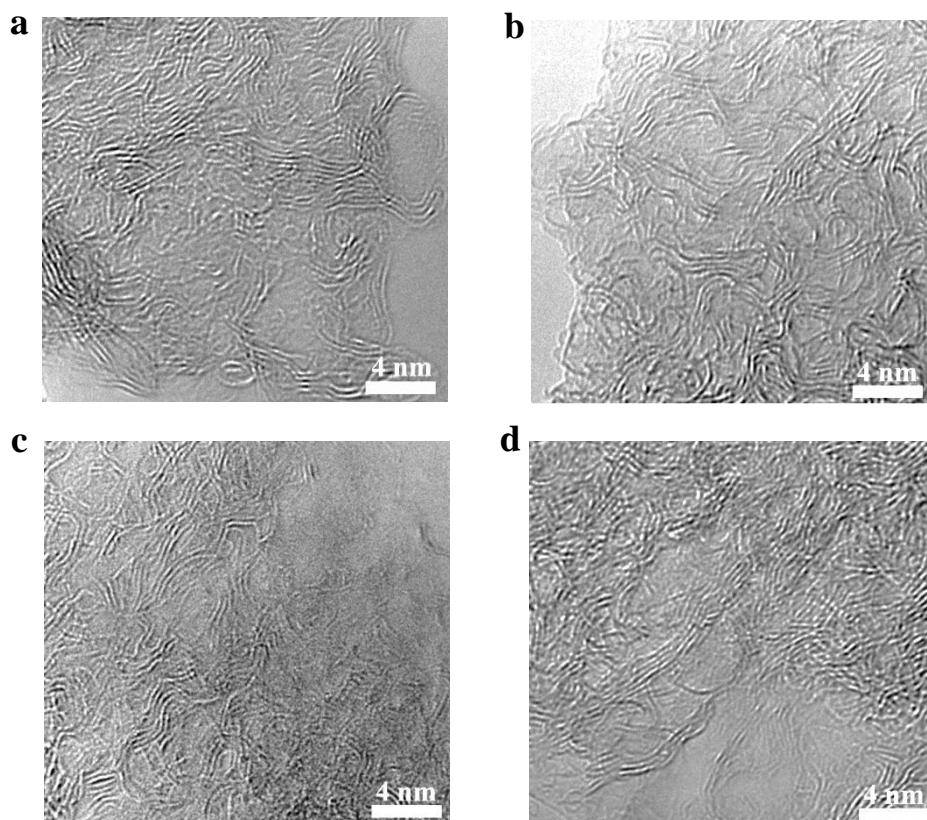


Figure 5.4 TEM images of all carbons. (a) HC, (b) P-HC, (c) S-HC and (d) B-HC. All carbons demonstrate a non-graphitic structure comprising curved graphenic layers, where the lines are from the edge-view of the graphenic layers.

Raman spectra can estimate the coherence lengths of graphenic domains along ab directions (L_a) according to the following equation:

$$L_a(nm) = (2.4 \cdot 10^{-10})\lambda_{nm}^4 \left(\frac{I_G}{I_D}\right) \quad (1)$$

where λ_{nm} is the laser wavelength: 514 nm, and I_G and I_D are intensity of G band and D band.⁴⁵ The D band at $\sim 1350 \text{ cm}^{-1}$ is attributed to the A_{1g} phonons of the breathing mode of C_6 rings activated by the existence of defects, while the G band at $\sim 1600 \text{ cm}^{-1}$ corresponds to the E_{2g} vibration of the sp^2 carbon atoms. To identify D and G bands accurately, two broad peaks in Raman spectra are deconvoluted into four Lorentzian peaks, as shown in Figure 5.5. With the above equation, HC, P-HC, S-HC and B-HC exhibit L_a values of 12.9, 12.1, 14.2 and 14.6 nm. P-HC exhibits the shortest coherence length of L_a , which indicates that graphenic layers in P-HC may be shorter or more curved, where the latter scenario is supported by the TEM imaging. Furthermore, the Raman results indicate that B-HC has the largest average domain size of graphenic layers, which corroborates the TEM results.

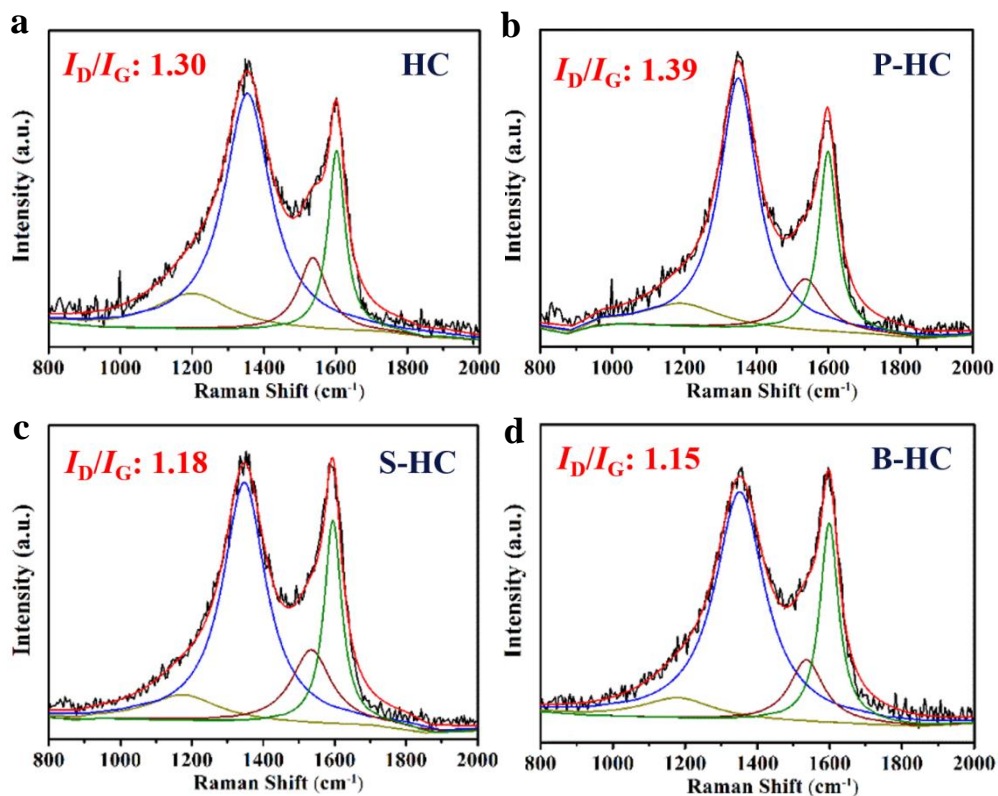


Figure 5.5 Raman spectra of different carbon samples, which are deconvoluted into four Lorentzian peaks: TPA (dark yellow), D (blue), A (wine) and G (green). (a) HC, (b) P-HC, (c) S-HC and (d) B-HC. The results of the ID/IG ratios suggest that P-HC exhibits the shortest coherence length along the ab planes, where B-HC has the longest, corroborating the XRD and TEM results.

It was extremely challenging to fully understand the local structures of amorphous carbon by conventional characterizations. Fortunately, recently, tremendous progress has been made with pair distribution function (PDF) studies associated with high-energy x-ray and neutron total scattering, which can help reveal the local structures of nanomaterials and amorphous carbon.⁴⁶⁻⁴⁸ In our prior studies, we determined local defect levels by neutron total scattering and PDF studies, where defects are correlated

to the sloping region of potential profiles.^{10, 15} To obtain the PDF results, a Fourier transform of the structure function $S(Q)$ is carried out with the following equation:

$$\frac{A}{4\pi} G(r) = A\rho[g(r) - 1] = \frac{1}{2\pi^2} \sum_0^{Q^{max}} QA[S(Q) - 1] \sin(QR) \Delta Q \quad (2)$$

where Q is the scattering vector, ρ is the atomic number density, $g(r)$ is the atomic pair distribution function, and A is a constant generated during normalization.⁴⁹ The $G(r)$ plots are simply a radial distribution map, where the peak positions (r) are the real space distances between an arbitrarily chosen central carbon atom and its neighbors averaged over all atoms of the sample. As shown in Figure 5.6a, the first three peaks are the intraring distances in C_6 (Figure 5.6b), and the first peak is the C-C bond length, 1.42 Å. The function $g(r)$ is the ratio of the average number of atoms found at the distance of r relative to the number of atoms that would be found in a completely disordered structure of the same density, and therefore, the amplitude for the first peak is related to coordination number. Boric acid (B^{11}) was used to prepare B-HC as the absorption cross section of B^{11} is only 0.0055, comparable to 0.0035 of carbon, whereas this value is 767 for the natural mixture of boron isotopes, which would significantly damp the amplitude of the collected data. By observing the change in peaks' area upon doping, it becomes clear that heteroatom doping causes changes in peak amplitude or conversely, defect concentration. Defects include the factors that disrupt the continuum of the graphenic honey comb structure.

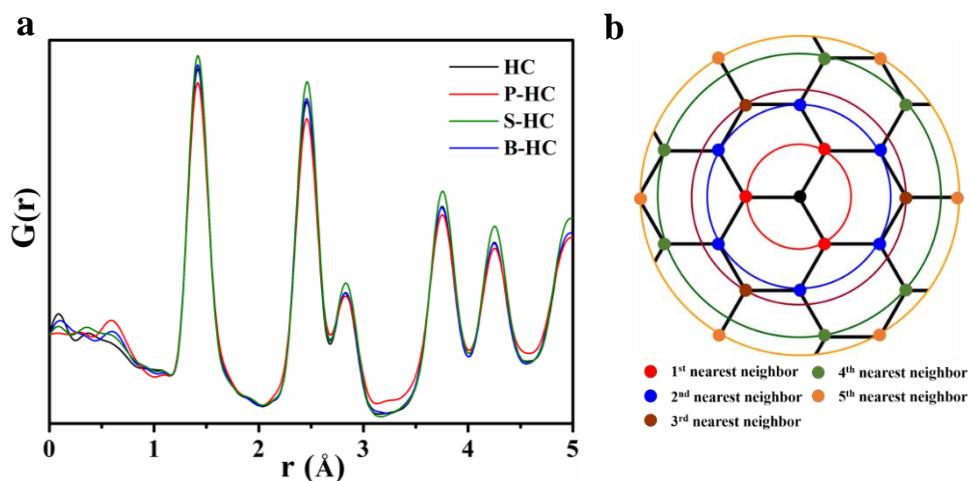


Figure 5.6 Neutron total scattering and PDF studies of carbons. (a) PDF within 5 Å from neutron total scattering of HC, P-HC, B-HC and S-HC. P-doping causes the local structure of carbon to be more defective, where S-doping slightly increases the degree of the local order. (b) Schematic local structure of graphene.

In PDF plots, S-HC exhibits higher amplitude of peaks than HC, which indicates less local defects. This is not surprising because H_2SO_4 is a carbonization agent, which enhances the formation of C_6 rings during sucrose pyrolysis. Plus, upon pyrolysis, H_2SO_4 decomposes to volatile gas species, *e.g.*, SO_2 , thus leading to a very low doping level of sulfur (0.1 wt.%) in the resulting carbon. It is quite intriguing that B-HC shares the similar peak amplitude as the un-doped carbon. It appears that the reduction of the boric acid precursor during boron doping does not result in more in-plane vacancies of the graphenic layers. As boron atoms can only form three bonds with the absence of strong Lewis bases, B-doping would retain well the graphenic nature of the doped carbon layers, which is consistent with the TEM and Raman results. Here, we should be cautious about the existence of in-plane doped-B and its impact on Na-ion storage. The B-doping process that does not generate more in-plane vacancies can still lead to a

profound impact on its Na-ion storage properties. The doped-B sites are, in fact, in-plane defect sites as the binding energies between the doped-B and inserted Na-ions are different compared to the pristine carbon sites, which will be discussed by the DFT simulation later in the article. P-HC exhibits the lowest peak amplitude, which indicates more defects or curvatures in the local structure. Because the doped PO_x species will not be coplanar with graphenic layers, thus inducing more curvatures, as corroborated by the TEM images and the shortest coherence length L_a among all samples, as indicated by the Raman results. It is possible that PO_x doping causes more structural vacancies as well.

To test our hypothesized Na-ion storage mechanism, we have obtained the desirable structural properties of hard carbon by heteroatom doping. First, through P- and S-doping, we have enlarged the inter-layer spacing inside the turbostratic nanodomains, which should enhance the plateau capacity. Second, P- and B-doping have introduced additional structural defects inside hard carbon, where the sloping capacity should be enlarged.

5.4.2 Electrochemical Behaviors of All Carbons

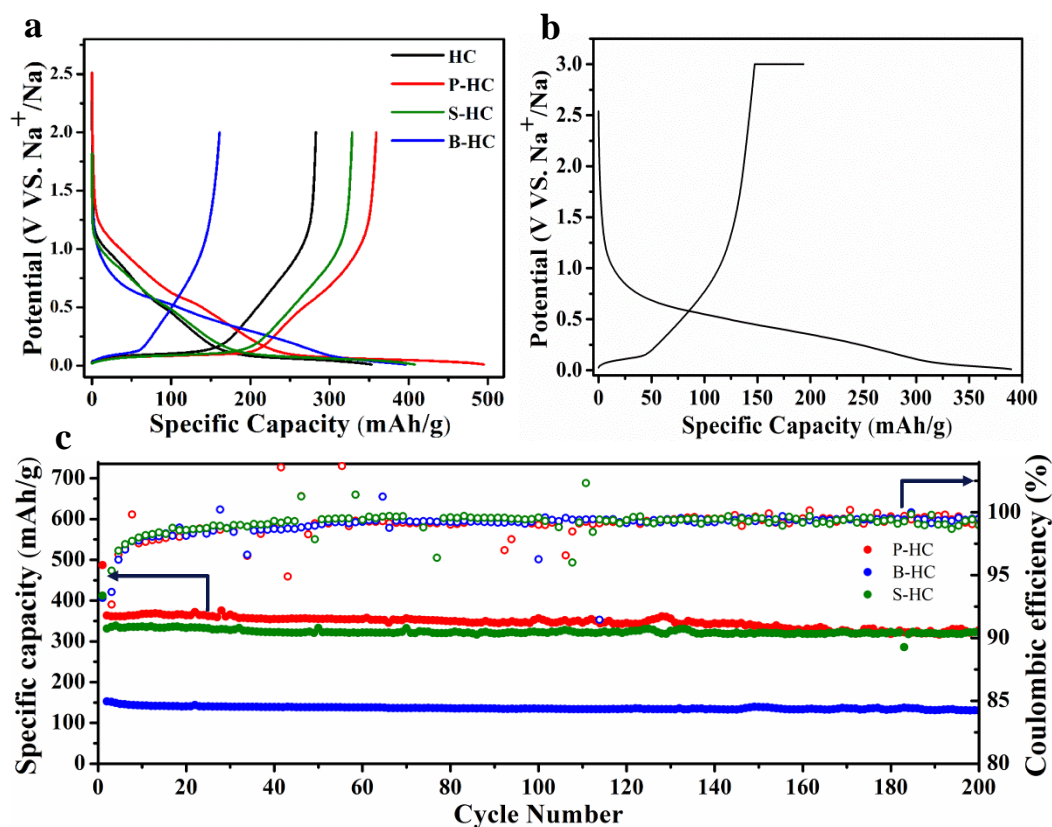


Figure 5.7 Electrochemical performance of hard carbons in C/Na half-cells. The potential is vs Na⁺/Na. (a) Galvanostatic sodiation/desodiation potential profiles of HC and doped hard carbons at a current rate of 20 mA/g. (b) Sodiation/desodiation potential profiles of B-HC at current rate of 20 mA/g by charging it to 3.0 V and holding the potential at 3.0 V for 30 h. (c) Cycling performance of doped carbons at a current density of 20 mA/g. All doped carbon materials are very stable in cycling performance.

Figure 5.7a and Table 5.1 provide the detailed slope/plateau capacity values, where we use the inflection point of the potential profiles to define the sloping and plateau regions: above the inflection point considered as the slope and below the point classified as the plateau. All doped carbons show quite stable cycling performance at a current density of 20 mA/g, where P-HC and S-HC exhibit a high capacity of 327 (91% retention) and 323 mAh/g (98% retention) even after 200 cycles (Figure 5.7c).

Table 5.1 Sodiation/desodiation capacities of HC and doped carbons and their capacities from plateau region and slope region.

First Cycle Electrode Capacity (mAh/g)	HC	P-HC	B-HC	S-HC
Total sodiation capacity	353	485	403	408
Total desodiation capacity	283	359	147	328
Sodiation capacity from plateau	175	240	99	213
Desodiation capacity from plateau	149	202	77	177
Sodiation capacity from slope	178	245	304	195
Desodiation capacity from slope	134	157	70	151

When we look at the plateau capacity of electrodes during the first sodiation, both P-HC and S-HC are superior to un-doped HC by exhibiting 240 and 213 mAh/g compared to 175 mAh/g of HC, and the plateau capacity for all carbon samples is relatively reversible. The capacity values confirm that a larger d-spacing due to hypervalent S- and P-doping does increase the plateau capacity. This can be well rationalized because it would be energetically more favorable for Na-ions to be inserted between more dilated graphene sheets. Note that Na-ions are, indeed, larger than the ideal fit size to be accommodated by the graphitic galleries even when they are turbostratic and dilated to some degree, thus to squeeze Na-ions between carbon layers would certainly involve a penalty enthalpy change. It is this penalty enthalpy change together with the weak binding energy between the defect-free graphene layers and Na-ions (atoms) that causes the extremely low capacity of Na-ion storage by graphite. Therefore, a larger average

d-spacing separating these graphenic layers will allow more Na-ions to be inserted before the cutoff potential of Na-plating is reached. However, it is quite interesting that B-HC exhibits an extremely small capacity from its low-potential plateau.

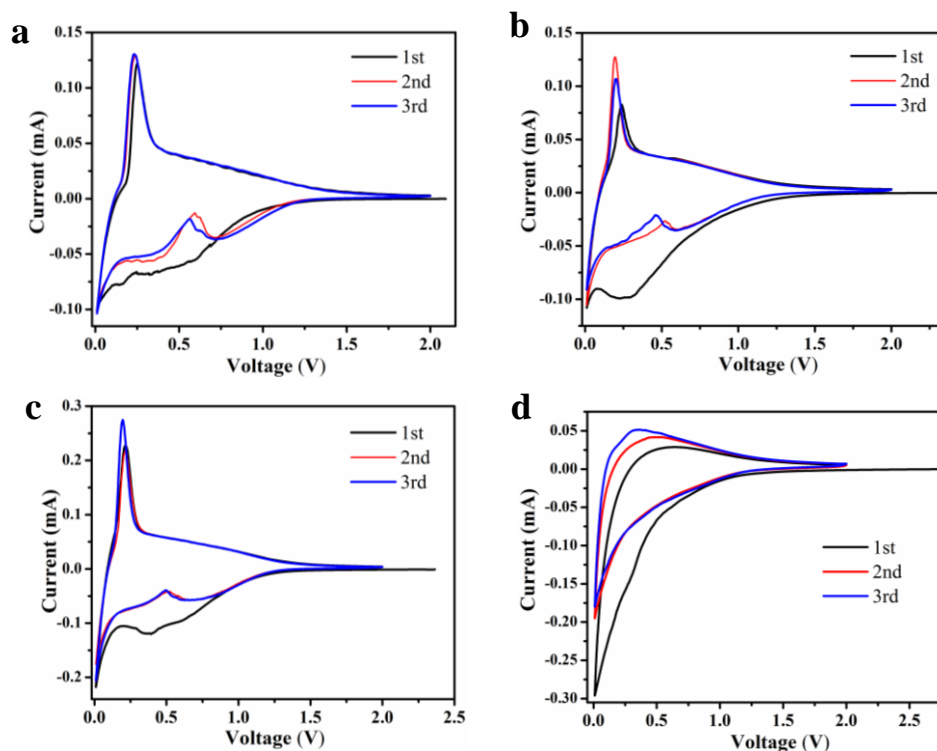


Figure 5.8 CV curves of various carbon anodes at a scan rate of 0.1 mV/s in a potential range of 0.01-2 V. (a) HC, (b) P-HC, (c) S-HC and (d) B-HC.

Looking at the sloping region during the first sodiation, B-HC and P-HC exhibit capacity values of 304 mAh/g and 245 mAh/g, respectively, compared to 178 mAh/g of the un-doped HC. Such high sloping capacity values during the first sodiation can be explained by the causality of Na/carbon-defect binding for P-HC; however, it is puzzling for B-HC because B-HC does not contain more graphenic vacancies as the PDF results revealed. Furthermore, B-HC is not likely to form a great deal of SEI due

to its very modest specific surface area of $8.0 \text{ m}^2/\text{g}$. The really shocking observation is from the first desodiation, where P-HC and B-HC generate sloping capacity values of 157 and 70 mAh/g, respectively, vs 134 mAh/g of HC. Both P-HC and B-HC suffer less coulombic efficiency for the slope region: 64% and 23% compared to 75% of HC. At this point, it is even more intriguing why B-HC's sodiation is so irreversible as we have excluded the possibility of massive SEI formation.²⁷ Cyclic voltammetry (CV) results confirm the same extent of irreversible sodiation in P-HC and B-HC electrodes (Figure 5.8). In particular, the CV curves of B-HC look completely different from the other doped and un-doped hard carbon samples, where instead of exhibiting a sharp desodiation peak, the anodic scan leads to a broad bump-like peak, thus revealing the difficulty of removing Na-ions from B-HC's internal structure.

5.4.3 Computational Studies of The Na Binding

To further understand the structure-capacity correlation in hard carbon, we used DFT calculations to determine the electronic structure of sodium binding at various structural sites: idealized dopants, vacancies in contrast to ideal graphene sheet. Even though several pure computational studies on the energetics of sodium binding with doped graphene had been reported,^{29, 50} this article focuses on understanding of Na-ion storage in hard carbon anode, where due to the similarity at the local atomic scale, we employ nanosheets of graphene for the computational studies. We pay more attention on a comparative study with the expectation that the same trends in the electronic structure and energetics will carry over to the more complex misaligned, multilayered,

turbostratic structures of hard carbon. Calculations were performed using the Vienna ab-initio Simulation Package (VASP) using dispersion corrected exchange correlation functionals. First, the binding of Na to graphene in the vicinity of B and P substitutional defects were studied. The sodiation energy was calculated using the equation:

$$E_{bnd}(x) = \frac{1}{n_{Na}} (E_{sub+Na}(x) - E_{sub} - n_{Na}E_{Na-BCC}) \quad (3)$$

$$E_{bnd}(x) = \int_0^x eV(x') dx' = \int_0^{q/e} V(q') dq' \quad (4)$$

where E_{sub+Na} is the energy of the relaxed carbon substrate-Na system, E_{sub} is the energy of the carbon substrate, and E_{Na-BCC} is the per atom cohesive energy of BCC sodium metal. These calculations were performed on a 4x4 supercell of graphene so that the dopant concentration obtained from a single substitutional defect was comparable to the experimentally measured dopant concentration. The quantity n_{Na} is the number of Na atoms in a calculation and x is the concentration of Na to substrate atoms. Ignoring entropic contributions, the binding energy computed in this way can be related to the discharge voltage in the C/Na half-cell environment with the expression: the integral above, where q is the stored charge.

The Na atom has a positive (unfavorable) binding energy on the pristine graphene sheet, while it has a negative binding energy with both the P-doped sheet, as well as the B-doped sheet. Utilizing a 4x4 sheet with a single heteroatom dopant implies that the sheet

formulas are $C_{31}P$ and $C_{31}B$, which gives an atomic concentration percentage of 3.2% for the heteroatoms.

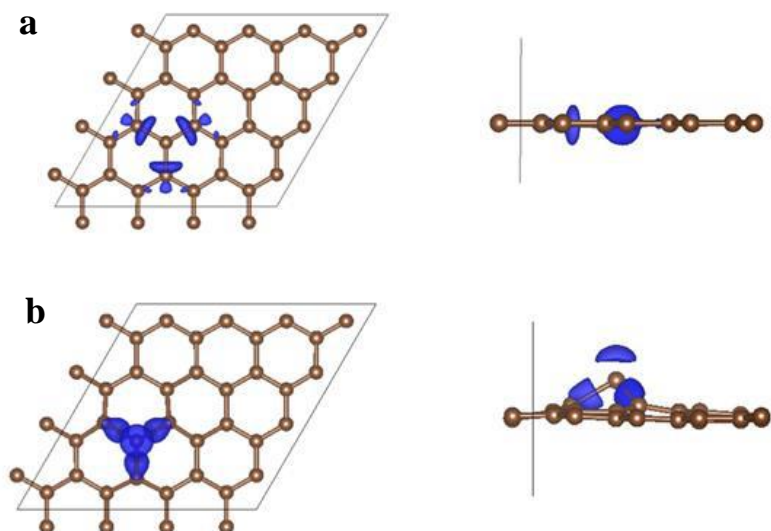


Figure 5.9 Comparison of charge distribution from (a) B-doped graphene sheet vs a pristine graphene sheet. (b) P-doped graphene sheet vs a pristine graphene sheet. The blue region indicates a greater negative charge present in the doped graphene sheet, as opposed to the undoped one. This demonstrates the electron donating nature of the heteroatom.

Table 5.2 Binding energy of Na-ions to pristine and doped graphene sheets.

Binding Energy (eV)		
Pristine Graphene	P-doped graphene	B-doped graphene
0.529	-0.325	-0.916

Though not representative of the actual hard carbon structure, the data suggest a trend that can be extrapolated to the experimental conditions. Addition of heteroatoms in the plane of the graphene leads to favorable binding energies over that of pristine graphene,

as shown in Table 5.2. In the case of the B-doped graphene, the increase in binding energy is much greater than that of the P-doped graphene. If we were to translate the binding energies to voltages, the sodiation voltage on a B-doped graphene sheet would be ~ 0.92 V vs Na^+/Na , while the sodiation voltage for a P-doped sheet be of only ~ 0.32 V. With this data, we conclude that, since boron acts as a p-type dopant, the system more readily accepts an electron from the sodium atom, thus leading to greater ionic interaction, and as a result, stronger binding. Meanwhile, the phosphorous being a n-type dopant, would less readily accept an electron from the sodium, thus weakening its binding energy. However, when the Bader charges for the dopant atoms are obtained, B-atom has a charge of B^{3+} , while the phosphorous has one of $\text{P}^{3.43+}$. This means that in both cases, three or more electrons are transferred to the neighboring carbon atoms on the graphene sheet (Figure 5.9). As a result, there is a stronger interaction between the sodium atom and the graphene sheet in the area around the heteroatom, but not the heteroatom itself (Figure 5.10). Since the heteroatom is positively charged, it is expected to repel the sodium atom, which is in fact seen: the sodium atom on the phosphorous doped graphene sheet is located 2.81 \AA from the P-atom, while in the sodium atom in the boron doped graphene sheet is located 2.57 \AA from the B-atom. The lower repulsion from the boron allows the sodium atom to get closer to the negatively charged graphene sheet, thus enhancing the ionic interactions. Furthermore, the size of the P-atom causes the graphene sheet to buckle with more curvature, which is consistent with our experimental results.

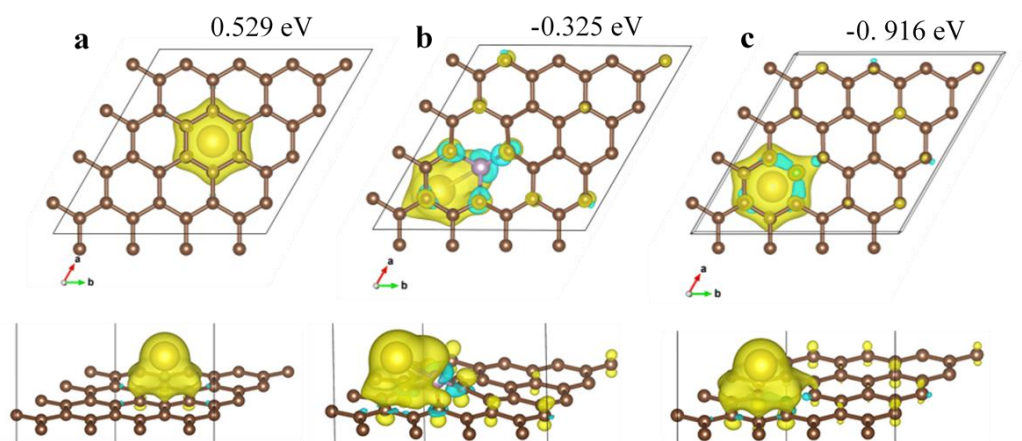


Figure 5.10 Charge distribution plots of different graphene/Na systems simulated in VASP with the binding energies of sodium ions shown. The blue regions of the charge distribution represent a negative charge, while the yellow regions represent positive charges. (a) Pristine graphene. (b) P-doped graphene. (c) B-doped graphene.

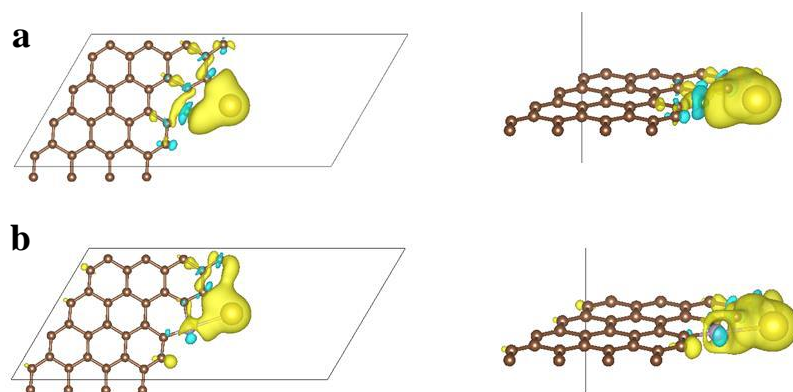


Figure 5.11 Charge distribution plots of different (a) Edge doped BC₂. (b) Edge doped PC₂.

Thus far, these simulations only allow us to ascertain what happens in the event that the heteroatom is bonded in-plane with the graphene sheet. However, this is not the only configuration it can take up in our system: there is the possibility of bonding at edge

sites in the graphene domains, as well as the presence of oxygen and hydrogen atoms. Thus, we pushed forward and simulated those configurations as well. In the case of a heteroatom being bonded of a graphene edge, thus forming a XC_2 bond, the equivalent voltage for the boron system was of 1.76 V, while it was 1.96 V for the phosphorous system (Figure 5.11). Looking at the Bader charges for the heteroatoms, the boron was found to be in a B^{3+} state, while the phosphorous was in a $P^{2.75+}$ oxidation. This supports our previous findings that electrons are transferred from the heteroatom to the graphene system. However, in this case, as there is less degree of charge transfer on behalf of the phosphorus, the binding with the Na atom is stronger, as it is not repelled as much.

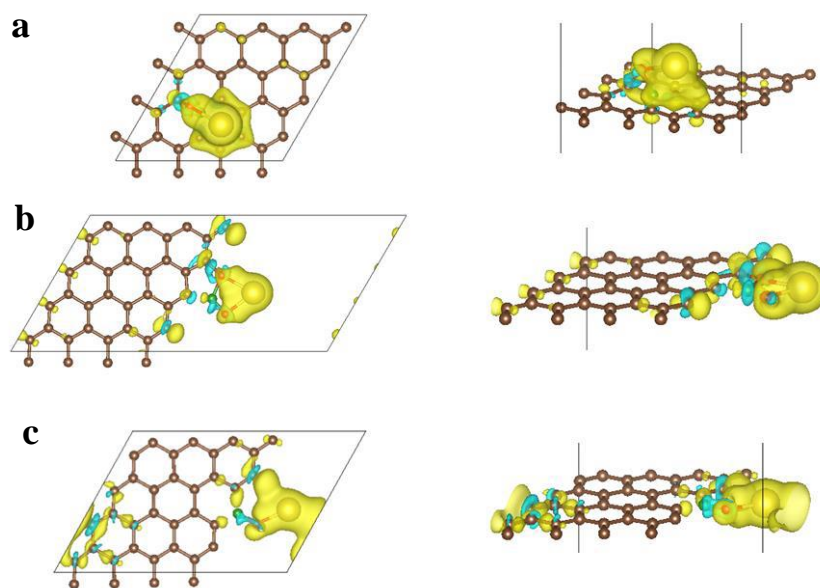


Figure 5.12 Charge distribution plots of (a) In-plane BC_3O . (b) Edge doped BCO_2 . (c) Edge BC_2O .

Addition of oxygen atoms to the system in various configurations was also performed, though a clear pattern in those results was harder to ascertain. In the case of the boron doping, addition of oxygen and a boron on the plane, and one on an edge site resulted in stronger binding energies, with the increase in binding energy being more pronounced at the edge site. An oxygen atom on the in-plane boron increased the voltage to 1.37 V, while oxygen groups on the edge boron increased the voltage to 2.52 V, with that voltage being able to be increased to 3.65 V if the unit cell was shrunk to a small enough size, as to induce periodic binding (Figure 5.12). The same configuration with oxygen atoms in the phosphorous doping yielded voltages of 1.66, 1.66, and 3.56 V with the smaller unit cell (Figure 5.13). When looking at the Bader charges for this system, the boron stayed at B^{3+} , while the phosphorous was at P^{5+} .

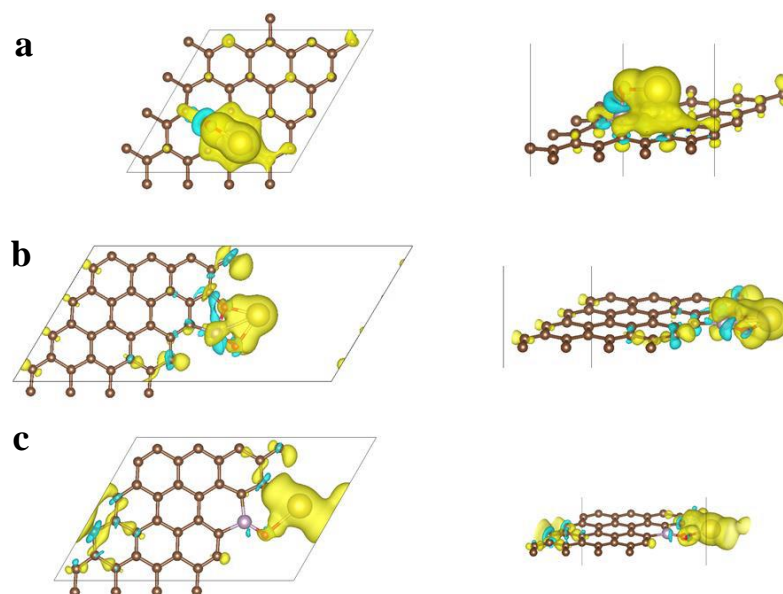


Figure 5.13 Charge distribution plots of (a) In-plane PC_3O . (b) Edge doped PCO_2 . (c) Edge PC_2O .

Since the oxidation P(II) was heavily featured in the XPS data, but the oxidation due to the addition of oxygen was entirely suggestive of P(V) oxidation, we performed additional simulation with OH groups, with the thought that the H would suppress the electron withdrawing tendencies of the oxygen functional group on the phosphorous. Converged simulations show that charges of $P^{2.64+}$ and $P^{3.37+}$, with voltages of 2.62 and 2.69 V, respectively (Figure 5.14). It also must be noted that both the phosphorous atoms were present at edge sites on the graphene sheet. Aside from the increased voltage in Na atom binding, these simulations also show that, while not the P(II) illustrated in the XPS results, the addition of H to carbonyl groups attenuates their electron withdrawing power.

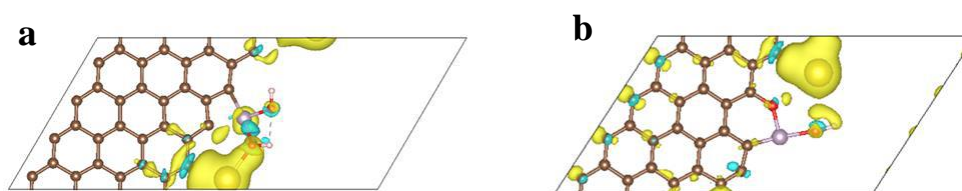


Figure 5.14 Charge distribution plots of (a) Edge doped $PC(OH)_2$. (b) Edge doped $PCO(OH)$.

Overall, there are a few takeaways from these simulations in helping us better understand the impact of heteroatom addition to graphene structures. First, the heteroatoms act as electron donors to the graphene sheet, while themselves acting at positively charges. This leads to stronger ionic bonding between the sodium atom and the graphene sheet, and is the strongest in boron. Additionally, the presence of oxygen in the system also increase the overall voltage of the sodium atom storage.

Correlating the simulation data to the first-cycle sodiation profiles of the B-HC and P-HC, we see a lot of similarities: the B-HC profile has a much more pronounced slope, and on average has a much higher voltage than the P-HC profile. Considering that Na atoms bind more strongly, and thus at higher voltages, to boron heteroatom, along with the fact that B-HC also had a higher oxygen concentration, which is also associated with higher voltages, such profiles match up well with the DFT results, and help to explain why the B-HC has a much longer slope than the P-HC.

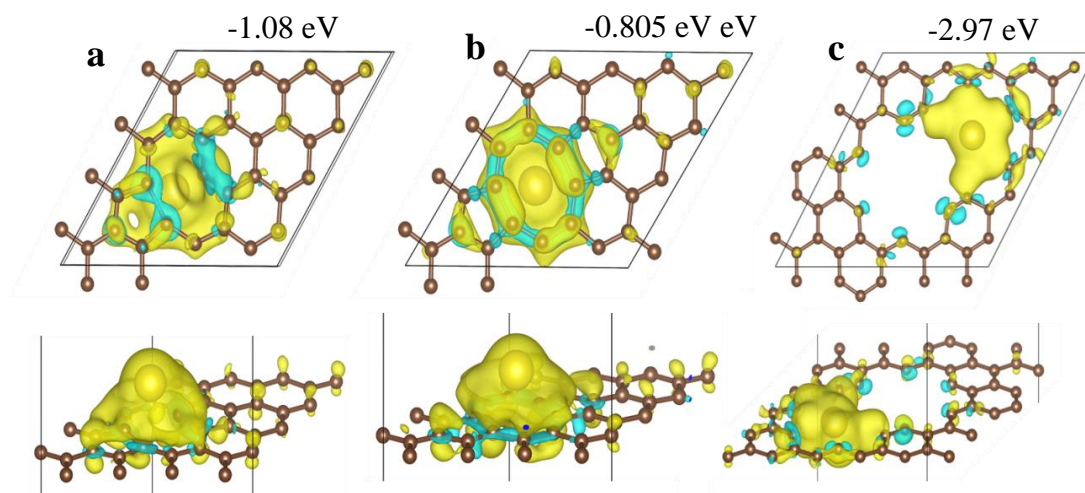


Figure 5.15 Charge distribution plots of different graphene/Na systems simulated in VASP. The blue regions of the charge distribution represent a negative charge, while the yellow regions represent positive charges. **(a)** Monovacancy graphene. **(b)** Divacancy graphene. **(c)** A large in-plane defect. With both monovacancy and divacancy, the Na-ion hovers on the surface of graphene layer; whereas in the case of the large vacancy, Na-ion is cuddled in the void.

Table 5.3 Binding energy of Na-ions to different defective graphene sheets.

Binding Energy (eV)		
Monovacancy	Divacancy	large-vacancy defect
-1.08	-0.805	-2.97

Though helpful, these initial results are to be taken with caution, as they make the assumption that the heteroatoms are only bonded with carbon atoms. However, there is another structural feature of the carbon material whose effect on Na-ion storage we can also evaluate: the presence of vacancies. From the PDF results, we know that P-HC is of a higher defect concentration than HC. When simulating a monovacancy, divacancy and a large-vacancy defect, where we define them all as in-plane defects, we see that the binding energy is very favorable, especially in the base of the large-vacancy defect (Table 5.3). From the charge density plots (Figure 5.15), we see that negative charges gather at defect sp^2 sites, thereby acting as favorable binding locations for Na atoms. This is especially true in the case of the monovacancy defect and the large-vacancy defect, which show strong regions of charge at sp -bonded carbons, which are highly favorable for binding with Na atoms. This may explain why with more defects P-HC exhibits an enhanced presence of sloping capacity. Cohn et al. recently reported the function of carbon nanoparticles coated on metal current collector as nucleation sites for Na-metal plating.⁵¹ The evenly distributed doping sites and their higher binding energy with sodium ions would reduce the sodium plating barrier and decrease the overpotential. This high reversible capacity and good cycling performance of P-HC and S-HC suggest that these doped carbons are very promising to be used as a carbon nucleation layer for sodium plating.

Note that different dopants are, indeed, of various numbers of doping sites; however, it is clear that different identities of dopants generate a stark contrast in their impacts on

the Na-ion storage performance of hard carbon anodes. Such impacts may come from the changed carbon structures, i.e, with more vacancy defects, or from the dopant themselves as heteroatom defects. For example, in terms of the sloping region, P-doping introduces more carbon vacancy defects to graphenic layers, as revealed by neutron total scattering/PDF, which rationalizes its higher sloping capacity; however, B-doping does not cause more carbon vacancy defects according to Raman and PDF results, but B-HC exhibits the highest sloping capacity in its first sodiation. This can only be understood by the fact that the doped Boron atoms themselves are strong Na-binding “defects”, as revealed by DFT studies, and the binding energy between the doped B sites and Na-ions are comparable to binding with carbon vacancy sites. This explains why both P-HC and B-HC show higher sloping capacity than un-doped HC, where the trend is that sites with higher binding energy values would contribute to the sloping capacity.

Here, we attempt to explain the poor reversibility of B-HC during the first cycle. First, B-HC exhibits a very limited low-potential plateau capacity of 99 mAh/g out of 403 mAh/g for the overall sodiation. This is in sharp contrast to 175, 240 and 213 mAh/g for HC, P-HC and S-HC. When scrutinizing the TEM imaging results, one cannot easily differentiate that of B-HC from the TEM images of other carbons because they all contain turbostratic stacking of curved graphenic layers. Considering its very large sodiation capacity of 403 mAh/g and an expected minimal SEI formation due to the low specific surface area, “intercalation” of Na-ions must have taken place between the B-doped graphenic layers during the first sodiation. Considering the high binding energy

between the doped B and the inserted Na-ions, we hypothesize that the normally low-potential plateau for other carbon samples is replaced by the high-binding-energy “intercalation” in B-HC. However, this high-binding-energy intercalation traps Na-ions, causing the high irreversible capacity in the first cycle. The basic rationale for such trapping is that the motion of Na-ions through the “sticky” bi-layers in the turbostratic domains becomes very restricted due to the high binding energy, which traps the Na-ions.

To prove the irreversibility is of the energetic causality, we apply a large voltage bias on the C/Na half-cells to see whether a larger extent of desodiation can be forced to take place. When the half-cell was held at a constant voltage of 3.0 V for 30 h, an additional capacity of 40 mAh/g was recovered (Figure 5.7b). It is expected that applying an even higher cell voltage can extract more desodiation capacity. This suggests that the B-HC anode can reversibly store Na atoms, but it does so very strongly. Thus, simply desodiating the anode up to a cut-off potential of 2.0 V is not sufficiently high to fully remove all of the inserted Na atoms. This behavior is consistent with the high binding energies from the in-plane boron in turbostratic domains.

5.5 Conclusion

In conclusion, *via* well-controlled syntheses, comprehensive structural characterization and first principles DFT studies, we provide in-depth insights on the correlation between the local structure of hard carbon and the corresponding capacity performance. We

confirm the linkage between high-energy binding with Na-ions and the sloping region of potential profiles, particularly for the first sodiation. We also confirm the favorable impacts of larger interlayer spacing between graphenic sheets on extending the sodium storage capacity from the low-potential plateau. We employed B-doping to elucidate that high-energy in-plane “defect” sites inside turbostratic nanodomains can cause a large irreversible capacity in the first cycle. It means that albeit B-doping does not generate more in-plane carbon vacancies, if there existed in-plane vacancies in other hard carbon materials that bind Na-ion strongly, it will affect the first-cycle reversibility as well. Overall, we elucidate the Na-ion storage mechanism for hard carbon as an NIB anode, and we provide the design principle as such that the ideal hard carbon anode should be a low surface area ensemble of dilated turbostratic nanodomains with more curvatures or more non-in-plane high-energy defects. We believe that these fundamental insights into Na-ion storage mechanisms will guide community to steer the development and optimization of hard carbon anodes and as such will hasten commercialization of high capacity Na-ion batteries.

5.6 References

- (1) Xu, Y.; Wei, Q.; Xu, C.; Li, Q.; An, Q.; Zhang, P.; Sheng, J.; Zhou, L.; Mai, L. Layer-by-Layer $\text{Na}_3\text{V}_2(\text{PO}_4)_3$ Embedded in Reduced Graphene Oxide as Superior Rate and Ultralong-Life Sodium-Ion Battery Cathode. *Adv. Energy Mater.* **2016**, *6*, 1600389.
- (2) Fang, Y.; Xiao, L.; Ai, X.; Cao, Y.; Yang, H. Hierarchical Carbon Framework Wrapped $\text{Na}_3\text{V}_2(\text{PO}_4)_3$ as a Superior High-Rate and Extended Lifespan Cathode for Sodium-Ion Batteries. *Adv. Mater.* **2015**, *27*, 5895-5900.
- (3) Mu, L.; Xu, S.; Li, Y.; Hu, Y. S.; Li, H.; Chen, L.; Huang, X. Prototype Sodium-Ion Batteries Using an Air-Stable and Co/Ni-Free O3-Layered Metal Oxide Cathode. *Adv. Mater.* **2015**, *27*, 6928-6933.

- (4) Sathiya, M.; Hemalatha, K.; Ramesha, K.; Tarascon, J.-M.; Prakash, A. Synthesis, structure, and electrochemical properties of the layered sodium insertion cathode material: $\text{NaNi}_{1/3}\text{Mn}_{1/3}\text{Co}_{1/3}\text{O}_2$. *Chem. Mater.* **2012**, *24*, 1846-1853.
- (5) Jian, Z.; Zhao, L.; Pan, H.; Hu, Y.-S.; Li, H.; Chen, W.; Chen, L. Carbon coated $\text{Na}_3\text{V}_2(\text{PO}_4)_3$ as novel electrode material for sodium ion batteries. *Electrochem. Commun.* **2012**, *14*, 86-89.
- (6) Jache, B.; Adelhelm, P. Use of Graphite as a Highly Reversible Electrode with Superior Cycle Life for Sodium-Ion Batteries by Making Use of Co-Intercalation Phenomena. *Angew. Chem. Int. Ed.* **2014**, *53*, 10169-10173.
- (7) Wen, Y.; He, K.; Zhu, Y.; Han, F.; Xu, Y.; Matsuda, I.; Ishii, Y.; Cumings, J.; Wang, C. Expanded graphite as superior anode for sodium-ion batteries. *Nat. Commun.* **2014**, *5*, 4033.
- (8) Franklin, R. E. Crystallite growth in graphitizing and nongraphitizing carbons. *Proc. R. Soc. London, Ser. A* **1951**, *209*, 196-218.
- (9) Stevens, D.; Dahn, J. High Capacity Anode Materials for Rechargeable Sodium-Ion Batteries. *J. Electrochem. Soc.* **2000**, *147*, 1271-1273.
- (10) Li, Z.; Ma, L.; Surta, T. W.; Bommier, C.; Jian, Z.; Xing, Z.; Stickle, W. F.; Dolgos, M.; Amine, K.; Lu, J. High Capacity of Hard Carbon Anode in Na-Ion Batteries Unlocked by PO_x Doping. *ACS Energy Lett.* **2016**, *1*, 395-401.
- (11) Ding, J.; Wang, H.; Li, Z.; Kohandehghan, A.; Cui, K.; Xu, Z.; Zahiri, B.; Tan, X.; Lotfabad, E. M.; Olsen, B. C. Carbon nanosheet frameworks derived from peat moss as high performance sodium ion battery anodes. *ACS Nano* **2013**, *7*, 11004-11015.
- (12) Li, Y.; Hu, Y. S.; Titirici, M. M.; Chen, L.; Huang, X. Hard Carbon Microtubes Made from Renewable Cotton as High-Performance Anode Material for Sodium-Ion Batteries. *Adv. Energy Mater.* **2016**, *1*, 395-401.
- (13) Shen, F.; Luo, W.; Dai, J.; Yao, Y.; Zhu, M.; Hitz, E.; Tang, Y.; Chen, Y.; Sprenkle, V. L.; Li, X., et al. Ultra-Thick, Low-Tortuosity, and Mesoporous Wood Carbon Anode for High-Performance Sodium-Ion Batteries. *Adv. Energy Mater.* **2016**, *6*, 1600377.
- (14) Lotfabad, E. M.; Ding, J.; Cui, K.; Kohandehghan, A.; Kalisvaart, W. P.; Hazelton, M.; Mitlin, D. High-density sodium and lithium ion battery anodes from banana peels. *ACS Nano* **2014**, *8*, 7115-7129.
- (15) Bommier, C.; Surta, T. W.; Dolgos, M.; Ji, X. New mechanistic insights on Na-ion storage in nongraphitizable carbon. *Nano Lett.* **2015**, *15*, 5888-5892.
- (16) Komaba, S.; Murata, W.; Ishikawa, T.; Yabuuchi, N.; Ozeki, T.; Nakayama, T.; Ogata, A.; Gotoh, K.; Fujiwara, K. Electrochemical Na insertion and solid electrolyte interphase for hard-carbon electrodes and application to Na-Ion batteries. *Adv. Funct. Mater.* **2011**, *21*, 3859-3867.

- (17) Qie, L.; Chen, W.; Xiong, X.; Hu, C.; Zou, F.; Hu, P.; Huang, Y. Sulfur-Doped Carbon with Enlarged Interlayer Distance as a High-Performance Anode Material for Sodium-Ion Batteries. *Adv. Sci.* **2015**, *2*, 1500195.
- (18) Li, W.; Zhou, M.; Li, H.; Wang, K.; Cheng, S.; Jiang, K. A high performance sulfur-doped disordered carbon anode for sodium ion batteries. *Energy Environ. Sci.* **2015**, *8*, 2916-2921.
- (19) Yang, F.; Zhang, Z.; Du, K.; Zhao, X.; Chen, W.; Lai, Y.; Li, J. Dopamine derived nitrogen-doped carbon sheets as anode materials for high-performance sodium ion batteries. *Carbon* **2015**, *91*, 88-95.
- (20) Wang, P.; Qiao, B.; Du, Y.; Li, Y.; Zhou, X.; Dai, Z.; Bao, J. Fluorine-Doped Carbon Particles Derived from Lotus Petioles as High-Performance Anode Materials for Sodium-Ion Batteries. *J. Phys. Chem. C* **2015**, *119*, 21336-21344.
- (21) Xu, D.; Chen, C.; Xie, J.; Zhang, B.; Miao, L.; Cai, J.; Huang, Y.; Zhang, L. A Hierarchical N/S-Codoped Carbon Anode Fabricated Facilely from Cellulose/Polyaniline Microspheres for High-Performance Sodium-Ion Batteries. *Adv. Energy Mater.* **2016**, *6*, 1501929.
- (22) Li, Y.; Wang, Z.; Li, L.; Peng, S.; Zhang, L.; Srinivasan, M.; Ramakrishna, S. Preparation of nitrogen-and phosphorous co-doped carbon microspheres and their superior performance as anode in sodium-ion batteries. *Carbon* **2016**, *99*, 556-563.
- (23) Ruan, B.; Wang, J.; Shi, D.; Xu, Y.; Chou, S.; Liu, H.; Wang, J. A phosphorus/N-doped carbon nanofiber composite as an anode material for sodium-ion batteries. *J. Mater. Chem. A* **2015**, *3*, 19011-19017.
- (24) Zhu, J.; Chen, C.; Lu, Y.; Ge, Y.; Jiang, H.; Fu, K.; Zhang, X. Nitrogen-doped carbon nanofibers derived from polyacrylonitrile for use as anode material in sodium-ion batteries. *Carbon* **2015**, *94*, 189-195.
- (25) Yang, T.; Qian, T.; Wang, M.; Shen, X.; Xu, N.; Sun, Z.; Yan, C. A Sustainable Route from Biomass Byproduct Okara to High Content Nitrogen-Doped Carbon Sheets for Efficient Sodium Ion Batteries. *Adv. Mater.* **2016**, *28*, 539-545.
- (26) Hou, H.; Shao, L.; Zhang, Y.; Zou, G.; Chen, J.; Ji, X. Large-Area Carbon Nanosheets Doped with Phosphorus: A High-Performance Anode Material for Sodium-Ion Batteries. *Adv. Sci.* **2016**, *4*, 1600243.
- (27) Bommier, C.; Luo, W.; Gao, W.-Y.; Greaney, A.; Ma, S.; Ji, X. Predicting capacity of hard carbon anodes in sodium-ion batteries using porosity measurements. *Carbon* **2014**, *76*, 165-174.
- (28) Luo, W.; Bommier, C.; Jian, Z.; Li, X.; Carter, R.; Vail, S.; Lu, Y.; Lee, J.-J.; Ji, X. Low-surface-area hard carbon anode for Na-ion batteries via graphene oxide as a dehydration agent. *ACS Appl. Mater. Interfaces* **2015**, *7*, 2626-2631.
- (29) Ling, C.; Mizuno, F. Boron-doped graphene as a promising anode for Na-ion batteries. *Phys. Chem. Chem. Phys.* **2014**, *16*, 10419-10424.

- (30) Kresse, G.; Furthmüller, J. Efficient iterative schemes for ab initio total-energy calculations using a plane-wave basis set. *Phys. Rev. B* **1996**, *54*, 11169-11186.
- (31) Kresse, G.; Hafner, J. Ab initio molecular-dynamics simulation of the liquid-metal–amorphous-semiconductor transition in germanium. *Phys. Rev. B* **1994**, *49*, 14251-14269.
- (32) Kresse, G.; Hafner, J. Ab initio molecular dynamics for liquid metals. *Phys. Rev. B* **1993**, *47*, 558-561.
- (33) Blöchl, P. E. Projector augmented-wave method. *Phys. Rev. B* **1994**, *50*, 17953-17979.
- (34) Kresse, G.; Joubert, D. From ultrasoft pseudopotentials to the projector augmented-wave method. *Phys. Rev. B* **1999**, *59*, 1758-1775.
- (35) Perdew, J. P.; Burke, K.; Ernzerhof, M. Generalized gradient approximation made simple. *Phys. Rev. Lett.* **1996**, *77*, 3865-3868.
- (36) Grimme, S.; Ehrlich, S.; Goerigk, L. Effect of the damping function in dispersion corrected density functional theory. *J. Comput. Chem.* **2011**, *32*, 1456-1465.
- (37) Grimme, S.; Antony, J.; Ehrlich, S.; Krieg, H. A consistent and accurate ab initio parametrization of density functional dispersion correction (DFT-D) for the 94 elements H-Pu. *J. Chem. Phys.* **2010**, *132*, 154104.
- (38) Monkhorst, H. J.; Pack, J. D. Special points for Brillouin-zone integrations. *Phys. Rev. B* **1976**, *13*, 5188-5192.
- (39) Datta, D.; Li, J.; Shenoy, V. B. Defective graphene as a high-capacity anode material for Na- and Ca-ion batteries. *ACS Appl. Mater. Interfaces* **2014**, *6*, 1788-1795.
- (40) Stratford, J. M.; Allan, P. K.; Pecher, O.; Chater, P. A.; Grey, C. P. Mechanistic insights into sodium storage in hard carbon anodes using local structure probes. *Chem. Commun.* **2016**, *52*, 12430-12433.
- (41) Zhang, J.; Qu, L.; Shi, G.; Liu, J.; Chen, J.; Dai, L. N. P-Codoped Carbon Networks as Efficient Metal-free Bifunctional Catalysts for Oxygen Reduction and Hydrogen Evolution Reactions. *Angew. Chem., Int. Ed.* **2015**, *55*, 2230-2234.
- (42) Yan, X.; Liu, Y.; Fan, X.; Jia, X.; Yu, Y.; Yang, X. Nitrogen/phosphorus co-doped nonporous carbon nanofibers for high-performance supercapacitors. *J. Power Sources* **2014**, *248*, 745-751.
- (43) Yan, Y.; Yin, Y.-X.; Xin, S.; Guo, Y.-G.; Wan, L.-J. Ionothermal synthesis of sulfur-doped porous carbons hybridized with graphene as superior anode materials for lithium-ion batteries. *Chem. Commun.* **2012**, *48*, 10663-10665.
- (44) Enterría, M.; Pereira, M.; Martins, J.; Figueiredo, J. Hydrothermal functionalization of ordered mesoporous carbons: The effect of boron on supercapacitor performance. *Carbon* **2015**, *95*, 72-83.

- (45) Cancado, L.; Takai, K.; Enoki, T.; Endo, M.; Kim, Y.; Mizusaki, H.; Jorio, A.; Coelho, L.; Magalhaes-Paniago, R.; Pimenta, M. General equation for the determination of the crystallite size L_a of nanographite by Raman spectroscopy. *Appl. Phys. Lett.* **2006**, *88*, 163106-163106.
- (46) Petkov, V.; DiFrancesco, R.; Billinge, S.; Acharya, M.; Foley, H. Local structure of nanoporous carbons. *Philos. Mag. B* **1999**, *79*, 1519-1530.
- (47) Chatterjee, S.; Jones, E. B.; Clingenpeel, A. C.; McKenna, A. M.; Rios, O.; McNutt, N. W.; Keffer, D. J.; Johs, A. Conversion of lignin precursors to carbon fibers with nanoscale graphitic domains. *ACS Sustainable Chem. Eng.* **2014**, *2*, 2002-2010.
- (48) Shi, C.; Redmond, E. L.; Mazaheripour, A.; Juhas, P.; Fuller, T. F.; Billinge, S. J. Evidence for Anomalous Bond Softening and Disorder Below 2 nm Diameter in Carbon-Supported Platinum Nanoparticles from the Temperature-Dependent Peak Width of the Atomic Pair Distribution Function. *J. Phys. Chem. C* **2013**, *117*, 7226-7230.
- (49) Dmowski, W.; Contescu, C. I.; Llobet, A.; Gallego, N. C.; Egami, T. Local atomic density of microporous carbons. *J. Phys. Chem. C* **2012**, *116*, 2946-2951.
- (50) Yao, L.-H.; Cao, W.-Q.; Cao, M.-S. Doping effect on the adsorption of Na atom onto graphenes. *Curr. Appl. Phys.* **2016**, *16*, 574-580.
- (51) Cohn, A. P.; Muralidharan, N.; Carter, R.; Share, K.; Pint, C. L. Anode-free sodium battery through in situ plating of sodium metal. *Nano Lett.* **2017**, *17*, 1296-1301.

Chapter 6 Defective Hard Carbon Anode for Na-ion Batteries

6.1 Abstract

Hard carbon as an anode is critical for the near-future commercialization of Na-ion batteries (NIBs). However, where Na-ions are located at different state of charge with respect to the local structures of hard carbon remains a topic under debating. Recently, some groups including ours have suggested a structure-property correlation that assigns the slope capacity in galvanostatic charge/discharge curves to the binding of Na-ions to structural defects of hard carbon. To test this correlation, herein, we prepared a highly defective hard carbon by microwaving a carbon that was obtained by pyrolysis of cellulose at 650 °C. After this microwave treatment for just 6 seconds, the reversible capacity of the hard carbon rose from 204 to 308 mAh/g, which is significantly higher than hard carbon annealed at 1100 °C for 7 hours (274 mAh/g). The microwave treatment is not only energy efficient but retains a high extent of the structural vacancies in hard carbon, as demonstrated by neutron total scattering and the associated pair distribution function (PDF) results. Indeed, such a defective structure exhibits a much higher slope capacity than the conventional hard carbon. This work serves as one of the first examples of rationally designed hard carbon guided by the new Na-ion storage mechanism. Furthermore, the microwave heating represents a promising strategy for fine tuning the structures of hard carbon for Na-ion batteries.

6.2 Introduction

To store intermittent energy from solar or wind, much attention has been devoted to sustainable storage batteries that employ earth-abundant elements as charge carriers, such as Na-ion batteries (NIBs),¹⁻⁷ K-ion batteries (KIBs),⁸⁻¹³ Al-ion batteries (AIBs),^{14, 15} and Mg-ion batteries (MIBs).¹⁶⁻¹⁸ Among them, NIBs are very competitive as sodium is abundant and widely available around the world, and the energy density of NIBs is relatively high. Often, the anode affects some key metrics of metal-ion batteries, such as safety, cycle life, and rate capability, where carbonaceous anode materials represent the most practically viable candidates for alkali metal ion batteries.¹⁹⁻²⁷ Among the three most inexpensive carbon anode materials—graphite, soft carbon, and hard carbon, hard carbon anode exhibits the best overall performance in NIBs, such as high capacity, high coulombic efficiency, and good cycling stability.^{21, 28-46}

Hard carbon, also known as nongraphitizable carbon, is composed of randomly oriented turbostratic nanodomains, and this type of carbons are typically prepared by high-temperature pyrolysis of oxygen-rich hydrocarbon/biomass precursors.⁴⁷ Despite its promising electrochemical performance in NIBs, the current cost of hard carbon is even higher than graphite, the anode of Li-ion batteries (LIBs). One cost contributor is that hard carbon anode needs to be annealed at high temperatures, *i.e.*, >1100 °C, for at least a few hours.

Recently, the mechanism of Na-ion storage in hard carbon has been revisited, where

the high-potential slope capacity in galvanostatic charge/discharge (GCD) profiles is attributed to Na-ion binding to structural defects.⁴⁸⁻⁵⁷ This implies that one could enhance the slope capacity by promoting defects in hard carbon. Additional to slope capacity, hard carbon also exhibits low-potential plateau capacity, which is ~ 60% of its total capacity. Yet, due to its vicinity to the Na plating potential, the low-potential plateau causes a concern of dendrite formation. Therefore, a predominantly defective hard carbon may potentially increase overall capacity and address the safety concern. It is known that low-temperature pyrolysis of biomasses generates highly defective amorphous carbon. Nevertheless, such low-temperature annealed carbon does not conduct electrons well, which leads to low capacity values. The question is how to boost the conductivity without removing defects from low-temperature annealed hard carbon (LT-HC).

Herein, we report that microwave heating⁴⁸⁻⁵⁰ for just a few seconds enhances conductivity of LT-HC but retains the highly defective structure. We microwave treated LT-HC formed by the pyrolysis of cellulose filter paper at 650°C. This was conducted in air in a kitchen-style microwave oven. After microwaving for 6 seconds, the capacity of LT-HC went up from 204 to 308 mAh/g, higher than 274 mAh/g of the conventional hard carbon (HT-HC), prepared by pyrolysis of the same precursor at 1100 °C. Pair Distribution Function (PDF) studies associated with neutron total scattering demonstrate that both LT-HC and the microwave-treated hard carbon (MV-HC) contain

greater extents of structural vacancies than HT-HC. Indeed, MV-HC exhibits much higher slope capacity than the conventional hard carbon.

6.3 Experimental Section

Materials Synthesis: In a typical experiment, 2 g filter paper was sonicated in water for 6 h and dried at 80 °C for 12 h and then it was preheated in air at 240 °C for 8 h. Afterwards, the pyrolysis of the filter paper was performed under Ar gas flow at 650 °C for 7 h. The obtained hard carbon was then subjected to the microwave treatment in a kitchen-style microwave (General Electric) oven for 2, or 6, or 10 seconds. The microwave oven used in this work is Emerson MW8995B, and the power we selected for the microwave treatment is 90 W. The high temperature annealed hard carbon was obtained by the pyrolysis of the same preheated filter paper at 1100 °C for 7 h under Ar gas flow.

Materials Characterization: Micromeritics TriStar II 3020 analyzer was used to conduct the N₂ sorption measurements for the BET surface area analysis. Rigaku Ultima IV Diffractometer with Cu K α ($\lambda = 1.5406 \text{ \AA}$) radiation was used for the collection of powder XRD patterns. The X-ray photoelectron spectroscopy (XPS) measurements were conducted with a focused monochromatic Al K α x-ray (1486.6 eV) excitation source in a Physical Electronics Quantera Scanning ESCA Microprobe. The morphology of all the carbons was examined by high resolution scanning electron microscopy (SEM) on FEI NOVA 230. FEI Titan 80-200 Transmission Electron Microscopy (TEM) was

used to record the TEM images. Raman spectra were gathered on a WITec confocal Raman spectrometer with a 514 nm laser source, and the fitting of the spectra was done with Origin 8.5. To perform the neutron total scattering, all the carbon samples were loaded into quartz capillaries, and the data were collected at the Nanoscale Ordered Materials Diffractometer (NOMAD), Spallation Neutron Source, at Oak Ridge National Laboratory.

Electronic conductivity test: The data was collected on an ULVACRIKO ZEM-3 under a helium atmosphere under room temperature. 5 wt% PTFE binder was added to prepare the sample for the conductivity test. Because of the large resistance of LT-HC, the instrument was not able to collect data for LT-HC. As a higher temperature would lead to a higher conductivity, LT-HC was heated up to 300°C to increase its conductivity. However, its conductivity at 300°C is still out of the limits of the instrument (0.2 S/m). This means the conductivity of LT-HC should be much lower than 0.2 S/m.

Electrochemical Measurements: The galvanostatic charge-discharge and cycling tests were carried out with coin cells (CR2032), and the rate capability tests were performed with T-shape three-electrode cells by using two Na-metal foils as the counter electrode and the reference electrode (Figure 6.9). To make the carbon electrodes, 80 wt% active materials, 10 wt% polyvinylidene fluoride (PVdF), and 10 wt% carbon black were mixed together in a mortar with N-Methyl-2-pyrrolidone (NMP). The obtained slurry

was coated onto copper foil and dried at 100 °C for 12 h under vacuum. The loading mass of active materials is between 1.0 to 1.5 mg/cm² for all electrodes. For the two-electrode Carbon/Na half cells in coin cells, sodium metal was used as the counter/reference electrode. The electrolyte for all cells is 1.0 mol/L NaPF₆ solution in ethylene carbonate (EC)/diethyl carbonate (DEC) (1:1 in volume). The galvanostatic charge-discharge and cycling were tested with Maccor 3000 system in the potential range of 0.01-2 V vs Na⁺/Na at room temperature, and the rate capability tests with three-electrode cell was performed on Bio-logic EC Lab VMP-3 under ambient conditions.

Galvanostatic intermittent titration technique (GITT) test: Fick's second law with equation (1) was used to determine the ion diffusion coefficient.

$$D = \frac{4}{\pi} \left(\frac{m_b V_M}{M_B S} \right)^2 \left(\frac{\Delta E_s}{\tau (dE/d\sqrt{\tau})} \right)^2 \quad (\tau \ll L^2/D) \quad (1)$$

Equation (1) can be simplified to equation (2) if the cell potential is linearly proportional to $\tau^{1/2}$ during the current pulse.

$$D = \frac{4}{\pi \tau} \left(\frac{m_b V_M}{M_B S} \right)^2 \left(\frac{\Delta E_s}{\Delta E_\tau} \right)^2 \quad (\tau \ll L^2/D) \quad (2)$$

In this equation, τ is pulse time, m_b is the mass of electrode material, V_M is molar volume of carbon, M_B is the molar mass of hard carbon, S is the contact area and L is the average thickness of the electrode. The density of the obtained hard carbon was tested by Archimedes' method with a density measurement kit and cyclohexane was used as the

solvent. The density for LT-HC, HT-HC and MV-HC is 1.34, 1.45 and 1.38 g/cm³, respectively.

6.4 Results and Discussion

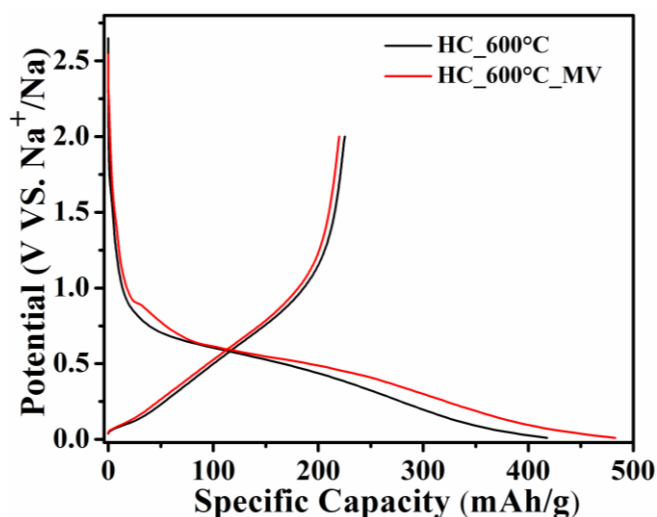


Figure 6.1 First sodiation-desodiation profiles of hard carbon annealed at 600°C before and after the microwave treatment at a current density of 20 mA/g.

The microwave treatment heats up carbon only when the carbon sample is not insulating. Cellulose filter paper pre-annealed at 600°C is not conductive enough to heat up under microwave, where microwaving for 2 minutes only warmed up this sample. This, thus, caused no impact on the performance of Na-ion storage (Figure 6.1). However, for the LT-HC samples pre-annealed at 650°C, after ~2.5 seconds of microwaving, it caught on a bright flame. We found that flaming during microwaving is inevitable after ~2.5 seconds for carbon samples that were pre-annealed at 650°C or above. We selected LT-HC pre-annealed at 650°C for the rest of the studies.

The burnoff of LT-HC after the microwave treatment for 6 seconds is only ~7 wt.%.

X-ray photoelectron spectroscopy (XPS) results show that the oxygen content of LT-HC decreased from 4.5 wt.% to 3.0 wt.%. This means that the burnoff of 5.5 wt.% comes from carbon combustion; this is a minimal scale of carbon loss despite intense flaming of the samples.

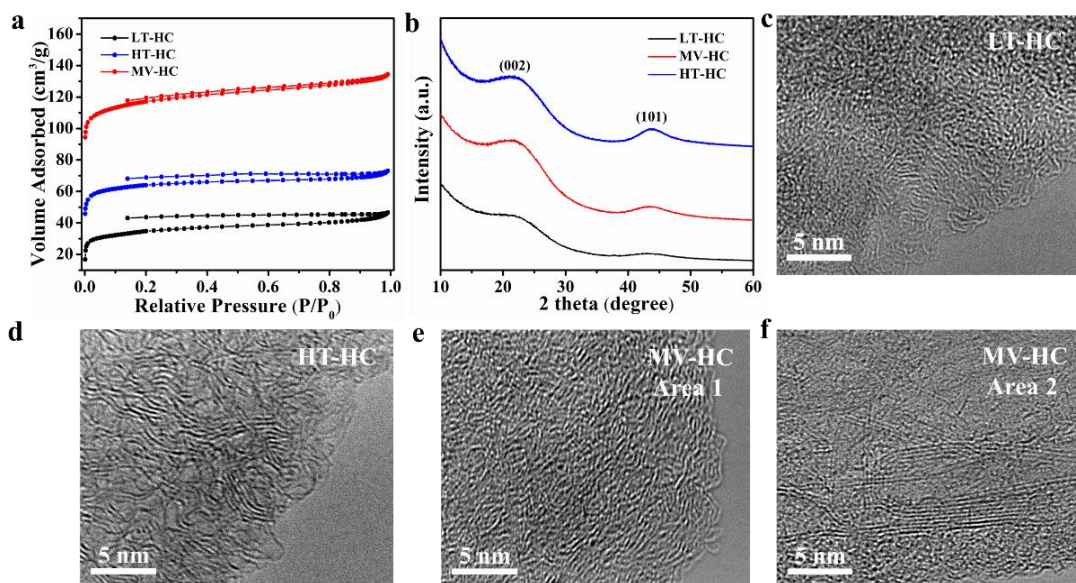


Figure 6.2 (a, b) Nitrogen sorption isotherms and XRD patterns of all hard carbons. TEM images of (c) LT-HC, (d) HT-HC, and (e) Area-1 of MV-HC and (f) Area-2 of MV-HC.

Figure 6.2a shows the N_2 sorption isotherms of LT-HC, HT-HC, and MV-HC (treated for 6 seconds), where their Brunauer-Emmett-Teller (BET) surface areas are 115, 207, and 379 m^2/g , respectively. MV-HC contains a larger volume of micropores than the other two hard carbons, where the t-Plot micropore volume increases from 0.031 cm^3/g of LT-HC to 0.144 cm^3/g of MV-HC, compared to 0.078 cm^3/g of HT-HC. The increased surface area and porosity suggest that the microwave treatment has “activated”

LT-HC. Despite their difference in porosity, no obvious variance shows up in their morphology, as displayed in the scanning electron microscopy (SEM) images (Figure 6.3).

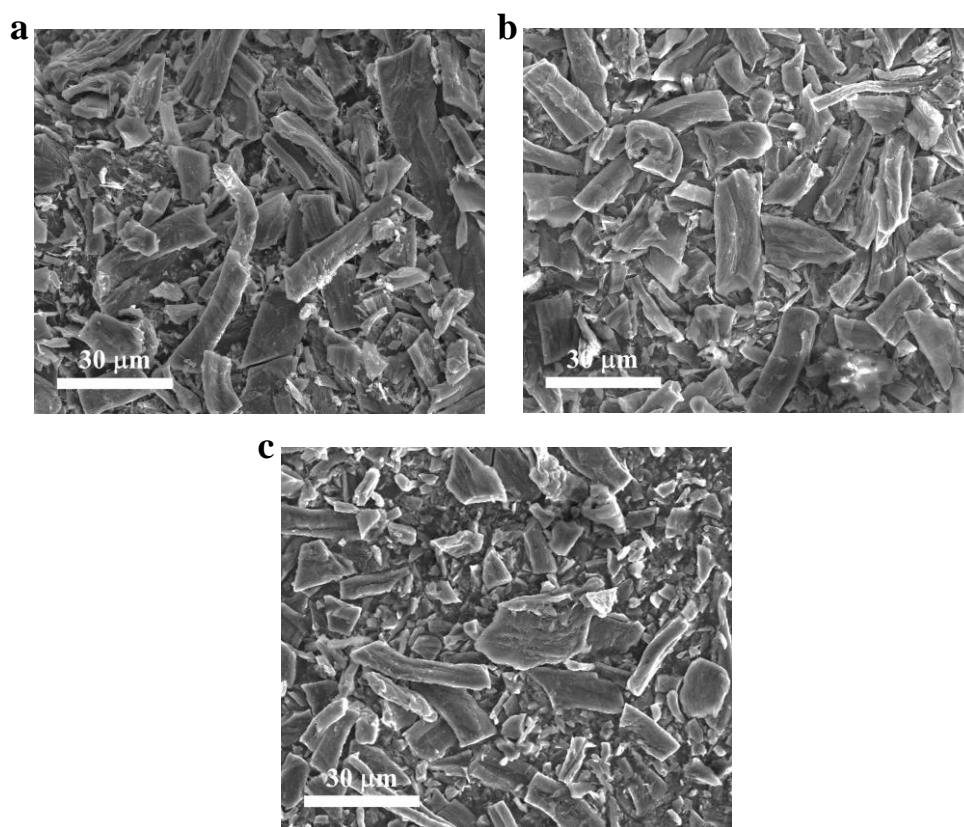


Figure 6.3 SEM images of (a) LT-HC, (b) HT-HC, and (c) MV-HC.

All LT-HC, HT-HC, and MV-HC are nongraphitic carbon as expected, reflected by their XRD patterns with broad (002) and (101) peaks (Figure 6.2b). LT-HC exhibits peaks with lower intensity than HT-HC and MV-HC. Albeit annealing at 650°C eliminates oxygen and hydrogen of cellulose paper, neither graphitization nor graphenization (the formation of order along lateral *ab* planes) goes to a large extent. To examine the

structures of these hard carbons, we took their high-resolution transmission electron microscopy (TEM) images. As shown in Figure 6.2c, LT-HC is highly disordered, and it is difficult to identify any graphenic sheets that are longer than 2 nm. In sharp contrast, the HT-HC comprises distinctly curved graphenic layers longer than 5 nm, where often they stack into turbostratic nanodomains (Figure 6.2d). As for MV-HC, its structure is heterogeneous. On one hand, most of carbon content has a graphenization degree between LT-HC and HT-HC, as shown in a representative TEM image in Figure 6.2e; on the other hand, interestingly, microwave treatment leads to the formation of some highly graphenic stripes, some of which are longer than 15 nm along *ab* planes, as shown representatively in Figure 6.2f. The collective consideration of both TEM and XRD implies that these graphenic stripes do not exhibit long coherence lengths along the *c*-axis; otherwise, it would result in a sharp (200) shoulder peak in the XRD pattern of MV-HC. The TEM results indicate that microwave heating that triggers the flaming is not uniform throughout the carbon structure.

The formation of the graphenic stripes may have a large impact on the electronic conductivity of the hard carbon. The conductivity of LT-HC is so low that it cannot be measured; nevertheless, after the microwave treatment MV-HC exhibits a conductivity of 0.59 S/m, albeit much lower than that of HT-HC, 16.16 S/m. The presence of graphenic stripes plus the decreased oxygen content should be responsible for the greatly increased electronic conductivity.

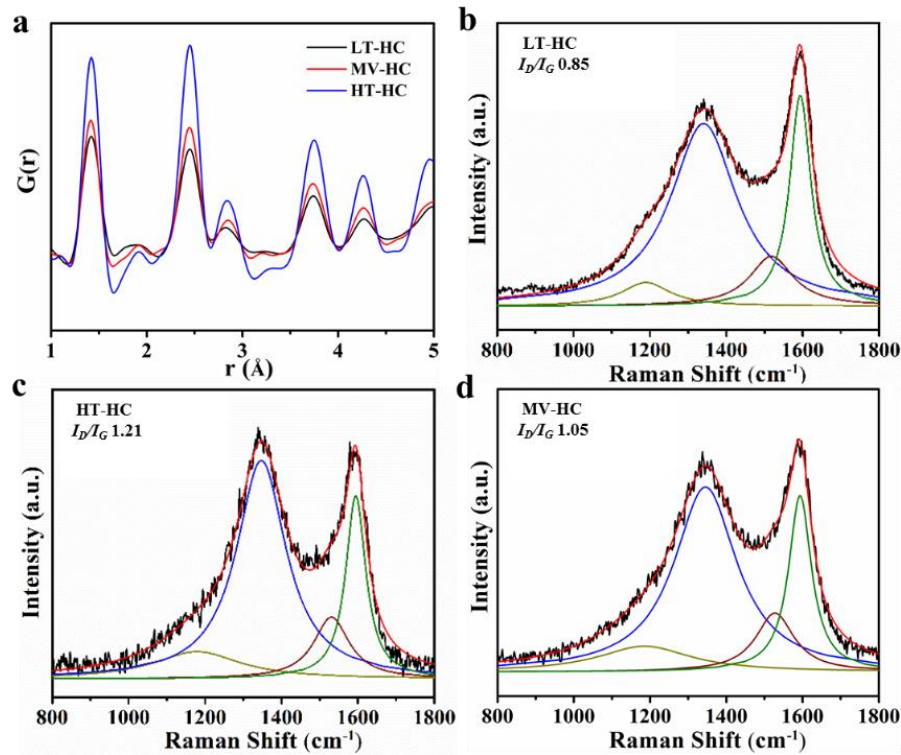


Figure 6.4 (a) PDF studies associated with the neutron total scattering of LT-HC, HT-HC, and MV-HC. Deconvoluted Raman spectra of all hard carbons with four Lorentzian peaks: TPA (dark yellow), D (blue), A (wine) and G (green). (b) LT-HC, (c) HT-HC, and (d) MV-HC.

We aimed to use the microwave treatment to retain most of the structural defects in MV-HC. To characterize the extent of the defective structure of hard carbons, we employed neutron total scattering, PDF, and Raman spectroscopy studies. PDF studies associated with neutron total scattering has been demonstrated invaluable to reveal the extent of defects in our prior hard carbon studies.⁵¹⁻⁵³ Via a Fourier transform of the structure functions $S(Q)$ by Equation (3), the PDF results were obtained.

$$\frac{A}{4\pi}G(r) = A\rho[g(r) - 1] = \frac{1}{2\pi^2}\sum_0^{Q^{max}}QA[S(Q) - 1]\sin(QR)\Delta Q \quad (3)$$

In this equation, A is a constant formed during normalization, ρ is the atomic number density, $g(r)$ represents the atomic pair distribution function, and Q is the scattering vector. In the $G(r)$ plots of the radial distribution maps (Figure 6.4), the peak positions (r) represent the real space distances between a central carbon atom that is arbitrarily chosen, and its neighbors averaged over all atoms. The peak amplitude is proportional to the probability of finding atoms at that distance, which means that a more graphenic carbon structure will exhibit a higher peak amplitude whereas a more defective structure along ab planes will have a lower peak amplitude. As shown in Figure 6.4a, the PDF results reveal that both LT-HC and MV-HC are much more defective, i.e., containing more vacancies, than HT-HC, and MV-HC is only slightly less defective than LT-HC even though MV-HC is much more conductive.

Raman spectra of all hard carbons were also collected and deconvoluted into four Lorentzian peaks, as shown in Figure 6.4b-d.⁵⁴ The D band at $\sim 1345\text{ cm}^{-1}$ is assigned to the A_{1g} breathing mode of carbon aromatic rings, which is induced by defects, and the G band at $\sim 1595\text{ cm}^{-1}$ is attributed to the E_{2g} vibration of the sp^2 carbon atoms. It has been widely accepted that I_D/I_G ratio is proportional to the defect concentration, which is inversely proportional to the graphenic domain size along the ab planes. However, there exist boundaries for this correlation; when the graphenic domain sizes are below 2 nm, this correlation is reversed, meaning that a higher I_D/I_G correlates to a higher domain size along the ab planes, and thus indicates lower defect concentrations.⁵⁵ As shown in Figure 6.4b-d, the LT-HC exhibits the lowest I_D/I_G ratio of 0.85, where by

considering the domain size of LT-HC being below 2 nm revealed from the TEM results, the Raman results corroborate the PDF results that LT-HC owns the highest defect concentration among our samples. With less defects, the I_D/I_G ratio of MV-HC (1.05) is higher than LT-HC because the domain size along *ab* planes in MV-HC is on average also below 2 nm, as shown in Figure 6.2c. The I_D/I_G ratio of HT-HC (1.21) is much higher than the other two carbons, where, however, such a comparison may not be meaningful since the average domain size along *ab* planes in HT-HC is most likely larger than 2 nm. Both the neutron total scattering and Raman results reveal that the defect concentration in MV-HC is slightly diminished after the microwave treatment, but it is still much higher than that of HT-HC.

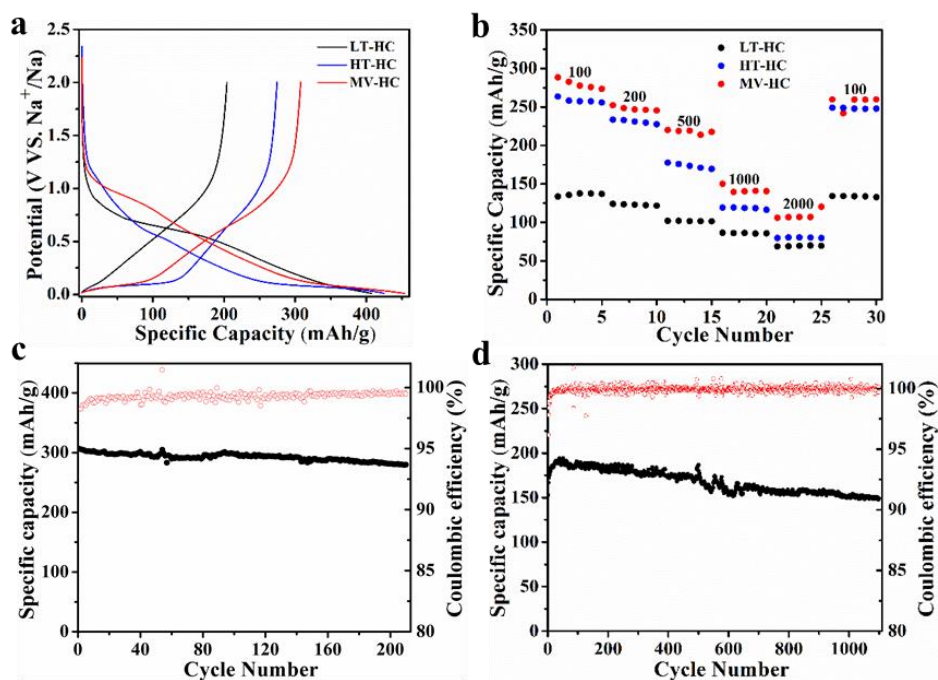


Figure 6.5 (a) The first-cycle galvanostatic sodiation/desodiation potential profiles of three hard carbons at a current rate of 20 mA/g. The potential is vs Na⁺/Na. (b) Rate capability of three hard carbons at various current density in three-electrode cells. Long cycling performance of MV-HC at (c) 20 mA/g and (d) 200 mA/g.

Table 6.1 The first-cycle reversible Na-ion storage capacities of three hard carbons and the capacities from plateau and slope regions at current density of 20 mA/g.

Reversible capacity (mAh/g)	LT-HC	HT-HC	MV-HC	MV-HC_2	MV-HC_10
Total reversible capacity	204	274	308	256	250
Plateau capacity (0-0.2 V)	42	147	112	81	143
Slope capacity (0.2-2 V)	162	127	196	175	107

The Na-ion storage performance of all the obtained hard carbon is evaluated in Carbon/Na half-cells. Even though LT-HC has the highest defect concentration among three hard carbons, it shows the lowest reversible Na-ion storage capacity of 204 mAh/g with the first cycle coulombic efficiency (FCCE) of only 50% in galvanostatic charge/discharge (GCD) cycling (Figure 6.5a). In sharp contrast to LT-HC, after a microwave treatment for 6 seconds, MV-HC shows a much higher reversible capacity of 308 mAh/g with the FCCE of 68%. The cyclic voltammetry (CV) results of LT-HC and MV-HC are shown in Figure 6.6, where in the first sodiation process, MV-HC shows a smaller irreversible reduction peak than LT-HC, agreeing with its higher FCCE from the GCD results.

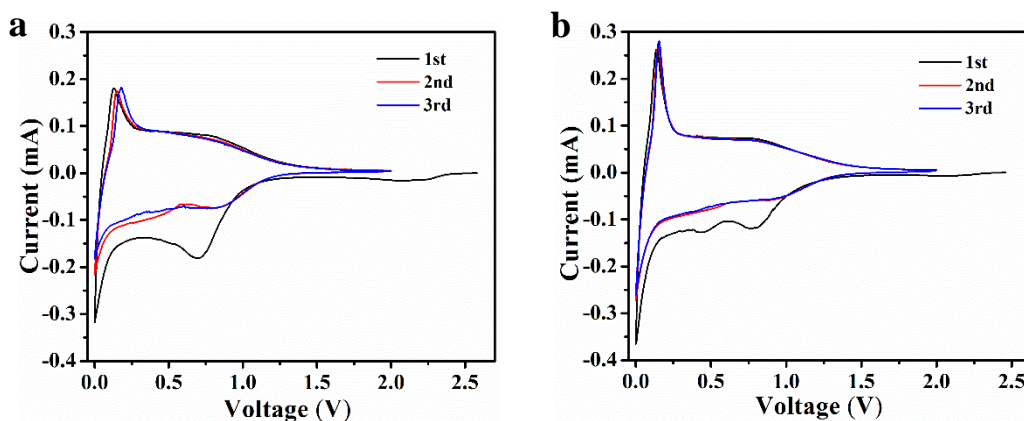


Figure 6.6 Cyclic voltammetry results of (a) LT-HC and (b) MV-HC.

The Na-ion storage capacity of MV-HC is even higher than the conventional HT-HC, which is 274 mAh/g with the FCCE of 64%. Our prior studies reveal that given similar structures and morphology of hard carbon NIB anodes, a higher surface area would lower capacity and FCCE values. This can be understood that a higher surface area causes more pronounced side reactions between the electrolyte and the anode.⁵⁶ However, the surface areas of LT-HC, HT-HC, and MV-HC are 115, 207, and 379 m²/g, respectively, where MV-HC, exhibits the highest capacity and the best FCCE despite its inevitably more surface-bound side reactions. Note that these three carbons mainly differ by their structures, and the extraordinarily good performance of MV-HC further demonstrates the dominance of its more suitable local structures, particularly the retained defect sites, for Na-ion storage. Surface functionalities may also play a role in the performance of hard carbon anodes. The oxygen content of the LT-HC is 4.5 wt.%, which goes to 3.0 wt.% after the microwave treatment, and it is 2.7 wt.% for a conventional hard carbon. Such variance does not warrant it as a primary factor affecting capacities of these different carbon materials.

To deconvolute the higher capacity of MV-HC, its slope capacity is 196 mAh/g, much higher than 127 mAh/g of HT-HC, which are 64% and 46% of the total capacities of MV-HC and HT-HC, respectively. A larger contribution of the slope capacity would lower the risk of dendrite formation. This is recognized as an advantage of soft carbon NIB anodes as well. However, the overall capacity of soft carbon is much lower. Note that if the potential of the slope capacity is high, i.e., 1 V, the more slope capacity would

not significantly enhance the energy density of a full cell; however, the potential for most of the increased slope capacity of MV-HC is still low, below 1.0 V.

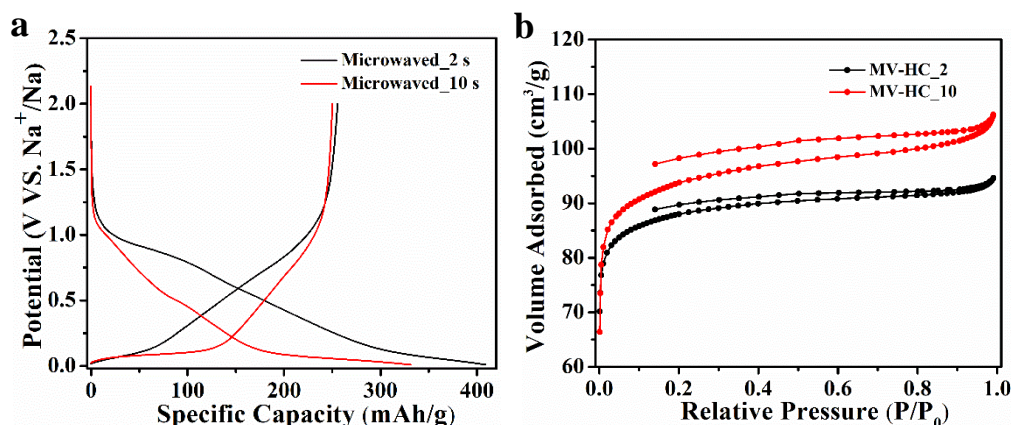


Figure 6.7 (a) First sodiation-desodiation potential profiles of hard carbon microwaved for 2 and 10 seconds at a current density of 20 mA/g. (b) Nitrogen sorption isotherms of MV-HC₂ and MV-HC-10.

We selected a duration of 6 seconds for the microwave treatment because it appears that this duration provides the best capacity as the capacity values of hard carbon obtained by the microwave treatment for 2 seconds (referred to as MV-HC₂) and 10 seconds (MV-HC₁₀) are only 256 and 250 mAh/g, respectively (Figure 6.7a). Even though it is a very short time frame for the microwave treatment, the results are very reproducible where the error bar for the time frame is around one second. The BET surface area of MV-HC₂ and MV-HC₁₀ is 283 and 302 m²/g, respectively (Figure 6.7b). The changes of the micropore volume shows the same trend with the BET surface area, where it increases from 0.031 cm³/g of LT-HC to 0.116 cm³/g of MV-HC₂ and 0.144 cm³/g of MV-HC, and then decreases to 0.117 cm³/g of MV-HC₁₀. These results suggest that in the beginning of the microwave process, micropores are generated by

the consumption of carbon atoms and the surrounding oxygen atoms. High-resolution TEM images and Raman spectra of MV-HC_2 and MV-HC_10 were also collected as shown in Figure 6.8. These results reveal that MV-HC_2 with a slightly larger domain size than LT-HC is less defective than LT-HC but more defective than MV-HC, whereas the MV-HC_10 with a much larger average domain size than MV-HC is even more ordered (graphenic) than HT-HC. We tested the electrochemical properties of these microwaved hard carbons, as summarized in Table 1. MV-HC_10 demonstrates a large plateau capacity comparable to that of HT-HC, whereas MV-HC and MV-HC_2 with higher defect concentrations deliver higher portions of slope capacity. This general structure-property correlation agrees well with the proposed mechanism about Na-ion storage in hard carbon.

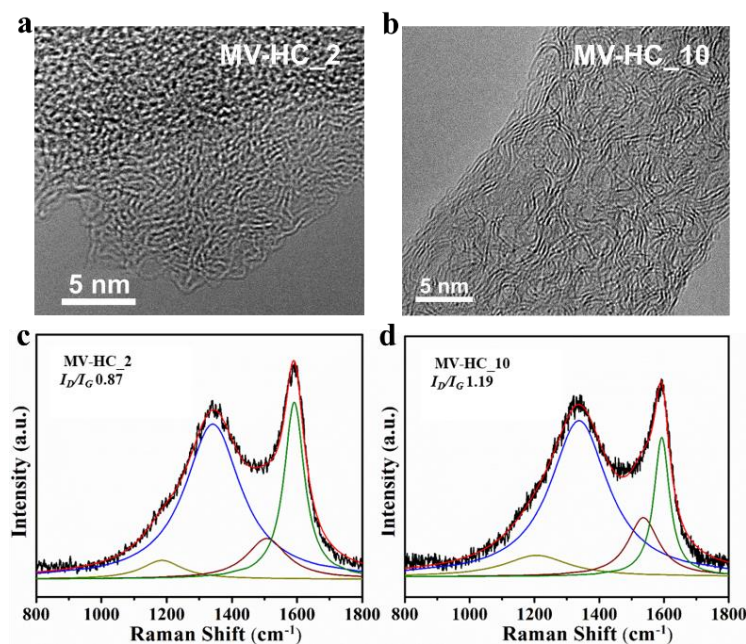


Figure 6.8 TEM images of (a) MV-HC_2 and (b) MV-HC_10. Deconvoluted Raman spectra of hard carbons with four Lorentzian peaks: TPA (dark yellow), D (blue), A (wine) and G (green). (c) MV-HC_2 and (d) MV-HC_10.

We tested the rate capability of LT-HC, HT-HC, and MV-HC with three-electrode cells, where Na metal foils are employed as both counter and reference electrodes (Figure 6.9). We employed three-electrode cells because the rate capability of conventional hard carbon would be much underestimated in the two-electrode Carbon/Na half-cell setup.⁵⁰ As shown in Figure 6.5b, MV-HC shows a higher capacity than both LT-HC and HT-HC at all current rates. Especially at 500 mA/g, the capacity disparity between MV-HC and HT-HC is significant. The reasons that MV-HC shows a much better rate capability will be discussed later.

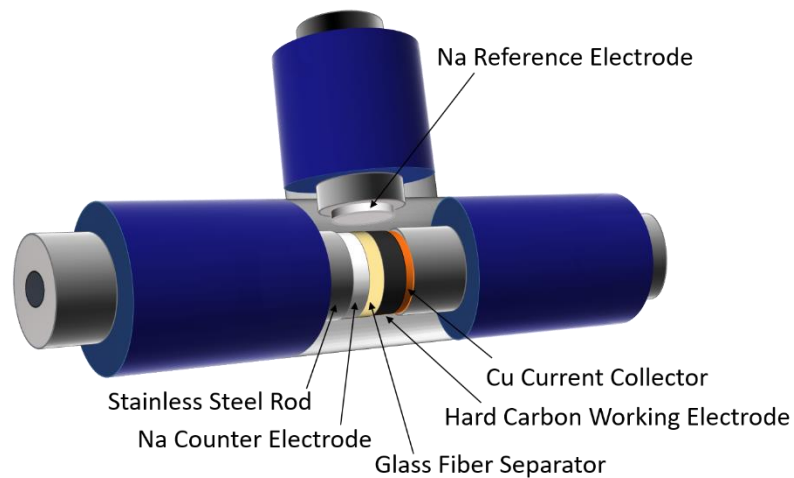


Figure 6.9 Schematic of three-electrode cell used for rate capability test.

We evaluated the cycle life of MV-HC in C/Na half cells at current rates of 20 mA/g and 200 mA/g, as shown in Figure 6.5c and d. At 20 mA/g, after 210 cycles MV-HC maintained its capacity at 288 mAh/g with the capacity retention of 91% (Figure 6.5c). At 200 mA/g, the capacity retention is 85% after 1100 cycles. Note that the initial

capacity of MV-HC in half-cells is lower than that recorded in three-electrode cells at 200 mA/g; therefore, it is more relevant to pay attention to the capacity retention percentage instead of the capacity values. The lower capacity at high current rate in half-cells is due to the overpotential of the Na counter electrode which we revealed before,⁵⁷ where such overpotential is caused by the high interfacial impedance of Na counter electrode, as reported by Iermakova et al.⁵⁸ This long cycling life is one of the longest for hard carbon anodes with the active mass loading of $\sim 1.5 \text{ mg/cm}^2$.

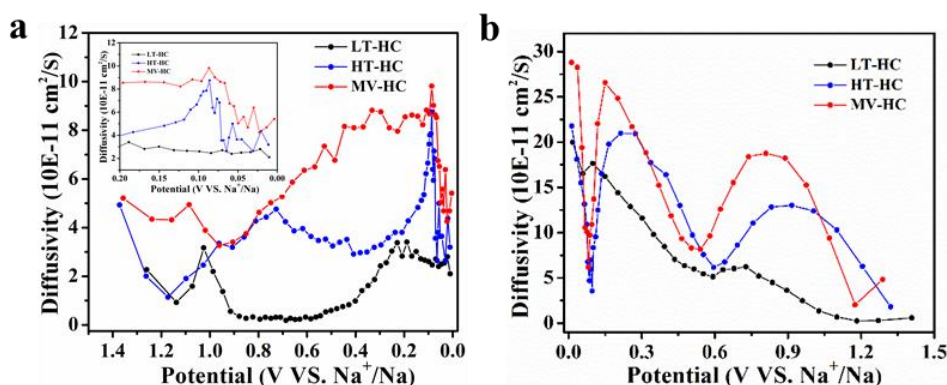


Figure 6.10 Diffusivity as a function of (de)sodiation potentials of hard carbons from GITT measurements (a) First sodiation. Inset: the low potential range, and (b) First desodiation.

The reversible slope capacity of LT-HC is lower than MV-HC even though its defect concentration is higher. This may have to do with the very low electronic and ionic conductivity of LT-HC. We measured the reversible capacity of LT-HC at a very low current rate of 2 mA/g, where a reversible capacity of 254 mAh/g can be obtained, and its slope capacity is 219 mAh/g comparable to that of MV-HC measured at 2 mA/g (Figure 6.11a). These results indicate that LT-HC has inherently high slope capacity, which is, however, limited by its poor charge carrier transport properties. As

as mentioned, LT-HC shows a much lower electronic conductivity than MV-HC. We further compare the Na-ion diffusion coefficient between different hard carbons by conducting galvanostatic intermittent titration technique (GITT) tests (Figure 6.10 and Figure 6.11b). As shown in Figure 6.10, LT-HC exhibits the lowest Na-ion diffusivity at almost all different potentials, while MV-HC shows the highest Na-ion diffusivity. The higher surface area with a larger micropore volume of MV-HC may be responsible for its high Na-ion diffusivity. Overall, the low Na-ion storage capacity of LT-HC can be attributed to the low electronic conductivity and poor Na-ion diffusivity. The higher Na-ion diffusivity is also one of the reasons for the much higher capacity of MV-HC than HT-HC at a current rate of 500 mA/g. Additionally, the larger domain size of HT-HC would lead to much plateau capacity that cannot be revealed at high current rates.

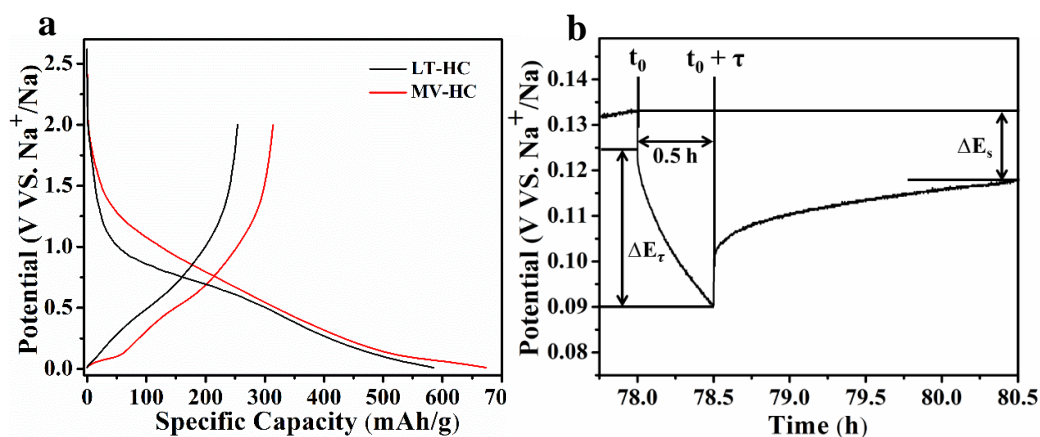


Figure 6.11 (a) First sodiation-desodiation potential profiles of LT-HC and MV-HC at a current density of 2 mA/g. (b) The potential profile of the GITT test at the potential of 0.12 V with the parameters labeled.

In addition, the sudden drop of Na-ion diffusivity at around 0.1 V for HT-HC and MV-HC suggests that the Na-ion (de)insertion around 0.1 V is more sluggish, which was

postulated to correlate to (de)intercalation inside the turbostratic nanodomains. However, LT-HC does not show such a diffusivity drop, which agrees with the fact that graphitic nanodomains have yet to be formed in LT-HC, where the Na-ion intercalation into non-existing nanodomains is irrelevant and there is no plateau for LT-HC. This phenomenon generally supports the plateau-intercalation correlation.

6.5 Conclusions

Guided by the new mechanism of Na-ion storage in hard carbon, we designed a highly defective hard carbon via a facile method of microwave treatment of a low-temperature annealed hard carbon. This energy-efficient synthetic method renders a unique heterogeneous structure hard carbon, which comprises highly ordered graphenic stripes in an overwhelmingly disordered structure with high concentrations of defects. The microwaved hard carbon shows a higher capacity and rate capability better than those of both LT-HC and conventional HT-HC. Neutron total scattering and the associated PDF studies reveal that MV-HC retains most of its defects during the microwave treatment for 6 s. MV-HC's high capacity benefits from its enhanced slope capacity that is attributed to its highly defective structure. We also revealed that the high defect concentration is not the only factor for high capacity. The premise of realizing a high capacity is high electronic and ionic conductivity, which explains why the more defective LT-HC exhibits less capacity than MV-HC does. The structure-property correlation of the newly designed MV-HC provides new evidence to support the defect-slope capacity correlation of Na-ion storage in hard carbon.

6.6 References

- (1) Guignard, M.; Didier, C.; Darriet, J.; Bordet, P.; Elkaïm, E.; Delmas, C. P2-Na_xVO₂ system as electrodes for batteries and electron-correlated materials. *Nat. Mater.* **2013**, *12*, 74-80.
- (2) Jian, Z.; Zhao, L.; Pan, H.; Hu, Y.-S.; Li, H.; Chen, W.; Chen, L. Carbon coated Na₃V₂(PO₄)₃ as novel electrode material for sodium ion batteries. *Electrochem. Commun.* **2012**, *14*, 86-89.
- (3) Zhao, C.; Lu, Y.; Li, Y.; Jiang, L.; Rong, X.; Hu, Y. S.; Li, H.; Chen, L. Novel Methods for Sodium-Ion Battery Materials. *Small Methods* **2017**, *1*, 1600063.
- (4) Sun, J.; Lee, H.-W.; Pasta, M.; Yuan, H.; Zheng, G.; Sun, Y.; Li, Y.; Cui, Y. A phosphorene-graphene hybrid material as a high-capacity anode for sodium-ion batteries. *Nat. Nanotechnol.* **2015**, *10*, 980-985.
- (5) Ni, J.; Fu, S.; Wu, C.; Maier, J.; Yu, Y.; Li, L. Self-Supported Nanotube Arrays of Sulfur-Doped TiO₂ Enabling Ultrastable and Robust Sodium Storage. *Adv. Mater.* **2016**, *28*, 2259-2265.
- (6) Palomares, V.; Serras, P.; Villaluenga, I.; Hueso, K. B.; Carretero-González, J.; Rojo, T. Na-ion batteries, recent advances and present challenges to become low cost energy storage systems. *Energy Environ. Sci.* **2012**, *5*, 5884-5901.
- (7) Hwang, J.-Y.; Oh, S.-M.; Myung, S.-T.; Chung, K. Y.; Belharouak, I.; Sun, Y.-K. Radially aligned hierarchical columnar structure as a cathode material for high energy density sodium-ion batteries. *Nat. Commun.* **2015**, *6*, 6865.
- (8) Jian, Z.; Luo, W.; Ji, X. Carbon electrodes for K-ion batteries. *J. Am. Chem. Soc.* **2015**, *137*, 11566-11569.
- (9) Komaba, S.; Hasegawa, T.; Dahbi, M.; Kubota, K. Potassium intercalation into graphite to realize high-voltage/high-power potassium-ion batteries and potassium-ion capacitors. *Electrochem. Commun.* **2015**, *60*, 172-175.
- (10) Luo, W.; Wan, J.; Ozdemir, B.; Bao, W.; Chen, Y.; Dai, J.; Lin, H.; Xu, Y.; Gu, F.; Barone, V. Potassium ion batteries with graphitic materials. *Nano Lett.* **2015**, *15*, 7671-7677.
- (11) Jian, Z.; Xing, Z.; Bommier, C.; Li, Z.; Ji, X. Hard Carbon Microspheres: Potassium-Ion Anode Versus Sodium-Ion Anode. *Adv. Energy Mater.* **2016**, *6*, 1501874.
- (12) Xue, L.; Li, Y.; Gao, H.; Zhou, W.; Lü, X.; Kaveevivitchai, W.; Manthiram, A.; Goodenough, J. B. Low-Cost High-Energy Potassium Cathode. *J. Am. Chem. Soc.* **2017**, *139*, 2164-2167.
- (13) Jian, Z.; Hwang, S.; Li, Z.; Hernandez, A. S.; Wang, X.; Xing, Z.; Su, D.; Ji, X. Hard-Soft Composite Carbon as a Long-Cycling and High-Rate Anode for Potassium-Ion Batteries. *Adv. Funct. Mater.* **2017**, *27*, 1700324.

- (14) Lin, M.-C.; Gong, M.; Lu, B.; Wu, Y.; Wang, D.-Y.; Guan, M.; Angell, M.; Chen, C.; Yang, J.; Hwang, B.-J. An ultrafast rechargeable aluminium-ion battery. *Nature* **2015**, *520*, 324-328.
- (15) Hu, Y.; Ye, D.; Luo, B.; Hu, H.; Zhu, X.; Wang, S.; Li, L.; Peng, S.; Wang, L. A Binder-Free and Free-Standing Cobalt Sulfide@Carbon Nanotube Cathode Material for Aluminum-Ion Batteries. *Adv. Mater.* **2017**, *30*, 1703824.
- (16) Yoo, H. D.; Shterenberg, I.; Gofer, Y.; Gershinshy, G.; Pour, N.; Aurbach, D. Mg rechargeable batteries: an on-going challenge. *Energy Environ. Sci.* **2013**, *6*, 2265-2279.
- (17) Shao, Y.; Gu, M.; Li, X.; Nie, Z.; Zuo, P.; Li, G.; Liu, T.; Xiao, J.; Cheng, Y.; Wang, C. Highly reversible Mg insertion in nanostructured Bi for Mg ion batteries. *Nano Lett.* **2013**, *14*, 255-260.
- (18) Aurbach, D.; Lu, Z.; Schechter, A.; Gofer, Y.; Gizbar, H.; Turgeman, R.; Cohen, Y.; Moshkovich, M.; Levi, E. Prototype systems for rechargeable magnesium batteries. *Nature* **2000**, *407*, 724-727.
- (19) Wenzel, S.; Hara, T.; Janek, J.; Adelhelm, P. Room-temperature sodium-ion batteries: improving the rate capability of carbon anode materials by templating strategies. *Energy Environ. Sci.* **2011**, *4*, 3342-3345.
- (20) Yan, Y.; Yin, Y. X.; Guo, Y. G.; Wan, L. J. A Sandwich-Like Hierarchically Porous Carbon/Graphene Composite as a High-Performance Anode Material for Sodium-Ion Batteries. *Adv. Energy Mater.* **2014**, *4*, 1301584.
- (21) Xu, J.; Wang, M.; Wickramaratne, N. P.; Jaroniec, M.; Dou, S.; Dai, L. High-Performance Sodium Ion Batteries Based on a 3D Anode from Nitrogen-Doped Graphene Foams. *Adv. Mater.* **2015**, *27*, 2042-2048.
- (22) Hou, H.; Qiu, X.; Wei, W.; Zhang, Y.; Ji, X. Carbon Anode Materials for Advanced Sodium-Ion Batteries. *Adv. Energy Mater.* **2017**, *7*, 1602898.
- (23) Licht, S.; Douglas, A.; Ren, J.; Carter, R.; Lefler, M.; Pint, C. L. Carbon nanotubes produced from ambient carbon dioxide for environmentally sustainable lithium-ion and sodium-ion battery anodes. *ACS Cent. Sci.* **2016**, *2*, 162-168.
- (24) Cohn, A. P.; Share, K.; Carter, R.; Oakes, L.; Pint, C. L. Ultrafast Solvent-Assisted Sodium Ion Intercalation into Highly Crystalline Few-Layered Graphene. *Nano Lett.* **2015**, *16*, 543-548.
- (25) Xiao, W.; Sun, Q.; Liu, J.; Xiao, B.; Glans, P.-A.; Li, J.; Li, R.; Guo, J.; Yang, W.; Sham, T.-K., et al. Utilizing the full capacity of carbon black as anode for Na-ion batteries via solvent co-intercalation. *Nano Res.* **2017**, *10*, 4378-4387.
- (26) Yu, Z.; Song, J.; Wang, D.; Wang, D. Advanced anode for sodium-ion battery with promising long cycling stability achieved by tuning phosphorus-carbon nanostructures. *Nano Energy* **2017**, *40*, 550-558.

- (27) Zhou, D.; Peer, M.; Yang, Z.; Pol, V. G.; Key, F. D.; Jorne, J.; Foley, H. C.; Johnson, C. S. Long cycle life microporous spherical carbon anodes for sodium-ion batteries derived from furfuryl alcohol. *J. Mater. Chem. A* **2016**, *4*, 6271-6275.
- (28) Zhang, H.; Ming, H.; Zhang, W.; Cao, G.; Yang, Y. Coupled Carbonization Strategy toward Advanced Hard Carbon for High-Energy Sodium-Ion Battery. *ACS Appl. Mater. Interfaces* **2017**, *9*, 23766-23774.
- (29) Li, Y.; Hu, Y. S.; Titirici, M. M.; Chen, L.; Huang, X. Hard Carbon Microtubes Made from Renewable Cotton as High-Performance Anode Material for Sodium-Ion Batteries. *Adv. Energy Mater.* **2016**, *6*, 1600659.
- (30) Shen, F.; Luo, W.; Dai, J.; Yao, Y.; Zhu, M.; Hitz, E.; Tang, Y.; Chen, Y.; Sprenkle, V. L.; Li, X., et al. Ultra-Thick, Low-Tortuosity, and Mesoporous Wood Carbon Anode for High-Performance Sodium-Ion Batteries. *Adv. Energy Mater.* **2016**, *6*, 1600377.
- (31) Xu, D.; Chen, C.; Xie, J.; Zhang, B.; Miao, L.; Cai, J.; Huang, Y.; Zhang, L. A Hierarchical N/S-Codoped Carbon Anode Fabricated Facilely from Cellulose/Polyaniline Microspheres for High-Performance Sodium-Ion Batteries. *Adv. Energy Mater.* **2016**, *6*, 1501929.
- (32) Yang, J.; Zhou, X.; Wu, D.; Zhao, X.; Zhou, Z. S-Doped N-Rich Carbon Nanosheets with Expanded Interlayer Distance as Anode Materials for Sodium-Ion Batteries. *Adv. Mater.* **2017**, *29*, 1604108.
- (33) Yang, T.; Qian, T.; Wang, M.; Shen, X.; Xu, N.; Sun, Z.; Yan, C. A Sustainable Route from Biomass Byproduct Okara to High Content Nitrogen-Doped Carbon Sheets for Efficient Sodium Ion Batteries. *Adv. Mater.* **2016**, *28*, 539-545.
- (34) Qie, L.; Chen, W.; Xiong, X.; Hu, C.; Zou, F.; Hu, P.; Huang, Y. Sulfur-Doped Carbon with Enlarged Interlayer Distance as a High-Performance Anode Material for Sodium-Ion Batteries. *Adv. Sci.* **2015**, *2*, 1500195.
- (35) Li, M.; Carter, R.; Cohn, A. P.; Pint, C. L. Interconnected foams of helical carbon nanofibers grown with ultrahigh yield for high capacity sodium ion battery anodes. *Carbon* **2016**, *107*, 109-115.
- (36) Zhu, J.; Chen, C.; Lu, Y.; Ge, Y.; Jiang, H.; Fu, K.; Zhang, X. Nitrogen-doped carbon nanofibers derived from polyacrylonitrile for use as anode material in sodium-ion batteries. *Carbon* **2015**, *94*, 189-195.
- (37) Wang, H. G.; Wu, Z.; Meng, F. L.; Ma, D. L.; Huang, X. L.; Wang, L. M.; Zhang, X. B. Nitrogen-Doped Porous Carbon Nanosheets as Low-Cost, High-Performance Anode Material for Sodium-Ion Batteries. *ChemSusChem* **2013**, *6*, 56-60.
- (38) Pol, V. G.; Lee, E.; Zhou, D.; Dogan, F.; Calderon-Moreno, J. M.; Johnson, C. S. Spherical carbon as a new high-rate anode for sodium-ion batteries. *Electrochim. Acta* **2014**, *127*, 61-67.

- (39) Li, W.; Zhou, M.; Li, H.; Wang, K.; Cheng, S.; Jiang, K. A high performance sulfur-doped disordered carbon anode for sodium ion batteries. *Energy Environ. Sci.* **2015**, *8*, 2916-2921.
- (40) Zhang, S.-W.; Lv, W.; Luo, C.; You, C.-H.; Zhang, J.; Pan, Z.-Z.; Kang, F.-Y.; Yang, Q.-H. Commercial carbon molecular sieves as a high performance anode for sodium-ion batteries. *Energy Storage Mater.* **2016**, *3*, 18-23.
- (41) Dahbi, M.; Kiso, M.; Kubota, K.; Horiba, T.; Chafik, T.; Hida, K.; Matsuyama, T.; Komaba, S. Synthesis of hard carbon from argan shells for Na-ion batteries. *J. Mater. Chem. A* **2017**, *5*, 9917-9928.
- (42) Wang, P.; Zhu, X.; Wang, Q.; Xu, X.; Zhou, X.; Bao, J. Kelp-derived hard carbons as advanced anode materials for sodium-ion batteries. *J. Mater. Chem. A* **2017**, *5*, 5761-5769.
- (43) Zhu, Y.-E.; Yang, L.; Zhou, X.; Li, F.; Wei, J.; Zhou, Z. Boosting the rate capability of hard carbon with an ether-based electrolyte for sodium ion batteries. *J. Mater. Chem. A* **2017**, *5*, 9528-9532.
- (44) Stevens, D.; Dahn, J. High Capacity Anode Materials for Rechargeable Sodium-Ion Batteries. *J. Electrochem. Soc.* **2000**, *147*, 1271-1273.
- (45) Xiao, L.; Cao, Y.; Henderson, W. A.; Sushko, M. L.; Shao, Y.; Xiao, J.; Wang, W.; Engelhard, M. H.; Nie, Z.; Liu, J. Hard carbon nanoparticles as high-capacity, high-stability anodic materials for Na-ion batteries. *Nano Energy* **2016**, *19*, 279-288.
- (46) Jache, B.; Adelhelm, P. Use of Graphite as a Highly Reversible Electrode with Superior Cycle Life for Sodium-Ion Batteries by Making Use of Co-Intercalation Phenomena. *Angew. Chem. Int. Ed.* **2014**, *53*, 10169-10173.
- (47) Franklin, R. E. Crystallite growth in graphitizing and nongraphitizing carbons. *Proc. R. Soc. London, Ser. A* **1951**, *209*, 196-218.
- (48) Komaba, S.; Murata, W.; Ishikawa, T.; Yabuuchi, N.; Ozeki, T.; Nakayama, T.; Ogata, A.; Gotoh, K.; Fujiwara, K. Electrochemical Na insertion and solid electrolyte interphase for hard-carbon electrodes and application to Na-Ion batteries. *Adv. Funct. Mater.* **2011**, *21*, 3859-3867.
- (49) Cao, Y.; Xiao, L.; Sushko, M. L.; Wang, W.; Schwenzler, B.; Xiao, J.; Nie, Z.; Saraf, L. V.; Yang, Z.; Liu, J. Sodium ion insertion in hollow carbon nanowires for battery applications. *Nano Lett.* **2012**, *12*, 3783-3787.
- (50) Ding, J.; Wang, H.; Li, Z.; Kohandehghan, A.; Cui, K.; Xu, Z.; Zahiri, B.; Tan, X.; Lotfabad, E. M.; Olsen, B. C. Carbon nanosheet frameworks derived from peat moss as high performance sodium ion battery anodes. *ACS Nano* **2013**, *7*, 11004-11015.
- (51) Tsai, P.-c.; Chung, S.-C.; Lin, S.-k.; Yamada, A. Ab initio study of sodium intercalation into disordered carbon. *J. Mater. Chem. A* **2015**, *3*, 9763-9768.
- (52) Bommier, C.; Surta, T. W.; Dolgos, M.; Ji, X. New mechanistic insights on Na-ion storage in nongraphitizable carbon. *Nano Lett.* **2015**, *15*, 5888-5892.

- (53) Stratford, J. M.; Allan, P. K.; Pecher, O.; Chater, P. A.; Grey, C. P. Mechanistic insights into sodium storage in hard carbon anodes using local structure probes. *Chem. Commun.* **2016**, 52, 12430-12433.
- (54) Zhang, B.; Ghimbeu, C. M.; Laberty, C.; Vix-Guterl, C.; Tarascon, J. M. Correlation between microstructure and Na storage behavior in hard carbon. *Adv. Energy Mater.* **2016**, 6, 1501588.
- (55) Li, Z.; Ma, L.; Surta, T. W.; Bommier, C.; Jian, Z.; Xing, Z.; Stickle, W. F.; Dolgos, M.; Amine, K.; Lu, J. High Capacity of Hard Carbon Anode in Na-Ion Batteries Unlocked by POx Doping. *ACS Energy Lett.* **2016**, 1, 395-401.
- (56) Qiu, S.; Xiao, L.; Sushko, M. L.; Han, K. S.; Shao, Y.; Yan, M.; Liang, X.; Mai, L.; Feng, J.; Cao, Y. Manipulating Adsorption–Insertion Mechanisms in Nanostructured Carbon Materials for High-Efficiency Sodium Ion Storage. *Adv. Energy Mater.* **2017**, 7, 1700403.
- (57) Li, Z.; Bommier, C.; Chong, Z. S.; Jian, Z.; Surta, T. W.; Wang, X.; Xing, Z.; Neufeind, J. C.; Stickle, W. F.; Dolgos, M. Mechanism of Na-Ion Storage in Hard Carbon Anodes Revealed by Heteroatom Doping. *Adv. Energy Mater.* **2017**, 7, 1602894.
- (58) Kim, T.; Jo, C.; Lim, W.-G.; Lee, J.; Lee, J.; Lee, K.-H. Facile conversion of activated carbon to battery anode material using microwave graphitization. *Carbon* **2016**, 104, 106-111.
- (59) Ali, G.; Mehmood, A.; Ha, H. Y.; Kim, J.; Chung, K. Y. Reduced graphene oxide as a stable and high-capacity cathode material for Na-ion batteries. *Sci. Rep.* **2017**, 7, 40910.
- (60) Liu, R.; Zhang, Y.; Ning, Z.; Xu, Y. A Catalytic Microwave Process for Superfast Preparation of High-Quality Reduced Graphene Oxide. *Angew. Chem. Int. Ed.* **2017**, 129, 15883–15888.
- (61) Hu, C.; Sedghi, S.; Silvestre-Albero, A.; Andersson, G. G.; Sharma, A.; Pendleton, P.; Rodriguez-Reinoso, F.; Kaneko, K.; Biggs, M. J. Raman spectroscopy study of the transformation of the carbonaceous skeleton of a polymer-based nanoporous carbon along the thermal annealing pathway. *Carbon* **2015**, 85, 147-158.
- (62) Ferrari, A. C.; Robertson, J. Interpretation of Raman spectra of disordered and amorphous carbon. *Phys. Rev. B* **2000**, 61, 14095-14107.
- (63) Bommier, C.; Luo, W.; Gao, W.-Y.; Greaney, A.; Ma, S.; Ji, X. Predicting capacity of hard carbon anodes in sodium-ion batteries using porosity measurements. *Carbon* **2014**, 76, 165-174.
- (64) Li, Z.; Jian, Z.; Wang, X.; Rodríguez-Pérez, I. A.; Bommier, C.; Ji, X. Hard carbon anodes of sodium-ion batteries: undervalued rate capability. *Chem. Commun.* **2017**, 53, 2610-2613.

(65) Iermakova, D.; Dugas, R.; Palacín, M.; Ponrouch, A. On the comparative stability of Li and Na metal anode interfaces in conventional alkyl carbonate electrolytes. *J. Electrochem. Soc.* **2015**, *162*, A7060-A7066.

Chapter 7 Hard Carbon Anode of Sodium-Ion Batteries: Undervalued Rate Capability

7.1 Abstract

Hard carbon is one of the most promising anode candidates for Na-ion batteries (NIBs). However, the poor rate capability of hard carbon has been considered as one of the major disadvantages which is often attributed to its tortuous nanometric structure. The electrochemical test of NIBs has been followed from LIBs, where the alkali metal, i.e., Li or Na metal, is employed as the counter/reference electrode concurrently. This setup could mask the high-rate capability of hard carbon since more than half of the sodiation capacity in hard carbon takes place at a low-potential plateau region (~ 0.05 V vs. Na^+/Na) vicinal to the sodium plating potential and the unstable potential of sodium metal. Through three-electrode cell setup, we discover that it is the overpotential of the sodium counter electrode that drives the half-cells to the lower cutoff potential prematurely during hard carbon sodiation, particularly at high current rates, which prevents the hard carbon anode from being fully sodiated. Hard carbon demonstrates a much better rate-capability in this three-electrode setup.

7.2 Introduction

Na-ion batteries (NIBs) may provide a sustainable solution for large-scale energy storage, which will facilitate the proliferation of renewable energy installation. Sodium is ubiquitous nearly everywhere, and is much more abundant than

lithium. Furthermore, NIBs share the similar rocking-chair operating mechanism as the well-established lithium-ion batteries (LIBs). After being intensely investigated during the last few years, NIBs become a real rival to LIBs potentially not only for the storage market but the power battery market for electrified transportation. For batteries, the rate capability of their electrodes determines the maximum power of their energy output and how fast the devices can be fully charged. The latter fast-charging characteristics can even be more important than any other metrics sometimes.

There has been a plethora of candidates of NIB cathode.¹⁻⁶ As for the anode side, graphite, the anode for LIBs, does not show a meaningful capacity in NIBs, i.e., 35 mAh/g. Therefore, different types of anode materials, including metal oxides, sodium metal, alloying type materials, phosphorus, and carbonaceous materials have been investigated.⁷⁻¹⁷ Considering the near-future commercialization of NIBs, the current leading anode candidate is hard carbon, also known as non-graphitizable carbon, whose performance in NIBs was first reported by Stevens and Dahn in 2000.¹⁸ Hard carbon's structure can be described by a combination of Franklin's House-of-Cards model and a Fullerene-Fragment model, where highly curved, short, and defective graphenic nanosheets are randomly oriented and are somewhat stacked with large van der Waals distances.^{19, 20} Hard carbon typically can exhibit good capacity values above 250 mAh/g and stable cycling performance. It is also facile to obtain hard carbon simply by pyrolysis of

biomasses, where the high O/C ratio in the carbon precursors causes the formation of hard carbon's unique disordered structure.¹⁹

To date, tremendous effort has been devoted to improving hard carbon's sodium storage capacity, where the impacts from the uniqueness of carbon precursors, morphologies, and heteroatom doping have been studied.²¹⁻²⁷ Recently, significant progress has been made on the capacity of hard carbon. Mitlin et al. reported a reversible capacity of 355 mAh/g with hard carbon derived from banana peels.²⁸ Li et al. reported 359 mAh/g of hard carbon by doping PO_x clusters in the local structure of sucrose-derived hard carbon.²⁹ New mechanistic insights on sodium storage in hard carbon have been proposed based on experimental results.^{22, 29-31} Computational studies on graphene, graphite, and disordered carbon also provided insights on the understanding of sodium storage in hard carbon.³²⁻³⁴ However, it has been nearly a consensus that hard carbon is poor in terms of its rate capability, which is often attributed to its tortuous nanometric structure. Recently, Li et al. reported fairly good high-rate performance of NIB full-cells with hard carbon as the anode, where such high-rate performance was rarely reported in Carbon/Na half-cells.²³

In studies of NIB electrodes, a routine has been followed from LIBs, where the alkali metal, i.e., Li or Na metal, is employed as the counter/reference electrode concurrently, which is often referred to as half-cells. Indeed, half-cells setup

functions well to reveal electrochemical properties of electrodes for LIBs. However, this might be where the issue is for the studies of hard carbon as an anode in NIBs, particularly for revealing its rate capability. The challenge is that more than half of the sodiation capacity in hard carbon takes place at a low-potential plateau region (~ 0.05 V vs. Na^+/Na) vicinal to the sodium plating potential. Any extent of the overpotential on the sodium metal electrode, particularly at high rates, would cause the half-cells to reach the lower cutoff potential prematurely. Therefore, it becomes a necessity to separate the Na metal's roles of being reference and counter electrodes for studying the rate capability of hard carbon anode.

7.3 Experimental Section

Material Synthesis: FP-HC was synthesized by pyrolysis of filter paper at 1400 °C under Ar gas flow for 5 h.

Material Characterization: XRD pattern of FP-HC was collected on a Rigaku Ultima IV Diffractometer with $\text{Cu K}\alpha$ ($\lambda = 1.5406$ Å) radiation. Raman spectra were obtained from WITec confocal Raman spectrometer with a 514 nm laser source and the peaks were deconvoluted by Origin 8.5. Transmission electron microscopy (TEM) was performed on FEI Titan 80-200 TEM.

Electrochemical Measurements: Coin cells (CR2032) and homemade T-Cell (three-electrode cell) were used for the electrochemical measurements. The working electrode consisted of hard carbon, polyvinylidene fluoride (PVdF) and carbon black additive with a mass ratio of 80:10:10. The electrodes were prepared by grounding active material, carbon black and PVdF with N-Methyl-2-pyrrolidone (NMP) as the solvent, and the obtained slurry is coated onto Cu foil by doctor blade and dried at 100 °C for 12 h under vacuum. The active mass loading for all electrodes are between 1.5 to 2 mg/cm². The electrolyte for all cells is 1.0 mol/L NaPF₆ solution in ethylene carbonate (EC)/diethyl carbonate (DEC) (1:1 in volume). Galvanostatic sodiation/desodiation tests are performed in the potential range of 0.01-2 V vs the reference electrode on Arbin BT2000 system at room temperature. Three-electrode cell sodiation/desodiation profiles are collected on a VMP-3 multichannel workstation at room temperature. The rate performance for both two-electrode half-cells and three-electrode cell were sodiated/desodiated at the same current rates of 1 C (250 mA/g), 2 C, 5 C and 10 C, respectively.

7.4 Results and Discussion

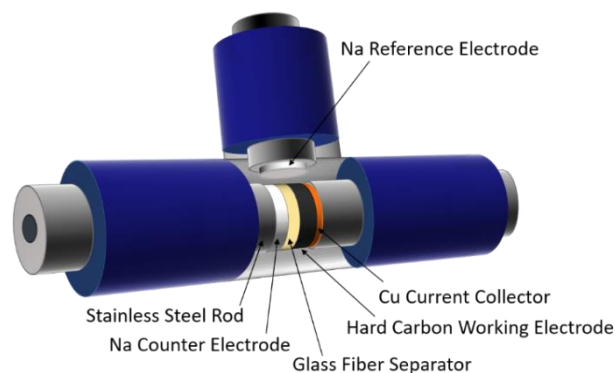


Figure 7.1 Schematic of the three-electrode cell setup.

In this study, we employ a three-electrode cell setup, where two separate Na metal foils are employed as the reference electrode and counter electrode, respectively (see the cell setup in Figure 7.1). This is to remove the possible polarization on the reference electrode, which is also used as the counter electrode in Carbon/Na two-electrode half-cells. Interestingly, the same hard carbon anode exhibits much better rate capability in the three-electrode cell than the two-electrode half-cells. At a current rate of 1C (250 mA/g), hard carbon working electrode in the three-electrode cell exhibits a high capacity of 186 mAh/g, whereas at the same current rate, the same electrode material only provides a capacity of 118 mAh/g in a half-cell.

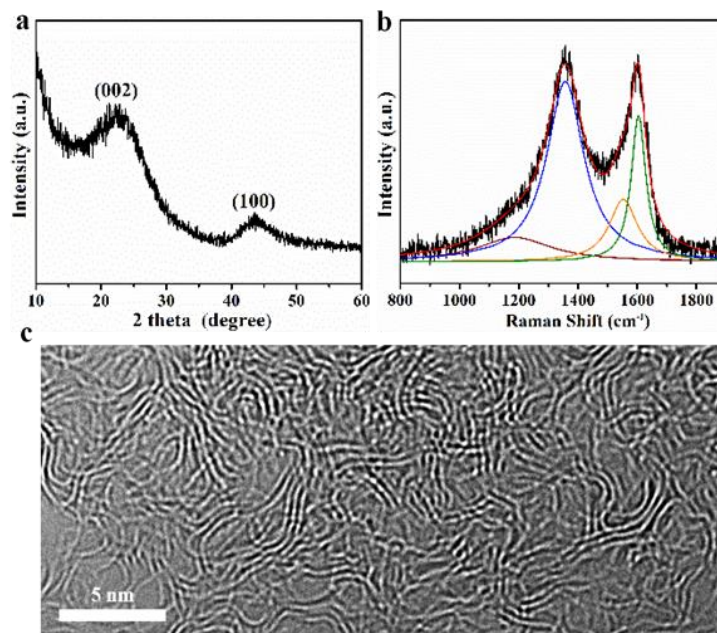


Figure 7.2 (a,b) XRD pattern and Raman spectrum of FP-HC. Raman spectrum was deconvoluted into four Lorentzian peaks: TPA (wine), D (blue), A (orange) and G (green). (c) TEM image of FP-HC.

We prepared a typical hard carbon to study the rate capability, which is derived from the pyrolysis of cellulose filter paper (FP-HC henceforth) at 1400 °C. This hard carbon contains a typical non-graphitic structure. As shown in Figure 7.2a, the x-ray diffraction (XRD) pattern of FP-HC displays a very broad (002) peak around 23.2°, revealing the non-graphitic nature of the obtained FP-HC. Raman spectrum of FP-HC, as shown in Figure 7.2b, displays two broad peaks, which can be deconvoluted into four Lorentzian peaks,³⁵ where D band (~1359 cm⁻¹) is assigned to A_{1g} vibration of C₆ rings induced by defects, and G band (~1604 cm⁻¹) corresponds to the E_{2g} vibration of sp² carbon atoms. The I_D/I_G ratio of 1.26 can

be used to calculate the coherence length of the graphenic domains along lateral *ab* planes according to the following equation:³⁶

$$L_a(\text{nm}) = (2.4 \cdot 10^{-10}) \lambda_{nm}^4 \left(\frac{I_G}{I_D} \right) \quad (1)$$

where the laser wavelength is 514 nm. The calculated domain size of 13.2 nm reveals the extent of defective structure or the existence of curvatures. We also investigated the local structure of this hard carbon by transmission electron microscopy (TEM). As Figure 7.2c shows, FP-HC is composed of small nanodomains with curved layers of graphenic sheets. All structural characterization results confirm that this is a very typical hard carbon structure.

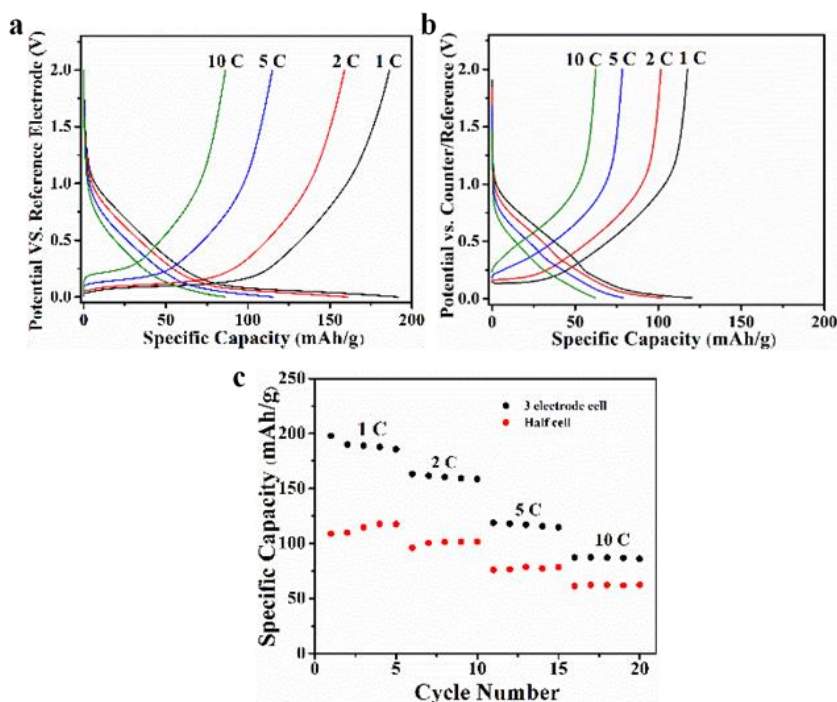


Figure 7.3 (a-c) Sodiation-desodiation potential profiles of the fifth cycle of FP-HC at different current rates in (a) three-electrode cell, (b) half-cell, (c) Rate cycling performance of FP-HC in three-electrode cell and half-cell.

Figure 7.3a shows the sodiation/desodiation profiles of FP-HC in the three-electrode cell at different current rates, where FP-HC shows a reversible capacity of 186, 159, 115 and 86 mAh/g at 1, 2, 5 and 10 C, respectively. In sharp contrast, in the half-cell setup, FP-HC electrode shows much lower capacity of 118, 102, 78 and 62 mAh/g at the current rates with the same sequence (Figure 7.3b). It is worth noting that the cutoff potentials of the working electrode (0.01 to 2 V) in the three-electrode cell are defined by the potential difference between the FP-HC working electrode and the Na metal reference electrode, whereas the cutoff potentials in half-cells are about the difference between the FP-HC electrode and Na metal counter/reference electrode. The fact that the FP-HC electrode in the three-electrode cell exhibits much higher capacity values, especially at high rates, than the half-cells points out the disadvantages of having Na metal as both the counter and reference electrode. In the three-electrode cell, the current going through the reference electrode is kept minimal; however, in a half-cell, the Na reference/counter electrode will at least suffer the ohmic resistance and the consequent overpotential at high current rates. Figure 7.3c shows the rate cycling performance of FP-HC in the three-electrode cell and half-cell, where the capacity is higher in the three-electrode cell than in the half-cell at all current rates.

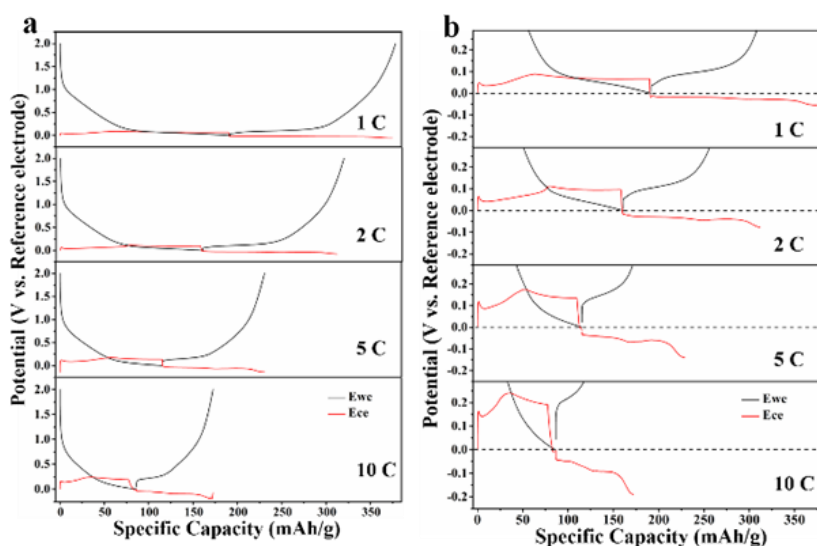


Figure 7.4 Sodiation-desodiation potential profiles of FP-HC of the fifth cycle at different current rates in three-electrode cell. The Ewe and Ece vs. specific capacity are plotted. (a) The full sodiation-desodiation profiles (b) The zoomed-in sodiation-desodiation profiles.

Figure 7.4 displays the potential profiles of both the FP-HC working electrode (E_{we} , black) and the counter electrode of Na metal (E_{ce} , red), both of which are vs. Na-metal reference electrode. It is evident that a large portion of the hard carbon's sodiation capacity is collected at the potentials of the FP-HC working electrode, which are below that of the counter electrode, where this portion of capacity would not be counted in half-cells. Figure 7.4b shows detailed extent of polarization of the Na counter electrode during its stripping, which turns larger upon higher current rates. Its stripping potential increases from below 0.1 V at 1C to above 0.2 V at 10 C. By comparing the potential profiles of the FP-HC electrode at different current rates, its low-potential plateau would be completely “blocked” due to the overpotential of the Na counter electrode beyond 2C in half

cells. The percentage of the capacity from the hard carbon electrode collected below the potential of the Na counter electrode increases from 42% to 57% from at 1C to 10 C. Upon higher current rates, hard carbon's near-intrinsic capacity does decrease; the “blocking effect” from the Na counter electrode would also cause increasing percentage of capacity loss. At this point, we can conclude that the underestimated capacity of hard carbon in half-cells originates from a combination of the low-potential plateau behavior of hard carbon as well as the polarized Na counter electrode at high rates.

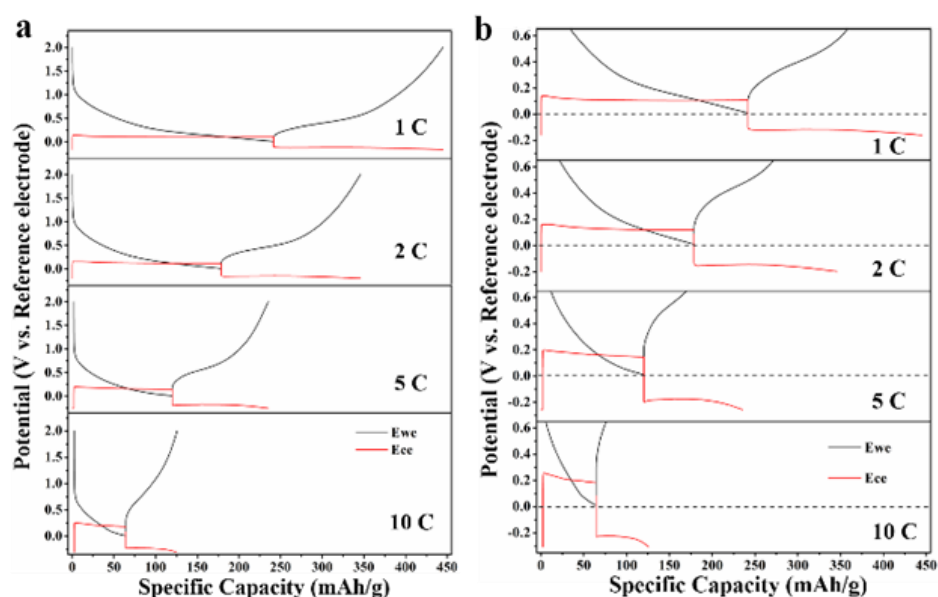


Figure 7.5 Fifth cycle of potassiation-depotassiation profiles of FP-HC at different current rates in three-electrode cell for KIB. The Ewe and Ece vs. specific capacity are plotted. (a) The full potassiation-depotassiation profiles (b) The magnified potassiation-depotassiation profiles.

With the same three-electrode setup, we also tested the K-storage properties of FP-HC for K-ion batteries (KIBs). As shown in Figure 7.5, the FP-HC electrodes

shows a reversible capacity of 203, 167, 115 and 61 mAh/g at 1 C, 2 C, 5 C and 10 C, respectively. By comparing the capacity values of FP-HC in NIBs and KIBs obtained in three-electrode cells, the capacity values are still larger for FP-HC in KIBs at 1C (203 vs. 186 mAh/g) and 2C (167 vs. 159 mAh/g). The two systems have the same capacity at 5 C (115 mAh/g); however, at 10 C, hard carbon in NIBs exhibits a higher capacity than KIBs (86 vs. 61 mAh/g). This is generally in line with the half-cell results of hard carbon spheres (HCS) in KIBs and NIBs, which Jian et al. reported previously.³⁷ It is evident that there is less K-ion storage capacity contribution below the potential of the counter electrode of potassium metal, in contrast to the scenario of Na-ion storage. What intriguing is that the polarization of the potassium metal counter electrode does not increase much upon high current rates, being around 0.2 V from 1C to 10C.

7.5 Conclusions

In summary, through three-electrode cell setup by employing Na metal foils as counter and reference electrode separately, we revealed that hard carbon has intrinsically high rate capability, which had been underestimated by prior studies using conventional half-cell setup. In a three-electrode cell, cellulose-derived hard carbon shows a reversible capacity of 186, 159, 115 and 86 mAh/g at 1, 2, 5 and 10 C, respectively, in sharp contrast to 118, 102, 78 and 62 mAh/g at the rates of the same sequence. The impressive high-rate performance of hard carbon in three-electrode cells calls for caution in terms of interpreting the rate-behavior

results obtained in half-cell studies of hard carbon anodes in NIBs. By using three-electrode cell, we investigated the rate capacity of K-ion storage in the same hard carbon as well. Generally, at high rates, hard carbon exhibits higher capacity values in KIBs than in NIBs; however, caution should be also taken to interpret such advantage. This study provides insights about the intrinsic high rate capability of hard carbon, which would benefit the further development of hard carbon in NIB full cells.

7.6 References

- (1) Mu, L.; Xu, S.; Li, Y.; Hu, Y. S.; Li, H.; Chen, L.; Huang, X. Prototype Sodium-Ion Batteries Using an Air-Stable and Co/Ni-Free O₃-Layered Metal Oxide Cathode. *Adv. Mater.* **2015**, *27*, 6928-6933.
- (2) Jian, Z.; Zhao, L.; Pan, H.; Hu, Y.-S.; Li, H.; Chen, W.; Chen, L. Carbon coated Na₃V₂(PO₄)₃ as novel electrode material for sodium ion batteries. *Electrochem. Commun.* **2012**, *14*, 86-89.
- (3) Xu, Y.; Wei, Q.; Xu, C.; Li, Q.; An, Q.; Zhang, P.; Sheng, J.; Zhou, L.; Mai, L. Layer-by-Layer Na₃V₂(PO₄)₃ Embedded in Reduced Graphene Oxide as Superior Rate and Ultralong-Life Sodium-Ion Battery Cathode. *Adv. Energy Mater.* **2016**, *6*, 1600389.
- (4) Hwang, J. Y.; Myung, S. T.; Yoon, C. S.; Kim, S. S.; Aurbach, D.; Sun, Y. K. Novel Cathode Materials for Na-Ion Batteries Composed of Spoke-Like Nanorods of Na[Ni_{0.61}Co_{0.12}Mn_{0.27}]O₂ Assembled in Spherical Secondary Particles. *Adv. Funct. Mater.* **2016**, *26*, 8083-8093.
- (5) Mao, J.; Luo, C.; Gao, T.; Fan, X.; Wang, C. Scalable synthesis of Na₃V₂(PO₄)₃/C porous hollow spheres as a cathode for Na-ion batteries. *J. Mater. Chem. A* **2015**, *3*, 10378-10385.
- (6) Ha, K. H.; Woo, S. H.; Mok, D.; Choi, N. S.; Park, Y.; Oh, S. M.; Kim, Y.; Kim, J.; Lee, J.; Nazar, L. F. Na_{4-α}M_{2+α/2}(P₂O₇)₂ (2/3 ≤ α ≤ 7/8, M= Fe, Fe_{0.5}Mn_{0.5}, Mn): A Promising Sodium Ion Cathode for Na-ion Batteries. *Adv. Energy Mater.* **2013**, *3*, 770-776.
- (7) Seh, Z. W.; Sun, J.; Sun, Y.; Cui, Y. A highly reversible room-temperature sodium metal anode. *ACS Cent. Sci.* **2015**, *1*, 449-455.

- (8) Lu, Y.; Zhao, Q.; Zhang, N.; Lei, K.; Li, F.; Chen, J. Facile Spraying Synthesis and High-Performance Sodium Storage of Mesoporous MoS₂/C Microspheres. *Adv. Funct. Mater.* **2015**, *26*, 911-918.
- (9) Zhu, X.; Li, Q.; Fang, Y.; Liu, X.; Xiao, L.; Ai, X.; Yang, H.; Cao, Y. Graphene-Modified TiO₂ Microspheres Synthesized by a Facile Spray-Drying Route for Enhanced Sodium-Ion Storage. *Part. Syst. Character.* **2016**, *33*, 545-552.
- (10) Wang, L.; Wang, C.; Zhang, N.; Li, F.; Cheng, F.; Chen, J. High Anode Performance of in-situ Formed Cu₂Sb Nanoparticles Integrated on Cu Foil via Replacement Reaction for Sodium-ion Batteries. *ACS Energy Lett.* **2016**, *2*, 256-262
- (11) Li, M.; Carter, R.; Cohn, A. P.; Pint, C. L. Interconnected foams of helical carbon nanofibers grown with ultrahigh yield for high capacity sodium ion battery anodes. *Carbon* **2016**, *107*, 109-115.
- (12) Cohn, A. P.; Share, K.; Carter, R.; Oakes, L.; Pint, C. L. Ultrafast Solvent-Assisted Sodium Ion Intercalation into Highly Crystalline Few-Layered Graphene. *Nano Lett.* **2015**, *16*, 543-548.
- (13) Zhang, S.-W.; Lv, W.; Luo, C.; You, C.-H.; Zhang, J.; Pan, Z.-Z.; Kang, F.-Y.; Yang, Q.-H. Commercial carbon molecular sieves as a high performance anode for sodium-ion batteries. *Energy Storage Mater.* **2016**, *3*, 18-23.
- (14) Kim, Y.; Kim, Y.; Park, Y.; Jo, Y. N.; Kim, Y.-J.; Choi, N.-S.; Lee, K. T. SnSe alloy as a promising anode material for Na-ion batteries. *Chem. Commun.* **2015**, *51*, 50-53.
- (15) Xu, J.; Wang, M.; Wickramaratne, N. P.; Jaroniec, M.; Dou, S.; Dai, L. High-Performance Sodium Ion Batteries Based on a 3D Anode from Nitrogen-Doped Graphene Foams. *Adv. Mater.* **2015**, *27*, 2042-2048.
- (16) Sun, J.; Lee, H.-W.; Pasta, M.; Yuan, H.; Zheng, G.; Sun, Y.; Li, Y.; Cui, Y. A phosphorene-graphene hybrid material as a high-capacity anode for sodium-ion batteries. *Nat. Nanotechnol.* **2015**, *10*, 980-985.
- (17) Farbod, B.; Cui, K.; Kalisvaart, W. P.; Kupsta, M.; Zehri, B.; Kohandehghan, A.; Lotfabad, E. M.; Li, Z.; Luber, E. J.; Mitlin, D. Anodes for sodium ion batteries based on tin-germanium-antimony alloys. *ACS Nano* **2014**, *8*, 4415-4429.
- (18) Stevens, D.; Dahn, J. High Capacity Anode Materials for Rechargeable Sodium-Ion Batteries. *J. Electrochem. Soc.* **2000**, *147*, 1271-1273.
- (19) Franklin, R. E. Crystallite growth in graphitizing and nongraphitizing carbons. *Proc. R. Soc. London, Ser. A* **1951**, *209*, 196-218.
- (20) Harris, P. J. Fullerene-like models for microporous carbon. *J Mater Sci* **2013**, *48*, 565-577.
- (21) Shen, F.; Luo, W.; Dai, J.; Yao, Y.; Zhu, M.; Hitz, E.; Tang, Y.; Chen, Y.; Sprenkle, V. L.; Li, X., et al. Ultra-Thick, Low-Tortuosity, and Mesoporous Wood

Carbon Anode for High-Performance Sodium-Ion Batteries. *Adv. Energy Mater.* **2016**, *6*, 1600377.

(22) Ding, J.; Wang, H.; Li, Z.; Kohandehghan, A.; Cui, K.; Xu, Z.; Zahiri, B.; Tan, X.; Lotfabad, E. M.; Olsen, B. C. Carbon nanosheet frameworks derived from peat moss as high performance sodium ion battery anodes. *ACS Nano* **2013**, *7*, 11004-11015.

(23) Li, Y.; Hu, Y. S.; Titirici, M. M.; Chen, L.; Huang, X. Hard Carbon Microtubes Made from Renewable Cotton as High-Performance Anode Material for Sodium-Ion Batteries. *Adv. Energy Mater.* **2016**, *6*, 1600659.

(24) Xu, D.; Chen, C.; Xie, J.; Zhang, B.; Miao, L.; Cai, J.; Huang, Y.; Zhang, L. A Hierarchical N/S-Codoped Carbon Anode Fabricated Facilely from Cellulose/Polyaniline Microspheres for High-Performance Sodium-Ion Batteries. *Adv. Energy Mater.* **2016**, *6*, 1501929.

(25) Xiao, L.; Cao, Y.; Henderson, W. A.; Sushko, M. L.; Shao, Y.; Xiao, J.; Wang, W.; Engelhard, M. H.; Nie, Z.; Liu, J. Hard carbon nanoparticles as high-capacity, high-stability anodic materials for Na-ion batteries. *Nano Energy* **2016**, *19*, 279-288.

(26) Zhou, D.; Peer, M.; Yang, Z.; Pol, V. G.; Key, F. D.; Jorne, J.; Foley, H. C.; Johnson, C. S. Long cycle life microporous spherical carbon anodes for sodium-ion batteries derived from furfuryl alcohol. *J. Mater. Chem. A* **2016**, *4*, 6271-6275.

(27) Qie, L.; Chen, W.; Xiong, X.; Hu, C.; Zou, F.; Hu, P.; Huang, Y. Sulfur-Doped Carbon with Enlarged Interlayer Distance as a High-Performance Anode Material for Sodium-Ion Batteries. *Adv. Sci.* **2015**, *2*, 1500195.

(28) Lotfabad, E. M.; Ding, J.; Cui, K.; Kohandehghan, A.; Kalisvaart, W. P.; Hazelton, M.; Mitlin, D. High-density sodium and lithium ion battery anodes from banana peels. *ACS Nano* **2014**, *8*, 7115-7129.

(29) Li, Z.; Ma, L.; Surta, T. W.; Bommier, C.; Jian, Z.; Xing, Z.; Stickle, W. F.; Dolgos, M.; Amine, K.; Lu, J. High Capacity of Hard Carbon Anode in Na-Ion Batteries Unlocked by POx Doping. *ACS Energy Lett.* **2016**, *1*, 395-401.

(30) Bommier, C.; Surta, T. W.; Dolgos, M.; Ji, X. New mechanistic insights on Na-ion storage in nongraphitizable carbon. *Nano Lett.* **2015**, *15*, 5888-5892.

(31) Stratford, J. M.; Allan, P. K.; Pecher, O.; Chater, P. A.; Grey, C. P. Mechanistic insights into sodium storage in hard carbon anodes using local structure probes. *Chem. Commun.* **2016**, *52*, 12430-12433.

(32) Datta, D.; Li, J.; Shenoy, V. B. Defective graphene as a high-capacity anode material for Na- and Ca-ion batteries. *ACS Appl. Mater. Interfaces* **2014**, *6*, 1788-1795.

(33) Liu, Y.; Merinov, B. V.; Goddard, W. A. Origin of low sodium capacity in graphite and generally weak substrate binding of Na and Mg among alkali and alkaline earth metals. *Proc Natl Acad Sci* **2016**, *113*, 3735-3739.

(34) Tsai, P.-C.; Chung, S.-C.; Lin, S.-k.; Yamada, A. Ab initio study of sodium intercalation into disordered carbon. *J. Mater. Chem. A* **2015**, *3*, 9763-9768.

- (35) Hu, C.; Sedghi, S.; Silvestre-Albero, A.; Andersson, G. G.; Sharma, A.; Pendleton, P.; Rodriguez-Reinoso, F.; Kaneko, K.; Biggs, M. J. Raman spectroscopy study of the transformation of the carbonaceous skeleton of a polymer-based nanoporous carbon along the thermal annealing pathway. *Carbon* **2015**, *85*, 147-158.
- (36) Cancado, L.; Takai, K.; Enoki, T.; Endo, M.; Kim, Y.; Mizusaki, H.; Jorio, A.; Coelho, L.; Magalhaes-Paniago, R.; Pimenta, M. General equation for the determination of the crystallite size L_a of nanographite by Raman spectroscopy. *Appl. Phys. Lett.* **2006**, *88*, 163106-163106.
- (37) Jian, Z.; Xing, Z.; Bommier, C.; Li, Z.; Ji, X. Hard Carbon Microspheres: Potassium-Ion Anode Versus Sodium-Ion Anode. *Adv. Energy Mater.* **2016**, *6*, 1501874.

Chapter 8 Low-temperature Pyrolyzed Soft Carbon Anodes for K-ion Storage

8.1 Abstract

K-ion batteries (KIBs) are emerging as a new option for large-scale energy storage. Graphite was reported to be able to reversibly store K-ions by forming KC₈. However, graphite does not show a promising cycling performance due to the large volume change upon (de)potassiation. Non-graphitic carbons including soft carbons and hard carbons have been studied as anode materials for potassium-ion storage; however, so far, the reported non-graphitic carbons have rarely been demonstrated with a capacity above 300 mA/g. In addition, the mechanism of potassium-ion storage in non-graphitic carbons is not well understood. Herein, soft carbons (SCs) were obtained with different pyrolysis temperatures with well controlled surface area and their K-ion storage properties were investigated. The SC obtained at low pyrolysis temperature (700°C) demonstrated the highest capacity of 350 mAh/g, excellent rate capability and good cycling performance. Combining with computational studies, the mechanism of K-ion storage in SCs was investigated.

8.2 Introduction

Grid-scale stationary energy storage is attracting more attention along with the exponential increase needs of Li-ion batteries (LIBs) in consumer electronics and electric vehicles. Unfortunately, lithium is not an Earth-abundant element and it is unevenly distributed in several countries which raises the concerns of using LIBs for

large-scale energy storage. For consumer electronics and electric vehicles high energy density is one of the most important parameters, whereas in grid-scale stationary energy storage, energy density is not the first priority. Metal-ion batteries with cheap and Earth-abundant elements such as Na-ion batteries (NIBs) and K-ion batteries (KIBs) have been considered as good candidates for grid-scale energy storage.¹⁻³ Compare with NIB, KIB is still in its infancy stage. On the cathode side, Prussian blue analogues, layered metal oxides and potassium vanadium phosphates have been demonstrated with decent K-ion storage performance.⁴⁻¹¹ On the anode side, graphite, which does not show meaningful capacity, i.e. 35 mAh/g in NIBs, has been reported with a reversible capacity above 220 mAh/g.¹²⁻¹⁴ However, the cycling performance and rate capability of graphite is unsatisfied due to the large volume expansion during the K-ion insertion/deinsertion. So far, carbonaceous materials, especially non-graphitic carbons, are the most studied anode materials for KIBs and remain as the most promising anode materials for KIBs.¹⁵⁻¹⁷ Recently, non-graphitic carbons including hard carbons (HCs) and soft carbons (SCs), nitrogen-doped non-graphitic and graphitic carbons have been reported to show a decent K-ion storage capacity, whereas carbon materials with capacity higher than 300 mAh/g have rarely been reported, especially for non-graphitic carbons.¹⁷⁻²² Even though the size of K^+ is larger than Na^+ , the lowered redox potential of K^+/K renders non-graphitic carbons the possibility of showing a comparable or even higher capacity in KIBs than in NIBs.

The understanding of K-ion storage in non-graphitic carbons is still limited and not all the principles of Na-ion storage in non-graphitic carbons can be transferred to K-ion storage. In our group, we had studied HCs and SCs as anode for K-ion storage, where HC shows a higher reversible capacity and better cycling performance, and SCs with a lower reversible capacity and worse cycling stability show a better rate capability.^{13, 15, 17} The worse cycling stability of SC was attributed to the structure change during potassiation/depotassiation, where the local structure of HC is more rigid. It is worth to note that all the non-graphitic carbons in our previous studies were synthesized at temperature above 900°C. According to our previous studies, high defect concentration could lead to a high reversible slope capacity for Na-ion storage in non-graphitic carbons and low pyrolysis temperature leads to high defect concentration. We had demonstrated that SC obtained at low pyrolysis temperature, e.g., 700°C, shows higher Na-ion storage capacity, however, its rate capability is worse than those obtained at higher pyrolysis temperatures.²³⁻²⁵ As K⁺ has a lower charge density and redox potential than Na⁺ which may lead to different ion storage properties, it is worth to study the K-ion storage in SCs, especially in the low-temperature pyrolyzed SCs. While the higher defect concentration of low-temperature pyrolyzed SCs could lead to a higher reversible K-ion storage capacity, they may also have better cycling stability than high-temperature pyrolyzed SCs as they would have a much smaller domain size and thus less volume expansion.

Herein, in this present research, we synthesized a series of SCs by the pyrolysis of 3,4,9,10-perylenetetracarboxylic dianhydride (PTCDA) at different temperatures. By using polyacrylic acid (PAA) as the binder, SC obtained at 700°C (SC700) delivers the highest capacity of 350 mAh/g which is the highest capacity of non-graphitic carbons reported so far by accounting the potential between 0-2 V. More importantly, SC700 also demonstrates a better rate capability and cycling stability than SCs obtained at higher temperatures. Through high-resolution transmission electron microscopy (TEM), PDF studies associated with neutron total scattering, Raman spectra and computational studies, the mechanism of the high capacity and the fading of SC700 are investigated. This work would bring new insights about K-ion storage in SCs.

8.3 Experimental Section

Materials Synthesis and Characterization: For the preparation of soft carbons, 1 g PTCDA was pyrolyzed in quartz tube furnace at 700°C, 900°C, and 1100°C, respectively, for 5h under Ar gas flow. For the synthesis of hard carbons, 2 g precursor, the filter paper was first sonicated in water for 6 h and dried at 80°C for 12 h, and then it was preheated in air at 240 °C for 8 h. After the pretreatment, the precursor was annealed at 650°C and 1100°C, respectively, for 7 h under Ar gas flow.

The N₂ sorption isotherms of all the carbon samples were performed on Micromeritics TriStar II 3020 analyzer for the BET surface area analysis. Powder XRD patterns of all the samples were collected via Rigaku Ultima IV Diffractometer with Cu K α (λ =

1.5406 Å) radiation. High resolution transmission electron microscopy (TEM) images were obtained by FEI Titan 80-200 (TEM). WITec confocal Raman spectrometer with a 514 nm laser source was used to gather Raman spectra, and Origin 8.5 was used for the fitting of the spectra. The neutron diffraction data was collected at the Nanoscale Ordered Materials Diffractometer (NOMAD), Spallation Neutron Source, at Oak Ridge National Laboratory, where quartz capillaries were used to load the carbon samples.

Electrochemical Measurements: CR2032 coin cells were assembled to perform the galvanostatic charge-discharge and cycling tests on Maccor battery tester. The CV tests were performed on Bio-logic EC Lab VMP-3. For the preparation of the electrode, 80 wt% active material, 10 wt% PAA, and 10 wt% carbon black were mixed together in a mortar with N-Methyl-2-pyrrolidone (NMP) to make the slurry. The obtained slurry was painted onto copper foil and then dried in the oven at 100 °C for 12 h. For all electrodes, the total mass loading is between 1.0 to 1.5 mg. To prepare the electrolyte, 1.0 mol/L NaPF₆ was dissolved in ethylene carbonate (EC)/diethyl carbonate (DEC) (1:1 in volume).

8.4 Results and Discussion

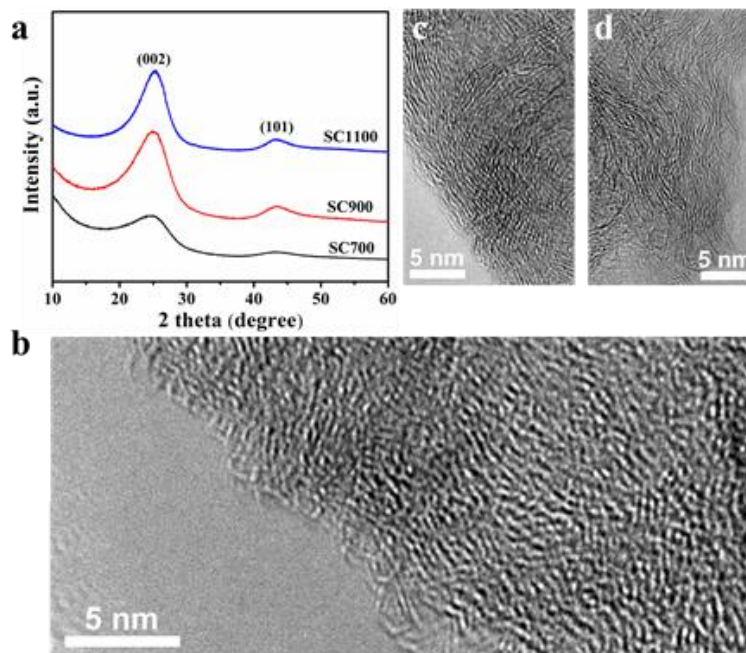


Figure 8.1 (a) XRD patterns of all the obtained SCs. High-resolution TEM image of SC obtained by the pyrolysis of PTCDA at (b) 700°C (c) 900°C and (d) 1100°C.

The SCs were obtained by the pyrolysis of PTCDA at 700, 900 and 1100°C, respectively. All the obtained SCs show small Brunauer-Emmett-Teller (BET) surface area ($< 30 \text{ m}^2/\text{g}$). The broad (002) and (101) peak of all the SCs demonstrate that they are all non-graphitic, where the (002) peak becomes sharper with the increase of pyrolysis temperature (Figure 8.1a). To further study the microstructure of SCs, high-resolution TEM images were collected (Figure 8.1b-d). The SC700 shows a much different microstructure with SC900 and SC100, where the average domain size of SC700 is below 2 nm. It is worth to note that even though the average domain size of SC700 is below 2 nm, most of the nanodomains are generally aligned along a certain direction

but not fully connected. This phenomenon should be derived from the PTCDA precursor which is a crystalline organic molecule that has an ordered stacking of planar aromatic molecules. At low pyrolysis temperature, i.e., 700°C, the energy is not enough to make the carbon atoms on the edge of one molecule to migrate and bond together with carbon atoms on the surrounding molecules which leads to the small domain size and could also result in a high defect concentration of SC700. When the pyrolysis temperature increased to 900 and 1100°C, the domain size of the obtained SCs increased, where the average domain size of SC1100 is above 12 nm.

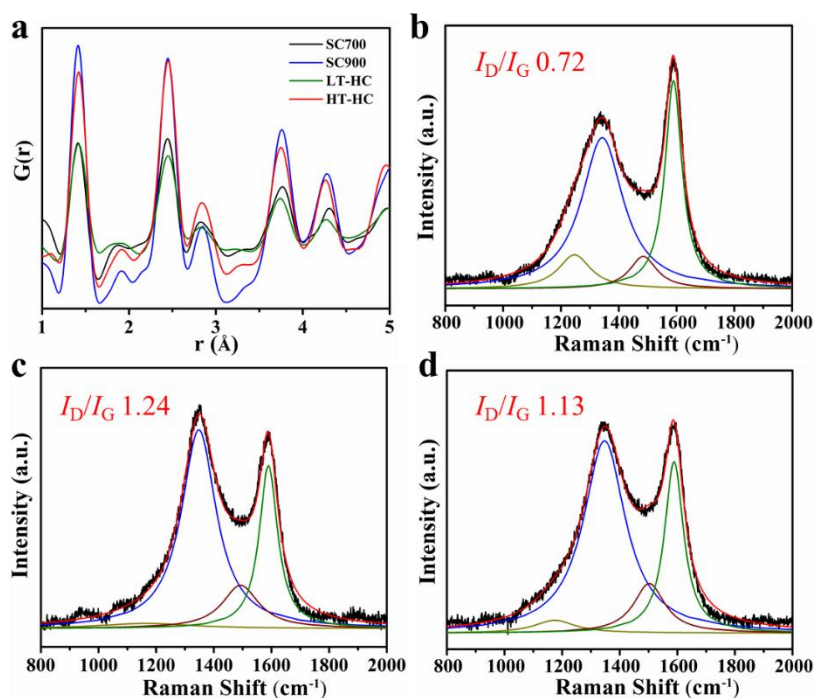


Figure 8.2 (a) PDF studies associated with the neutron total scattering of SC700, SC900 and hard carbons. Raman spectra of SCs, where the spectra were deconvoluted with four Lorentzian peaks: TPA (dark yellow), D (blue), A (wine) and G (green). (b) SC700, (c) SC900, and (d) SC1100.

The defect concentration has been proved to be crucial for the performance of Na-ion storage in non-graphitic carbon in addition to the domain size and interlayer spacing. Therefore, in order to investigate the effects of the defect concentration on K-ion storage in SCs, we performed pair distribution function (PDF) study associated with the neutron total scattering and Raman spectroscopy to characterize the defect concentration. Our prior studies about hard carbons have proved that Neutron total scattering associated with PDF is a reliable technique for the study of defect concentration of non-graphitic carbons.^{24, 25} The PDF results were obtained by performing Fourier transformation of the structure functions $S(Q)$ via equation (3):

$$\frac{A}{4\pi} G(r) = A\rho[g(r) - 1] = \frac{1}{2\pi^2} \sum_0^{Q^{max}} QA[S(Q) - 1] \sin(QR) \Delta Q \quad (3)$$

where in this equation, A is a constant obtained during normalization, ρ is the atomic number density, $g(r)$ stands for the atomic pair distribution function, and Q is the scattering vector. In the PDF results (Figure 8.2a), the peak positions (r) is corresponding to the averaged real space distance between a randomly selected carbon central atom and its surrounding atoms over all atoms. The higher probability of finding atoms at a specific peak position, the higher the peak amplitude will be. Therefore, a high peak amplitude means a low defect concentration of the sample. This enable us to directly compare the defect concentration of different carbon samples by plotting their $G(r)$ vs r together. As shown in Figure 8.2a, the peak amplitude of SC900 is much higher than SC700 which means that the defect concentration of SC900 is much higher than

that of SC700. This is reasonable as the increased pyrolysis temperature will lead to a larger domain size and will also eliminate some in-plane vacancies, and thus less defects.

To further examine the structure of SCs, we also gathered Raman spectra of all the SCs (Figure 8.2 b-d). In Raman spectrum of carbon sample, the presence of D band at ~ 1345 cm^{-1} is ascribed to the A_{1g} breathing mode of carbon aromatic clusters, which is activated by defects, and the presence of G band at ~ 1595 cm^{-1} is correlated to the stretching of the in-plane sp^2 carbon atoms. In Raman spectrum, the I_D/I_G ratio can indicate the order degree and defect concentration of the structure. To accurately obtain the I_D/I_G ratio, the Raman spectra of all SCs were deconvoluted into four Lorentzian peaks (Figure 8.2b-d), where SC700 with the smallest domain size shows the lowest I_D/I_G ratio (0.72). Normally, a lower I_D/I_G ratio represents a lower degree of graphenic order along the *ab* plane and a higher defect concentration. However, this correlation does not hold when the average domain size of carbon is below 2 nm.²⁶ According to the TEM results, the average domain size of SC700 should be below 2 nm and this explains the much lower I_D/I_G ratio of SC700 comparing with SC900 (1.24) and SC1100 (1.13). As shown in Figure 8.2 c and d, SC1100 exhibits a lower I_D/I_G ratio than SC900 which suggests that SC1100 is more ordered and has a lower defect concentration than SC900. Combing the neutron total scattering results and the Raman results, it is evident that SC700 with the lowest pyrolysis temperature has the highest defect concentration.

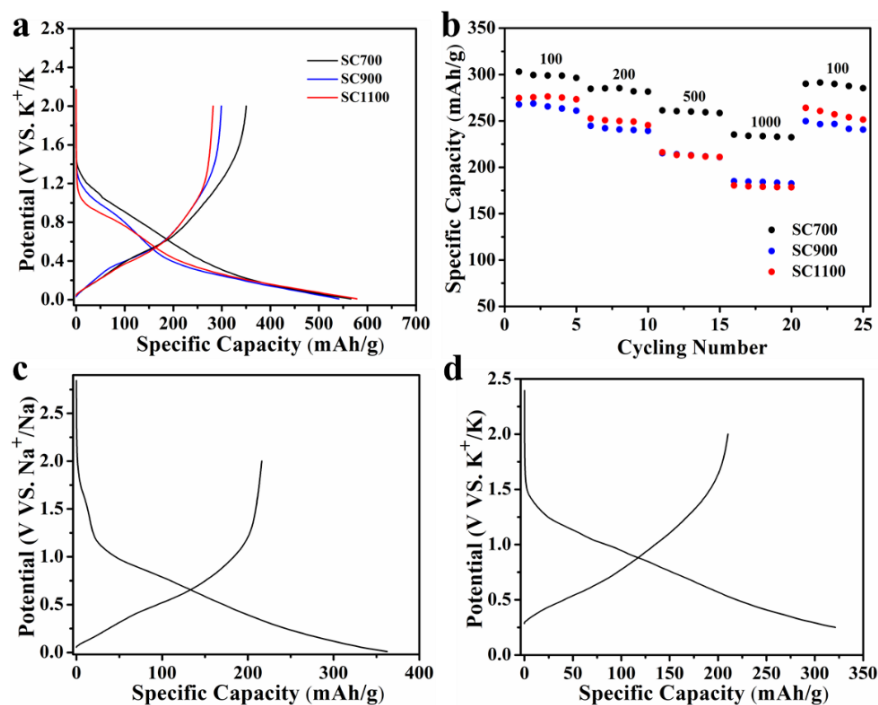


Figure 8.3 Electrochemical performance of the SCs electrodes. (a) Potassiation/depotassiation potential profiles of all SCs at a current rate of 20 mA/g. The potential is vs K^+/K . (b) Rate capability of all SCs in the current range of 100 to 1000 mA/g. (c) Sodiation/desodiation profile of SC700 at a current of 20 mA/g. The potential is vs Na^+/Na . (d) Potassiation/depotassiation profile of SC700 at the cut-off potential of 0.25 V.

The K-ion storage properties of SCs were investigated in half-cells. As shown in Figure 8.3a, the SC700 demonstrates the highest reversible K-ion storage capacity of 350 mAh/g among the three SCs, which is the highest capacity of non-graphitic carbon reported so far by accounting the potential range of 0-2 V. It is worth to note that the capacity from the potential above 2 V does not contribute too much in the full cell. With the increasing pyrolysis temperature of SC, the reversible K-ion storage capacity of SCs decreases to 299 mAh/g of SC900, and 282 mAh/g of SC1100. In addition, the first cycle coulombic efficiency (FCCE) of SC700 is 62% which is higher than that of SC900

(55%) and SC1100 (50%). By looking into the potassiation/depotassiation profiles of SCs, it is evident that the higher capacity of SC700 is from the high-potential region (0.6-2 V). In our prior studies about Na-ion storage in non-graphitic carbon, we conclude that the high potential sloping capacity is contributed from the Na-ion binding with the defect sites. We had demonstrated that among these three SCs, SC700 has the highest defect concentration. Therefore, the higher capacity of SC700 should be due to its higher defect concentration.

Comparing with our prior NIBs study, all the SCs deliver a much higher capacity for K-ion storage than Na-ion storage.²³ However, polyvinylidene fluoride (PVdF) was used as the binder in our prior Na-ion storage study. Therefore, in order to make a fair comparison, we also test the Na-ion storage performance of SC700 by using PAA as the binder. As shown in Figure 8.3 c, the reversible Na-ion storage capacity of SC700 is 216 mAh/g with the CE@1st of 60%. As the potential of K^+/K is about 0.25 V lower than that of Na^+/Na in EC/DEC, we test the K-ion storage of SC700 at the cut-off potential of 0.25 in a C/K half-cell. The SC700 only delivers a capacity of 210 mAh/g with the CE@1st of 65%, where at this cut-off potential, SC700 show a very similar capacity for Na-ion and K-ion storage. Therefore, the much higher K-ion storage capacity of SCs than Na-ion should be due to the lower redox potential of K^+/K which can enable more K-ion insertion into the SCs structure. This can also be corroborated by the long plateau of the SCs under 0.25 V during the potassiation process.

Note that even at a cut-off potential of 0.25 V, SC700 still has a higher CE@1st of 65% than that of 60% of Na-ion storage in SC700. In order to understand this disparity and gain further mechanistic insights about the K-ion storage in soft carbon, we performed density functional theory (DFT) calculations to study the binding energetics of K-ion with various structural sites and compare them with Na-ion binding energetics. Graphene nanosheets were used as the model to study the binding energetics of K-ion and Na-ion as the local atomic structure of SCs resemble that of small graphene sheets. Vienna ab-initio Simulation Package (VASP) was used to perform the calculations with the dispersion corrected exchange correlation functionals. The sodiation energy was calculated with the following equation:

$$E_{bnd}(x) = \frac{1}{n_K} (E_{sub+K}(x) - E_{sub} - n_K E_{K-BCC}) \quad (4)$$

$$E_{bnd}(x) = \int_0^x eV(x') dx' = \int_0^{q/e} V(q') dq' \quad (5)$$

where E_{sub+K} represents the energy of the relaxed carbon substrate-Na system, E_{sub} is the energy of the original carbon substrate, and E_{K-BCC} is the per atom cohesive energy of BCC potassium metal. The quantity n_K is the number of K atoms in a calculation and x is the concentration of K atoms to the substrate atoms. Without considering entropic contributions, the binding energy calculated in this way can be correlated to the discharge voltage in the environment of C/K half-cell with the expression: the integral above, where q is the stored charge.

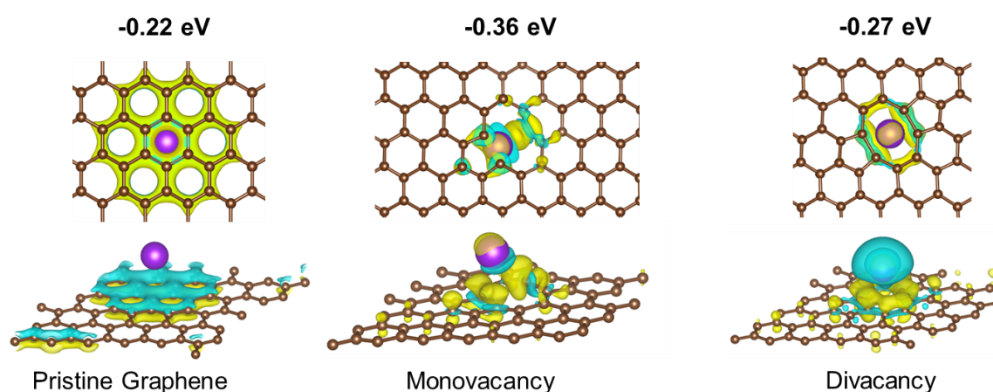


Figure 8.4 Different simulated graphene/K system with the charge distribution and binding energies shown. The green regions represent a negative charge and the yellow regions represent positive charges. (a) pristine graphene, (b) monovacancy graphene, (c) divacancy graphene.

Table 8.1 Na-ion and K-ion binding energy with different structural sites.

Binding Energy (eV)	Pristine	Mono-vacancy	Di-vacancy
Na-ion	+0.44	-1.08	-0.81
K-ion	-0.22	-0.36	-0.27

As shown in Figure 8.4, the binding energy of K-ion with pristine graphene sheet is -0.22 eV, where the binding energies with monovacancy and divacancy are -0.36 and -0.27 eV, respectively. In addition, both the positive and negative charge are evenly distributed in pristine graphene sheet, however, they are more concentrated on the defect sites for both monovacancy and divacancy. Our previous work had shown that the binding energy of Na-ion with pristine graphene sheet is +0.44 eV. This means that the

binding between K-ion and the pristine graphene sheet is favorable, however, the binding between Na-ion and the pristine graphene sheet is not favorable. This may ascribe to the lower redox potential of K^+/K comparing with Na^+/Na . Both Na-ion and K-ion have a negative binding energy and thus favorable binding with monovacancy and divacancy (Table 1). However, comparing the binding between Na-ion and these various defect sites, K-ion has smaller absolute binding energies with these defect sites. These results indicate that the binding between K-ion and these defect sites is not as strong as Na-ion. As we revealed in our previous study that too strong binding between Na-ion and the hard carbon structure could lead to irreversibility. These lower binding energies of K-ion could be the reason that SC700 shows a higher FCCE for K-ion storage than Na-ion storage even at a cut-off potential of 0.25 V. Through the computational studies we demonstrate that K-ion has suitable binding energies with various structural sites which enables its decent K-ion storage capacity even at a cut-off potential of 0.25 V and its higher FCCE.

Table 8.2 Capacity retention of all SCs at different current rates.

Capacity Retention	100 mA/g	200 mA/g	500 mA/g	1000 mA/g
SC700	100%	95%	87%	96%
SC900	100%	90%	77%	92%
SC1100	100%	92%	81%	92%

In NIBs, our group reported that SC700 has the highest capacity for Na-ion storage compares with the SCs obtained at higher pyrolysis temperature.²³ However, SC700 showed worse rate capability than SC900. Therefore, we performed rate capability tests of all the three SCs in the current range of 100 to 1000 mA/g for K-ion storage. As shown in Figure 3b, SC700 shows good rate capability, where its capacity is 296, 282, 258, and 232 mAh/g at a current density of 100, 200, 500 and 1000 mA/g, respectively. In addition, in sharp contrast to Na-ion storage in SCs, SC700 exhibits the highest capacity retention among these three SCs at all different current rate as summarized in Table 2. The good rate capability of SC700 for K-ion storage should be due to the suitable binding energies between K-ion and different defect sites, and the lower charge density of K-ion than Na-ion.

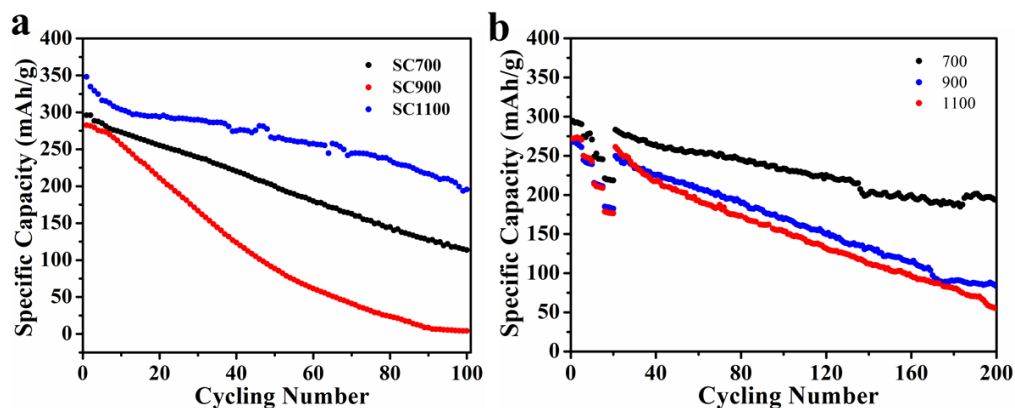


Figure 8.5 (a) Cycling performance of SCs at different current rates of 20 mA/g. (b) Cycling performance of SCs at 100 mA/g after rate capability test at the current rates of 100, 200, 500 and 1000mA/g.

We also evaluated the long cycling stability of all the SCs under current rate of 20 and 100 mA/g. At the current rate of 20 mA/g, SC700 demonstrates a much better cycling

stability than SC900 and SC1100, where the capacity retention after 100 cycles is 56%, 39% and 2% for SC700, SC900 and SC1100, respectively (Figure 8.5a). As shown in Figure 8.5b, after the rate capability test, most of the capacity is recovered for all SCs when the current is returned to 100 mA/g, and the capacity retention for SC700, SC900 and SC1100 after 200 cycles is 65%, 31%, and 20%, respectively. It is obvious that the SC700 exhibits much better cycling stability than SC900 and SC1100 at both low and high current rate. As we discussed in our prior study, the poor cycling performance of SC900 may be caused by the volume changes upon potassiation. As SC1100 has larger domain size and smaller interlayer spacing, the volume changes of SC1100 should be even larger than SC900 upon potassiation. This should be the reason that SC 1100 shows the worst cycling performance among these three SCs. In contrast to SC900 and SC1100, SC700 with the smallest domain size and the highest defect concentration, may cause smaller volume changes upon potassiation and thus lead to the highest capacity and good cycling performance. It is worth to note, even for SC700, its cycling stability is still not satisfying. However, in this current work, we demonstrate that SC700 has the highest capacity with the highest defect concentration, good rate capability and better cycling stability than the SCs obtained at high pyrolysis temperatures.

8.5 Conclusions

In conclusion, by the pyrolysis of PTCDA at different temperatures, we obtained a series of SCs with well controlled surface area. The K-ion storage properties of these SCs was thoroughly investigated and compared with their Na-ion storage properties. The SC700

delivers the highest capacity among these three SCs where its high capacity is attributed to its high defect concentration, indicating that the high-potential sloping region of K-ion storage in SCs is due to K-ion binding with defects. By comparing with Na-ion storage in SC700, we revealed that the much higher capacity of K-ion storage in SC700 is most likely due to the lower redox potential of K^+/K . In addition, our computational studies suggest that K-ion has a more suitable binding energies with various defect sites than Na-ion which explains its higher FCCE than Na-ion storage in SC700 even when the cut-off potential of K-ion storage is at 0.25 V. SC700 also demonstrate better rate capability and cycling stability than the SCs obtained at higher pyrolysis temperature. This study shows the potential of low temperature pyrolyzed carbon anode for K-ion storage and shed lights on the mechanism of K-ion storage in SCs.

8.6 References

- (1) Eftekhari, A.; Jian, Z.; Ji, X. Potassium secondary batteries. *ACS Appl. Mater. Interfaces* **2016**, *9*, 4404-4419.
- (2) Pramudita, J. C.; Sehwat, D.; Goonetilleke, D.; Sharma, N. An Initial Review of the Status of Electrode Materials for Potassium-Ion Batteries. *Adv. Energy Mater.* **2017**, *7*, 160291.
- (3) Yabuuchi, N.; Kubota, K.; Dahbi, M.; Komaba, S. Research development on sodium-ion batteries. *Chem. Rev.* **2014**, *114*, 11636-11682.
- (4) Kim, H.; Kim, J. C.; Bo, S. H.; Shi, T.; Kwon, D. H.; Ceder, G. K-Ion Batteries Based on a P2-Type $K_{0.6}CoO_2$ Cathode. *Adv. Energy Mater.* **2017**, *7*, 1700098.
- (5) Hironaka, Y.; Kubota, K.; Komaba, S. P2-and P3- K_xCoO_2 as an electrochemical potassium intercalation host. *Chem. Commun.* **2017**, *53*, 3693-3696.
- (6) Wu, X.; Jian, Z.; Li, Z.; Ji, X. Prussian white analogues as promising cathode for non-aqueous potassium-ion batteries. *Electrochem. Commun.* **2017**, *77*, 54-57.
- (7) Lin, X.; Huang, J.; Tan, H.; Huang, J.; Zhang, B. $K_3V_2(PO_4)_2F_3$ as a Robust Cathode for Potassium-Ion Batteries. *Energy Storage Mater.* **2019**, *16*, 97-101.

- (8) Bie, X.; Kubota, K.; Hosaka, T.; Chihara, K.; Komaba, S. A novel K-ion battery: hexacyanoferrate (II)/graphite cell. *J. Mater. Chem. A* **2017**, *5*, 4325-4330.
- (9) Liao, J.; Hu, Q.; Yu, Y.; Wang, H.; Tang, Z.; Wen, Z.; Chen, C. A potassium-rich iron hexacyanoferrate/dipotassium terephthalate@carbon nanotube composite used for K-ion full-cells with an optimized electrolyte. *J. Mater. Chem. A* **2017**, *5*, 19017-19024.
- (10) Vaalma, C.; Giffin, G. A.; Buchholz, D.; Passerini, S. Non-aqueous K-ion battery based on layered $K_{0.3}MnO_2$ and hard carbon/carbon black. *J. Electrochem. Soc.* **2016**, *163*, A1295-A1299.
- (11) Deng, T.; Fan, X.; Luo, C.; Chen, J.; Chen, L.; Hou, S.; Eidson, N.; Zhou, X.; Wang, C. Self-templated formation of P2-type $K_{0.6}CoO_2$ microspheres for high reversible potassium-ion batteries. *Nano Lett.* **2018**, *18*, 1522-1529.
- (12) Komaba, S.; Hasegawa, T.; Dahbi, M.; Kubota, K. Potassium intercalation into graphite to realize high-voltage/high-power potassium-ion batteries and potassium-ion capacitors. *Electrochem. Commun.* **2015**, *60*, 172-175.
- (13) Jian, Z.; Luo, W.; Ji, X. Carbon electrodes for K-ion batteries. *J. Am. Chem. Soc.* **2015**, *137*, 11566-11569.
- (14) Luo, W.; Wan, J.; Ozdemir, B.; Bao, W.; Chen, Y.; Dai, J.; Lin, H.; Xu, Y.; Gu, F.; Barone, V. Potassium ion batteries with graphitic materials. *Nano Lett.* **2015**, *15*, 7671-7677.
- (15) Jian, Z.; Xing, Z.; Bommier, C.; Li, Z.; Ji, X. Hard Carbon Microspheres: Potassium-Ion Anode Versus Sodium-Ion Anode. *Adv. Energy Mater.* **2016**, *6*, 1501874.
- (16) Wang, W.; Zhou, J.; Wang, Z.; Zhao, L.; Li, P.; Yang, Y.; Yang, C.; Huang, H.; Guo, S. Short-Range Order in Mesoporous Carbon Boosts Potassium-Ion Battery Performance. *Adv. Energy Mater.* **2018**, *8*, 1701648.
- (17) Jian, Z.; Hwang, S.; Li, Z.; Hernandez, A. S.; Wang, X.; Xing, Z.; Su, D.; Ji, X. Hard-Soft Composite Carbon as a Long-Cycling and High-Rate Anode for Potassium-Ion Batteries. *Adv. Funct. Mater.* **2017**, *27*, 1700324.
- (18) Zhao, X.; Tang, Y.; Ni, C.; Wang, J.; Star, A.; Xu, Y. Free-Standing Nitrogen-Doped Cup-Stacked Carbon Nanotube Mats for Potassium-Ion Battery Anodes. *ACS Appl. Energy Mater.* **2018**, *1*, 1703-1707.
- (19) Chen, M.; Wang, W.; Liang, X.; Gong, S.; Liu, J.; Wang, Q.; Guo, S.; Yang, H. Sulfur/Oxygen Codoped Porous Hard Carbon Microspheres for High-Performance Potassium-Ion Batteries. *Adv. Energy Mater.* **2018**, 1800171.
- (20) Liu, L.; Chen, Y.; Xie, Y.; Tao, P.; Li, Q.; Yan, C. Understanding of the Ultrastable K-Ion Storage of Carbonaceous Anode. *Adv. Funct. Mater.* **2018**, 1801989.
- (21) Zhao, J.; Zou, X.; Zhu, Y.; Xu, Y.; Wang, C. Electrochemical intercalation of potassium into graphite. *Adv. Funct. Mater.* **2016**, *26*, 8103-8110.

- (22) Xu, Y.; Zhang, C.; Zhou, M.; Fu, Q.; Zhao, C.; Wu, M.; Lei, Y. Highly nitrogen doped carbon nanofibers with superior rate capability and cyclability for potassium ion batteries. *Nat. Commun.* **2018**, *9*, 1720.
- (23) Luo, W.; Jian, Z.; Xing, Z.; Wang, W.; Bommier, C.; Lerner, M. M.; Ji, X. Electrochemically expandable soft carbon as anodes for Na-ion batteries. *ACS Cent. Sci.* **2015**, *1*, 516-522.
- (24) Li, Z.; Bommier, C.; Chong, Z. S.; Jian, Z.; Surta, T. W.; Wang, X.; Xing, Z.; Neufeind, J. C.; Stickle, W. F.; Dolgos, M. Mechanism of Na-Ion Storage in Hard Carbon Anodes Revealed by Heteroatom Doping. *Adv. Energy Mater.* **2017**, *7*, 1602894.
- (25) Bommier, C.; Surta, T. W.; Dolgos, M.; Ji, X. New mechanistic insights on Na-ion storage in nongraphitizable carbon. *Nano Lett.* **2015**, *15*, 5888-5892.
- (26) Ferrari, A. C.; Robertson, J. Interpretation of Raman spectra of disordered and amorphous carbon. *Phys. Rev. B* **2000**, *61*, 14095-14107.